



City Research Online

City, University of London Institutional Repository

Citation: Rodriguez Fernandez, Carlos (2019). Supercritical, transcritical and subcritical real-fluid mixing at high-pressure conditions using the PC-SAFT EoS. (Unpublished Doctoral thesis, City, University of London)

This is the accepted version of the paper.

This version of the publication may differ from the final published version.

Permanent repository link: <https://openaccess.city.ac.uk/id/eprint/23069/>

Link to published version:

Copyright: City Research Online aims to make research outputs of City, University of London available to a wider audience. Copyright and Moral Rights remain with the author(s) and/or copyright holders. URLs from City Research Online may be freely distributed and linked to.

Reuse: Copies of full items can be used for personal research or study, educational, or not-for-profit purposes without prior permission or charge. Provided that the authors, title and full bibliographic details are credited, a hyperlink and/or URL is given for the original metadata page and the content is not changed in any way.

City Research Online:

<http://openaccess.city.ac.uk/>

publications@city.ac.uk

Supercritical, transcritical and subcritical real-fluid mixing at high-pressure conditions using the PC-SAFT EoS

Carlos Rodríguez Fernández

Thesis submitted for the fulfilment of the requirements for
the Degree of Doctor of Philosophy



CITY UNIVERSITY
LONDON

School of Mathematics, Computer Science &
Engineering

Department of Aeronautical and Mechanical Engineering

April, 2019

...to my family...

Abstract

The goal of this work is to develop a new numerical framework to simulate supercritical, transcritical and subcritical injections at Diesel engine relevant conditions using a compressible density-based solver of the Navier-Stokes equations, along with the conservative formulation of the energy equation. This new algorithm allows one to perform practical CFD simulations using complex EoS at affordable CPU times, and smooths-out the previously observed spurious pressure oscillations associated with fully conservative schemes when used along with real-fluid EoS. For the first time, the Perturbed Chain Statistical Associating Fluid Theory (PC-SAFT) equation of state (EoS) has been coupled with the Navier-Stokes equations, energy conservation equation and vapor liquid equilibrium (VLE) calculations in a numerical algorithm. This molecular based EoS is an alternative to cubic EoS, which show low accuracy when computing the thermodynamic properties of hydrocarbons at temperatures that are typical for today's high-pressure fuel injection systems. It only requires three empirically determined but well-known parameters (when the association term is neglected) to model the properties of a specific component without the need for extensive model calibration, as is typically the case when the NIST (REFPROP) library is utilised. Moreover, PC-SAFT can flexibly handle the thermodynamic properties of multi-component mixtures for which the NIST (REFPROP) library supports only limited component combinations. One-dimensional simulations (shock tube problems and advection test cases) were performed to validate the numerical framework against analytical /exact solutions. Nitrogen, n-dodecane and Diesel were used as working fluids. The properties of Diesel fuel have been modelled as: multicomponent surrogates comprising of four, five, eight and nine components divided into accuracy types, depending on how closely they match the composition of real Diesel; or as a pseudo-component obtained by applying a purely predictive method based on the PC-SAFT model. Published molecular dynamic simulations have been employed to demonstrate that the algorithm properly captures the multicomponent VLE interface at high-pressure conditions. Additionally, planar two-dimensional simulations of jets of nitrogen, n-dodecane, a four component Diesel surrogate and a Diesel pseudo-component are included to demonstrate the multidimensional, multispecies and multiphase capability of the developed numerical framework.

Present contribution

The novelty of the thesis can be summarised in the following points:

- **Numerical novelty**

A new numerical framework has been developed to simulate supercritical, transcritical and subcritical injections at Diesel engine relevant conditions, using a compressible density-based solver of the Navier-Stokes equations along with the conservative formulation of the energy equation. The proposed numerical approach improves the overall computational time of codes employing complex EoS and overcomes the previously observed spurious pressure oscillations associated with the utilisation of conservative schemes along with real-fluid EoS.

- **Complex thermodynamics coupling with N-S**

The PC-SAFT model has been coupled with the Navier-Stokes equations, energy conservation equation and VLE calculations in the developed numerical framework. No SAFT variant has been previously implemented in a CFD code. This molecular-based EoS presents multiple advantages for simulations that require accurate thermodynamic calculations over a wide range of conditions (e.g., Diesel injections).

Moreover, a purely predictive method that employs the PC-SAFT EoS for developing pseudo-components, which are defined to replicate the properties of complex hydrocarbon mixtures (e.g., diesel fuels), has been validated and completed to be used in CFD simulations. This methodology makes the simulation time independent of the number of compounds present in the fuel and thus, allowing the real composition of a specific fuel to be utilised in practical CFD simulations.

- **Cases simulated**

One-dimensional simulations (shock tube problems and advection test cases) were performed to validate the numerical framework against analytical/exact solutions. Additionally, planar two-dimensional simulations of supercritical, transcritical and subcritical injections were performed to demonstrate the multidimensional, multispecies and multiphase capability of the developed code. Nitrogen, n-dodecane and Diesel were used as working fluids. The properties of Diesel fuel were modelled as: multicomponent surrogates of four, five, eight and nine components divided into

accuracy types, depending on how closely they match the composition of real Diesel; or as a pseudo-component that replicates the properties of a specific multicomponent surrogate. To the best of the author's knowledge, this is the first time that real Diesel composition is considered in CFD simulations using a molecular based model. Moreover, published molecular dynamic simulations have been employed to demonstrate that the numerical framework properly captures the multicomponent VLE interface of subcritical injections at high-pressure conditions.

- **Major findings**

The results obtained by the PC-SAFT EoS to model Diesel shows the highest degree of agreement with experimental values in comparison with the results obtained applying the method developed at NIST. All the multi-component Diesel surrogates tested show different properties to n-dodecane, a working fluid commonly used in CFD simulations to model Diesel fuel. Simulations of supercritical and transcritical Diesel injections where the fuel is modelled as a multicomponent surrogate can be performed at affordable CPU times by computing the pressure and sonic fluid velocity in the cell centres and performing a reconstruction of these variables at each cell face to solve the Riemann problem. This technique has been found to smooth-out the spurious pressure oscillations associated with conservative schemes when used along with real-fluid EoS. In subcritical injections, due to computational requirements of calculating the VLE state of multiple components, it is necessary to model the Diesel surrogates as single pseudo-components to perform simulations at affordable CPU times. The pseudo-components developed correctly capture the evaporation process of the multicomponent Diesel surrogates in the VLE interface.

Acknowledgements

I would like to thank Professor Manolis Gavaises and PhD Phoivos Koukouvini for their expert advice and continuous encouragement throughout this project. I would also like to thank my colleagues in the IPPAD project for their wonderful collaboration. And finally, I would like to express my gratitude towards my parents, sister, partner and friends for their ongoing support over the last 3 years.

This project has received funding from the European Union Horizon-2020 Research and Innovation Programme with grant Agreement No 675528.

London, April 2019

Carlos Rodríguez Fernández

Contents

| | |
|--|-------|
| Abstract | v |
| Present contribution | vii |
| Acknowledgements | ix |
| Contents | xi |
| List of Figures | xiii |
| List of Tables..... | xviii |
| Nomenclature | xix |
| List of abbreviations | xix |
| List of Symbols..... | xx |
| Greek Letters..... | xxi |
| Superscripts..... | xxi |
| 1. Introduction | 1 |
| 1.1 Background and Motivation..... | 1 |
| 1.2 Real-fluid mixing at high-pressure conditions..... | 1 |
| 1.3 Supercritical and transcritical injections | 6 |
| 1.4 Subcritical injections (VLE interface)..... | 7 |
| 1.5 Conservative and quasi-conservative (pressure based) formulations..... | 9 |
| 1.6 Perturbed Chain-Statistical Associating Fluid Theory | 9 |
| 1.7 Diesel modelling..... | 12 |
| 1.8 Objectives..... | 13 |
| 1.9 Thesis outline | 13 |
| 2. Simulation of transcritical fluid jets using the PC-SAFT EoS..... | 15 |
| 2.1 Numerical method | 15 |
| 2.1.1 Formulations | 16 |
| 2.1.2 PC-SAFT EoS subroutine | 21 |
| 2.1.3 Peng-Robinson EoS and PC-SAFT EoS comparison..... | 22 |
| 2.2 Results | 23 |
| 2.2.1 One-dimensional cases | 23 |
| 2.2.2 Two-dimensional cases | 32 |
| 2.2.3 Hyperbolicity of Euler system with PC-SAFT EoS | 40 |
| 2.2.4 Pressure-composition phase diagram for the $N_2+C_{12}H_{26}$ system | 41 |
| 3. Simulation of supercritical Diesel jets using the PC-SAFT EoS | 43 |
| 3.1 Numerical method | 43 |

| | | |
|----------------|---|-----|
| 3.1.1 | Spatial reconstruction methods and Riemann solver | 44 |
| 3.1.2 | Diesel surrogates | 47 |
| 3.1.3 | Phase diagrams | 48 |
| 3.2 | Results | 48 |
| 3.2.1 | N-dodecane and Diesel comparison | 48 |
| 3.2.2 | Advection test cases | 49 |
| 3.2.3 | Shock tube problems | 53 |
| 3.2.4 | Two-dimensional cases | 57 |
| 3.3 | Conclusions | 62 |
| 4. | Simulation of subcritical Diesel jets at high-pressure conditions using the PC-SAFT EoS... 65 | |
| 4.1 | Numerical method | 65 |
| 4.1.1 | CFD Code | 65 |
| 4.1.2 | Diesel modelling | 66 |
| 4.1.3 | Thermodynamic solver (PC-SAFT + VLE) | 68 |
| 4.1.4 | VLE interface | 71 |
| 4.1.5 | Results | 73 |
| 4.2 | Conclusions | 81 |
| 5. | Conclusions and future work | 85 |
| 5.1 | Conclusions | 85 |
| 5.2 | Future work | 88 |
| Appendix | | 91 |
| Algorithm 1 | | 92 |
| Algorithm 2 | | 93 |
| Algorithm A | | 94 |
| Algorithm A(p) | | 100 |
| Algorithm B | | 101 |
| Stability | | 107 |
| TPn Algorithm | | 110 |
| VLE properties | | 113 |
| Publications | | 115 |
| References | | 117 |

List of Figures

| | |
|---|----|
| Figure 1.1: Experimental [33] and calculated pressure-composition phase diagram for the N ₂ (1) + C ₁₂ H ₂₆ (2) system. Solid lines: PC-SAFT EoS with $k_{ij} = 0.144$ [34] | 8 |
| Figure 1.2: Schematic representation of the attractive and repulsive contributions of the SAFT EoS and the PC-SAFT EoS [64] | 11 |
| Figure 2.1: Schematic representation of hyperbolic sub-step employing a fully conservative formulation [77] | 19 |
| Figure 2.2: Schematic representation of hyperbolic sub-step employing the double flux model [35] | 21 |
| Figure 2.3: Comparison of thermodynamic properties of n-dodecane at 6MPa computed using the PC-SAFT EoS and the Peng-Robinson EoS: (a) density, (b) sound speed, (c) internal energy | 23 |
| Figure 2.4: Advection Test Case 1 (N ₂), FC formulation, CFL = 0.5, u = 50 m/s, 100 cells, | 24 |
| Figure 2.5: Advection Test Case 1 (N ₂), FC formulation, CFL = 0.5, u = 50 m/s, 300 cells, t=0.01 s. Comparison of the (a) density, (b) temperature, (c) pressure and (d) x-velocity between the analytical and the numerical solution. | 25 |
| Figure 2.6: Advection Test Case 1 (N ₂), FC and QC formulations, CFL(FC) = 0.5, CFL(QC)=1.0, u = 50 m/s, 100 cells, t=0.02 s. Comparison of the (a) density, (b) temperature, (c) pressure and (d) x-velocity between the analytical and the numerical solution. | 26 |
| Figure 2.7: Advection Test Case 2 (N ₂), QC formulations, CFL = 1.0, u = 150 m/s, 100 cells, t=0.01s. Comparison of the (a) density, (b) temperature, (c) pressure and (d) x-velocity between the analytical and the numerical solution. | 27 |
| Figure 2.8: Advection Test Case 3 (N ₂ - Dodecane), QC formulations, CFL = 1.0, u = 100 m/s, 150 cells, t=0.01 s. Comparison of the (a) density, (b) temperature, (c) pressure and (d) x-velocity between the analytical and the numerical solution. | 28 |
| Figure 2.9: Relative energy conservation error of the QC formulation for the Advection Test Case 2 (Transcritical nitrogen) using the Peng-Robinson EoS (PR) and the PC-SAFT EoS. N is the number of cells employed. | 28 |
| Figure 2.10: Relative energy conservation error of QC formulation for the Advection Test Case 3 using the PC-SAFT EoS. N is the number of cells employed. | 29 |

| | |
|--|----|
| Figure 2.11: Advection Test Case 2 (N ₂), QC formulation, CFL = 1.0, u = 150 m/s, 100 cells, t=0.01s. Comparison of γ^* and $e0^*$ computed using the Peng Robinson EoS (PR EoS) and the PC-SAFT in the Advection Test Case 2. | 29 |
| Figure 2.12: Shock Tube Problem 1 (Dodecane), QC formulation, CFL = 1.0, 800 cells, t=0.2 ms. Comparisons of (a) density, (b) temperature, (c) velocity and (d) pressure profiles: exact solution and numerical solution..... | 30 |
| Figure 2.13: Shock Tube Problem 1 (Dodecane), FC formulation, CFL = 0.5, 4000 cells, t=0.2 ms. Comparisons of (a) density, (b) temperature, (c) velocity and (d) pressure profiles: exact solution and numerical solution..... | 31 |
| Figure 2.14: Shock Tube Problem 2 (Dodecane), QC formulation, CFL = 1.0, 800 cells, t=0.3 ms. Comparison of the (a) density, (b) temperature, (c) pressure, (d) x-velocity, (e) sound speed, (f) internal energy between the numerical solutions obtained using the Peng-Robinson EoS and the PC-SAFT EoS..... | 32 |
| Figure 2.15: 2D Test Case A, CFL = 1.0, 245000 cells, QC formulation. Density results of the simulation of the planar cryogenic nitrogen jet at various times. | 34 |
| Figure 2.16: Scatter plot of pressure as a function of density for the transcritical nitrogen jet (Case A). The vapor dome, non-convex region and the region with complex speed of sound (SOS) are included..... | 34 |
| Figure 2.17: Computational time employed to compute the solution of the transcritical nitrogen jet (Case A) at $t = 4 \times 10^{-4}$ employing a variable number of cells. | 35 |
| Figure 2.18: 2D Test Case A, CFL = 1.0, 245000 cells, QC formulation. Results of the simulation of the planar cryogenic nitrogen jet at $t = 4 \times 10^{-4}$ s using the quasi-conservative formulation: (a) density, (b) temperature, (c) pressure, (d) sound speed. | 36 |
| Figure 2.19: 2D Test Case B, CFL = 0.4, 180000 cells, FC formulation. Results of the simulation of the supercritical nitrogen jet at $t = 7.84 \times 10^{-4}$ s: (a) density, (b) pressure..... | 37 |
| Figure 2.20: 2D Test Case B solved using the FC and QC formulations. Scattered data of density and temperature. The nitrogen vapor dome is included..... | 37 |
| Figure 2.21: 2D Test Case C, CFL = 0.5, 180000 cells, FC formulation. Results of the simulation of the supercritical dodecane jet at $t = 2.5 \times 10^{-5}$ s: (a) density, (b) temperature, (c) pressure, (d) sound speed. | 39 |
| Figure 2.22: Scattered data of composition and temperature of the planar dodecane jet Case C. Solid lines are dodecane-nitrogen phase boundaries from VLE at 4.5 MPa and 6 MPa..... | 40 |

| | |
|---|----|
| Figure 2.23: The vapor dome, non-convex region and the region with complex speed of sound of dodecane computed using the PC-SAFT EoS. | 40 |
| Figure 3.1: Schematic representation of hyperbolic sub-step | 46 |
| Figure 3.2: Comparison of thermodynamic properties of n-dodecane and Diesel surrogates at 6MPa: (a) density, (b) sonic fluid velocity, (c) internal energy..... | 49 |
| Figure 3.3: Advection Test Case 1 (N2), CFL = 0.5, u = 10 m/s, 100 cells, t=0.04 s. Comparison of the (a-b) density, (c-d) pressure and (e-f) x-velocity between the analytical and the numerical solutions. Numerical solution 1: Pressure and sonic fluid velocity computed at the faces using the EoS. Numerical solution 2: Pressure and sonic fluid velocity interpolated at the faces. | 51 |
| Figure 3.4: Advection Test Case 1 (N2), CFL = 0.5, u = 10 m/s, 100 cells. Maximum wiggles amplitude in the velocity and pressure fields. Analysis of smooth and sharp initial interfaces using the second-order MUSCL-Hancock scheme. Numerical solution 1: Pressure and sonic fluid velocity computed at the faces using the EoS. Numerical solution 2: Pressure and sonic fluid velocity interpolated at the faces. | 52 |
| Figure 3.5: Advection Test Case 1 (N2), CFL = 0.5, u = 10 m/s, 100 cells. Maximum wiggles amplitude in the velocity and pressure fields. Analysis of smooth and sharp initial interfaces using the fifth-order WENO scheme. Numerical solution 1: Pressure and sonic fluid velocity computed at the faces using the EoS. Numerical solution 2: Pressure and sonic fluid velocity interpolated at the faces..... | 52 |
| Figure 3.6: Diesel surrogate V0a - nitrogen phase boundary from VLE at different pressures. . | 53 |
| Figure 3.7: Advection Test Case 2 (Diesel surrogate V0a – N2), CFL=0.5 u = 10 m/s, 500 cells, t=0.1s. Comparison of the (a) density, (b) temperature, (c) pressure and (d) x-velocity between the analytical and the numerical solution..... | 53 |
| Figure 3.8: Shock Tube Problem 1 (MUSCL-Hancock scheme, Dodecane). CFL = 0.5, u = 10 m/s, 1000 cells, t=5 10 ⁻⁴ s. Comparisons of (a) density, (b) temperature, (c) velocity and (d) pressure profiles: exact solution and numerical solutions. Numerical solution 1: Pressure and sonic fluid velocity computed at the faces using the EoS. Numerical solution 2: Pressure and sonic fluid velocity interpolated at the faces. | 55 |
| Figure 3.9: Shock Tube Problem 1 (Fifth-order WENO, Dodecane). CFL = 0.3, 1000 cells, t=5 10 ⁻⁴ s. Comparisons of (a) density, (b) temperature, (c) velocity and (d) pressure profiles: exact solution and numerical solutions. Numerical solution 1: Pressure and sonic fluid velocity | |

| | |
|---|----|
| computed at the faces using the EoS. Numerical solution 2: Pressure and sonic fluid velocity interpolated at the faces..... | 56 |
| Figure 3.10: Shock Tube Problem 2 (Dodecane). CFL = 0.3, 1000 cells, $t=5 \cdot 10^{-4}$ s..... | 56 |
| Figure 3.11: Shock Tube Problem 3 (Dodecane). CFL = 0.3, 1000 cells, $t=2.5 \cdot 10^{-4}$ s..... | 57 |
| Figure 3.12: Shock Tube Problem 4. CFL = 0.8, 800 cells, $t=2.5 \cdot 10^{-4}$ s. Comparison of the (a) density, (b) temperature, (c) pressure, (d) x-velocity, (e) sonic fluid velocity, (f) internal using as working fluids dodecane and the surrogate Diesels. | 58 |
| Figure 3.13: CFL = 0.5, 405000 cells. Results of the simulation of the supercritical n-dodecane jet at $t = 3.4 \cdot 10^{-5}$ s: (a) density, (b) temperature, (c) pressure. | 60 |
| Figure 3.14: Scattered data of composition and temperature of the planar dodecane jet, dodecane-nitrogen phase boundary from VLE at 4.5 MPa and isobaric-adiabatic mixing line.. | 60 |
| Figure 3.15: Percentage number of times the PC-SAFT model is solved in the hyperbolic operator respect a classic implementation of a FC formulation..... | 61 |
| Figure 3.16: Number of times the PC-SAFT is solved per cell in the first RK sub-time-step (RK1), the second RK sub-time-step (RK2), and the parabolic operator at $1.24 \cdot 10^{-5}$ s and $3.43 \cdot 10^{-5}$ s. | 61 |
| Figure 3.17: CFL = 0.5, 405000 cells. Results of the simulation of the supercritical Diesel surrogate V0a jet at $t = 3.4 \cdot 10^{-5}$ s: (a) density, (b) temperature, (c) pressure..... | 62 |
| Figure 4.1: Schematic representation of the CFD code | 68 |
| Figure 4.2: Schematic representation of the thermodynamic solver | 69 |
| Figure 4.3: Isobaric-adiabatic mixing lines at different pressures in the combustion chamber. 69 | |
| Figure 4.4: Experimental [33] and calculated pressure-composition phase diagram for the N2 (1) + C12H26 (2) system. Solid lines: PC-SAFT EoS with $k_{ij} = 0.144$. It was computed using the thermodynamic algorithm described in the Appendix. | 70 |
| Figure 4.5: Diesel engine compression cycles [22] and contours of dimensionless transition time on pressure-temperature diagram of n-dodecane [15]..... | 72 |
| Figure 4.6: Development of gas–liquid interface shown on VLE diagram at 20 MPa [15], VLE experimental data [33] and isobaric-adiabatic mixing lines. | 72 |
| Figure 4.7: Development of gas–liquid interface shown on VLE diagram at 1 MPa [15], VLE experimental data [33] and isobaric-adiabatic mixing line..... | 73 |

| | |
|---|----|
| Figure 4.8: Shock Tube Problem. CFL = 0.5, $u = 0$ m/s, 300 cells, $t=5 \cdot 10^{-4}$ s. Comparisons of (a) density, (b) temperature, (c) velocity and (d) pressure profiles: exact solution and numerical solutions. | 74 |
| Figure 4.9: Density predictions for the hydrocarbon mixture presented in Table 4.2. | 75 |
| Figure 4.10: Shock Tube Problem 2. CFL = 0.5, 800 cells, $t=5 \cdot 10^{-4}$ s. Comparison of the (a) density, (b) temperature, (c) pressure, (d) x-velocity, (e) sonic fluid velocity, (f) internal energy using as working fluids are a mixture of n-octane, n-dodecane and n-hexadecane (Table 4.2) and a pseudo-component that replicate the properties of the mixture (Table 4.3) [72]. | 76 |
| Figure 4.11: Advection Test Case 1 (N2- C ₁₂ H ₂₆), CFL = 0.5, $u = 10$ m/s, 100 cells. Results of (a) density, (b) temperature, (c) pressure and (d) VLE interface at 10^{-6} s. | 77 |
| Figure 4.12: Advection Test Case 2 (N2- V0a/ pseudo-Diesel V0a), CFL = 0.5, $u = 10$ m/s, 100 cells. Results of (a) density, (b) temperature, (c) speed of sound and (d) internal energy results at 10^{-6} s. | 78 |
| Figure 4.13: VLE Interface, Advection Test Case 2 (N2- V0a/ pseudo-Diesel V0a), CFL= 0.5, $u = 10$ m/s, 100 cells. Results of VLE interface at 10^{-6} s. | 79 |
| Figure 4.14: Advection Test Case 2 (N2- V0a/ pseudo-Diesel V0a). Results of VLE interface at 10^{-6} s and phase boundaries from VLE at 11MPa. | 79 |
| Figure 4.15: Advection Test Case 2 (N2- V0a/ pseudo-Diesel V0a), CFL = 0.5, $u = 10$ m/s, 100 cells. Results of (a) density, (b) temperature, (c) speed of sound and (d) internal energy results at 10^{-6} s. | 80 |
| Figure 4.16. Scattered data of composition and temperature of the planar n-dodecane jet, dodecane-nitrogen phase boundary from VLE at 11MPa and isobaric-adiabatic mixing line. | 81 |
| Figure 4.17: Density results of n-dodecane planar jet. | 82 |
| Figure 4.18: CFL = 0.5, 1,216,800 cells. Results of the simulation of the VOA Diesel pseudo-component jet at $t = 3.04 \times 10^{-5}$ s.: (a) density, (b) temperature, (c) pressure, and (d) overall vapor fraction on a molar basis. | 83 |

List of Tables

| | |
|--|----|
| Table 2.1: PC-SAFT pure component parameters [55]..... | 26 |
| Table 2.2: 1D Test Cases..... | 26 |
| Table 2.3: 2D Test Cases..... | 27 |
| Table 3.1: Comparison between experimentally measured surrogate densities (kg/m ³) at 293.15 K and 0.1MPa with the NIST and PC-SAFT predictions [71]...... | 47 |
| Table 3.2: Molar composition for the four Diesel fuel surrogates (V0a, V0b, V1, V2) [70] | 47 |
| Table 3.3: PC-SAFT pure component parameters [71], [86] | 48 |
| Table 3.4: ADVECTION TEST CASES | 50 |
| Table 3.5: SHOCK TUBE PROBLEMS | 54 |
| Table 3.6: 2D Test Cases..... | 57 |
| Table 4.1: PC-SAFT parameter correlations as a function of MW (g/mol) for n-alkanes and PNAs using the GC parameters of [86] | 67 |
| Table 4.2: Molar composition of hydrocarbon mixture employed in Shock Tube Problem 2 [72] | 75 |
| Table 4.3: PC-SAFT pure component parameters employed to model the pseudo-component employed in Shock Tube Problem 2 [72] | 75 |
| Table 4.4: Pseudo-component PC-SAFT parameters employed to model the pseudo-Diesel V0a using the correlations developed by utilizing the GC parameters of Tihic et al. [86]..... | 79 |

Nomenclature

List of abbreviations

| | |
|-----------|--|
| AAD | Average Absolute Deviation |
| CFD | Computational Fluid Dynamics |
| CFL | Courant–Friedrichs–Lewy |
| CPA | Cubic Plus Association |
| ECN | Engine Combustion Network |
| ENO | Essentially Non-Oscillatory |
| EoS | Equation of State |
| FC | Fully Conservative |
| GC | Group Contribution |
| HLLC | Harten-Lax-van Leer-Contact |
| HN/CN | Hydrogen-to-Carbon Ratio |
| LES | Large Eddy Simulation |
| MW | Number Averaged Molecular Weight |
| N-S | Navier-Stokes |
| PM | Particulate matter |
| PNAs | Poly-Nuclear Aromatics |
| PR | Peng-Robinson |
| PC-SAFT | Perturbed Chain Statistical Associating Fluid Theory |
| QC | Quasi-Conservative |
| RK2 | Second-order Runge–Kutta |
| SAFT-BACK | Boublik-Alder-Chen-Kreglewshi |
| SRK | Soave-Redlich-Kwong |
| SSP-RK3 | Third-order strong-stability-preserving Runge–Kutta |
| TPn flash | Isothermal-Isobaric Flash |
| TVD | Total Variation Diminishing |
| TPD | Tangent Plane Distance |
| VLE | Vapor-Liquid Equilibrium |
| WENO | Weighted Essentially Non-Oscillatory |

List of Symbols

| | |
|-------------------|---|
| A | Helmholtz free energy [J] |
| \tilde{a}^{res} | Reduced Helmholtz free energy [-] |
| c | Sound speed [m s ⁻¹] |
| d | Temperature-dependent segment diameter [Å] |
| e | Internal energy [J kg ⁻¹] |
| h | Enthalpy [J mol ⁻¹] |
| g | Radial distribution function [-] |
| I | Integrals of the perturbation theory [-] |
| J | Mass diffusion flux of species [-] |
| k_b | Boltzmann constant [J/K] |
| k_{ij} | Binary interaction parameter |
| m | Number of segments per chain [-] |
| \bar{m} | Mean segment number in the system [-] |
| M_M | Molecular weight [g/mol] |
| N_A | Avogadro's number [mol ⁻¹] |
| N | Total number of molecules [-] |
| p | Pressure [Pa] |
| R | Gas constant [J mol ⁻¹ K ⁻¹] |
| r | Radial distance between two segments [Å] |
| T | Temperature [K] |
| x_i | Mole fraction of component i [-] |
| x | Reduced radial distance between two segments [-] |
| y_i | Mass fraction of component i [-] |
| S | Wave speed [m/s] |
| w | Acentric factor [-] |
| Z | Compressibility factor [-] |
| \mathbf{U} | Conservative variable vector |
| \mathbf{F} | x-convective flux vector |
| \mathbf{G} | y-convective flux vector |
| \mathbf{F}_V | x-diffusive flux vector |
| \mathbf{G}_V | y-diffusive flux vector |
| \mathbf{W} | Primitive variable vector |

Greek Letters

| | |
|---------------|---|
| β | Overall fraction of vapour phase on a molar base [-] |
| ε | Depth of pair potential [J] |
| η | Packing fraction [-] |
| ρ | Density [kg/m ³] |
| ρ_m | Total number density of molecules [1/Å ³] |
| σ_d | Segment diameter [Å] |
| θ | Vapour volume fraction [-] |
| φ | Fugacity coefficient [-] |
| μ | Chemical potential [J mol ⁻¹] |
| μ_v | Dynamic viscosity [Pa s] |

Superscripts

| | |
|-----------|---|
| <i>EQ</i> | Equilibrium |
| disp | Contribution due to dispersive attraction |
| hc | Residual contribution of hard-chain system |
| hs | Residual contribution of hard-sphere system |
| id | Ideal gas contribution |
| <i>L</i> | Left |
| <i>R</i> | Right |

1. Introduction

1.1 Background and Motivation

Small soot particles or particulate matter (PM) inhaled in traffic and city centres [1] are related to adverse health effects like premature death, heart attacks, and strokes, as well as acute bronchitis and aggravated asthma among children. Moreover, the presence of soot in the atmosphere has been linked to regional as well as global climate change [2]. Passenger cars produce most of the emissions, but electrification can solve this issue. However, electric trucks cannot be directly used to replace the current fleet fueled practically by Diesel [3]. Road freight generates approximately 16% of the CO₂ emissions worldwide [3] and its demand is expected to grow +160% in tonne-kilometre by 2050 [4]. The study performed by [3], which explored the technical limits of electrification in the transportation sector using real data from the Swiss truck fleet, points out how its full electrification is particularly difficult to be carried out. Even when considerably improving the gravimetric energy density of the battery cells, three additional conditions must be met to have a high electrification potential: (1) a change in the maximum permissible weight; (2) to have access to a high-capacity grid for charging and (3) backing an intra-day energy infrastructure (such as swapping stations). Therefore, there is still a real need to improve our understanding of Diesel engines to continue reducing emissions until gradual replacement with electrification becomes effective in most sectors. The research presented in this document is part of the IPPAD project, which is focused on developing a systematic understanding of three emission reduction strategies: increasing pressure, use of additives and supercritical injection. In particular, this thesis explains how to couple the Perturbed-Chain Statistical Associating Fluid Theory (PC-SAFT) with the Navier-Stokes equations to simulate supercritical, transcritical and subcritical real-fluid mixing at high-pressure conditions with a special emphasis on Diesel injections.

1.2 Real-fluid mixing at high-pressure conditions

To correctly model the combustion in Diesel engines one needs to characterise the atomisation and mixing of sprays at high-pressure conditions. Even nowadays these processes are not completely understood.

According to the experiments performed by several authors [5]–[9], supercritical mixing exists at pressures near or slightly higher than the critical pressure of the liquid fuel. In [5], flashlight photography and high-speed cinematography were used to visualise cryogenic fluids

injected into several gases. It was observed that there was a notable difference between subcritical and supercritical injections. By increasing the ambient pressure, fluids reach a transcritical regime where surface tension does not play a role in the breakup and mixing phenomena. The behaviour is similar to viscous miscible fluids. The authors explained how the transition from subcritical to supercritical depends on the ambient composition and initial conditions and it is not determined by the critical pressure of the pure species. At low pressures, a LOX (Liquid Oxygen) jet showed a smooth interface, breaking up into non-spherical droplets. However, it presented stringy-like fluid structures that quickly dissolved at transcritical conditions.

[6] investigated the injection of cryogenic liquids at subcritical and supercritical pressures, relevant to liquid rocket engines. Shadowgraphy and spontaneous Raman scattering were employed to measure turbulent length scales, growth rates, core lengths, fractal dimensions and jet breakup regimes. In [6], it is explained that single round jets of cryogenic nitrogen injected into room temperature gaseous nitrogen at subcritical conditions show conventional spray features. However, they present a gas-like appearance at supercritical conditions.

[7] studied experimentally and analytically liquid jet injections into a quiescent gaseous environment from subcritical to supercritical conditions. At subcritical conditions, the process is controlled by the surrounding gas inertia and surface tension forces. It was observed material broke off from ligament formation and drops. At transcritical conditions, the formation of ligaments decreased with sporadic drop formation. At supercritical conditions, ligament formation was not detected demonstrating that surface tension does not play a role.

[8] investigated the behaviour of swirling supercritical hydrocarbon fuel (SCF) jets injected into nitrogen environments at temperatures and pressures that exceed the fuel critical values. The authors report that Gaussian mass concentration profiles and jet boundaries that scale with swirl number are similar to those of gas jets.

[9] presented a summary of experimental achievements relevant to liquid rockets, paying special attention to the injection of nonreacting cryogenic liquids into a high-pressure environment which exceeds the critical pressure of at least one of the propellants. The author stated that as the ambient pressure gets close to the injectant critical pressure and surpasses it, the influence of the surface tension decreases leading to the suppression of drop/ligament formation and liquid breakup. Instead, the jet describes a gas-like jet behaviour.

[10], [11] derived a mathematical model combining real-fluid thermodynamics and Linear Gradient Theory to specify under what conditions a classical non-continuum "jump" exists between the phases, or a continuous gas-liquid interfacial diffusion layer. According to the

results, high-temperature interfaces present a significantly reduced surface tension and a wider interface when compared to low-temperature interfaces. There is a reduction in the mean free molecular path and a broadening of the interfaces, which places the interface in the continuum length scale regime. Then, surface tension forces create a discontinuous interface that leads to the formation of primary atomization and secondary breakup (classic spray) at low ambient temperatures, supercritical fuel pressures, and constant chamber density. Ligaments and drops are present in the spray. However, a diffusive mixture process takes place at Diesel engine high-temperature conditions where there is a continuous phase transition from compressed liquid to supercritical mixture states. The lack of surface tension avoids the formation of drops and promotes a diffusion dominated mixing process. The jets evolve in the presence of large and continuous thermophysical gradients. The authors presented experimental images obtained at constant ambient density and at supercritical pressures with respect to the fuel where drop breakup processes appear at low ambient temperatures, but not at high ambient temperature conditions.

More recently, [12] investigated the atomization and mixing processes of sprays injected into progressively higher pressure and temperature ambient conditions. The Engine Combustion Network [13] Spray A single-hole injector was employed to inject n-dodecane into a combustion chamber that is optically accessible. Long-distance microscopy and diffused back-illumination were utilised to perform high-speed imaging to resolve ligament structures and droplets close to the nozzle. It was determined that the surface tension remains in effect at the gas–liquid interfaces in ambient conditions slightly above the critical point of the fuel. However, at higher pressure and temperature conditions the surface tension diminishes, as expected for supercritical fuel–air mixtures. Diesel engine operation conditions are in the diffused controlled mixing regime.

However, [14] carried out systematic measurements using high-speed long-distance microscopy for three single-component fuels (n-heptane, n-dodecane, n-hexadecane) injected into gas (89.71% N₂, 6.52% CO₂ and 3.77% H₂O) at elevated temperatures (700–1200 K) and pressures (2–11 MPa). The research is focused on understanding the transition from classical evaporation to supercritical fluid mixing. By increasing the ambient pressure and temperature, it was observed that classical atomization and vaporization change to another process where the surface tension forces are weaker. But there is not an immediate transition to diffusive mixing. In the near-nozzle region, subcritical liquid structures showed surface tension. After some time, the fuel experienced a transition to a dense miscible fluid. For n-dodecane and n-hexadecane, there was evidence of surface tension at all the conditions while n-heptane showed

supercritical fluid appearance from the nozzle outlet at the highest temperature and pressure conditions tested (1200 K, 10 MPa).

In [15] the evaporation of n-alkane fuels into nitrogen was investigated at different pressure and temperature conditions carrying out molecular dynamic simulations. The aim of this work was to understand how the transition from classical two-phase evaporation to one-phase diffusion-controlled mixing takes place. Two regimes are identified: (1) subcritical evaporation where a distinctive interface exists separating the liquid core and the ambient gases; and (2) supercritical evaporation where initially the liquid has a surface tension that decreases rapidly and vanishes. During the subcritical stage, the evaporation rate increases and reaches a maximum after which there is a transition to the supercritical stage. The results obtained have a high degree of agreement against the experimental results obtained by [14].

Numerous simulations of Diesel sprays in the literature exist, which employ Lagrangian methods considering a sharp gas-liquid interface which evolve according to primary and secondary breakup models and evaporation. [16] performed LES (Large Eddy Simulations) of Diesel spray in a constant volume vessel and in an internal combustion engine. A Eulerian-Lagrangian approach was employed including primary and secondary break-up, spray-induced turbulence (SIT) and the stochastic turbulence dispersion (STD) of parcels.

[17] simulated the Spray A benchmark case of the Engine Combustion Network. This is a n-dodecane spray into nitrogen at temperature and pressure conditions characteristic of Diesel engines. The jet was modelled using the transported probability density function (TPDF) method coupled with a time-dependent Reynolds-averaged $k-\epsilon$ turbulence model. A Lagrangian discrete phase model is utilised for the liquid spray.

[18] carried out LES of the Spray A as well. The liquid spray was modelled using a traditional Lagrangian method. The gas-phase reaction was modelled using a δ function combustion model.

[19] presented an implicit LES of the Spray A. A Lagrangian particle tracking approach was employed for the liquid phase. Mesh resolution effects were investigated as well as how the local and global flow characteristics are influenced by the droplet breakup model.

[20] utilised a Lagrangian-Eulerian framework to study the Subgrid-scale (SGS) model performance and grid resolution effects on fuel spray simulations. However, all these configurations present some limitations to accurately capture dense flow regimes near the nozzle where the liquid fuels disintegrate into ligaments that then form droplets. Additionally, Lagrangian methods are sensitive to calibration parameters and, there is no quantitative experimental droplet size measurements at Diesel engine conditions [21].

In [22], [23], a Eulerian density-based methodology was used to model the primary atomisation of the injected liquid accounting for compressibility effects associated with the high-pressure and injection velocity.

According to the work of [10]–[12], [24], when ambient pressure surpasses the fuel critical pressure, interfacial diffusion layers appear due to the reduction of the mean free molecular, reduction of surface tension forces, and thickening of the gas-liquid interfaces. The interfaces enter the continuum length scale and disappear when the mixture temperature is higher than its critical temperature value. Due to these reasons, a single-phase dense-gas approach (using the Peng-Robinson (PR) EoS) was employed in these publications. The simulation presents large and continuous thermodynamics (totally different from classical assumptions). It should be noted that phase separation was not included. However, n-dodecane/nitrogen mixtures are TYPE IV, which means that the critical temperature of the mixture is higher than the lower critical temperature of the components and lower than the higher critical temperature of the compounds. On the other hand, the critical pressure is higher than the critical pressure of the components [25]. Considering that the pressures that can be found in the combustion chamber of Diesel engines are lower than the critical pressure of some nitrogen/fuel mixtures, the VLE state must be included in the simulation.

[26] used a compressible Eulerian numerical model to perform LES of internal nozzle flow and downstream gas phase mixing in a single domain. The authors utilised a simplified approach for describing saturation lines in a pressure-volume diagram. The PR EoS was employed in these simulations.

In [21], [27] a multi-species two-phase model was developed using LES for accounting the turbulent mixing under high pressures. They implemented a thermodynamic solver which can compute the properties of a homogenous mixture in supercritical or subcritical states. The LES including VLE thermodynamics of the so-called Spray A shows a high degree of agreement against the available experimental data. Although according to [14], [15] the Spray A ambient conditions (900K, 6MPa) fall in the classic evaporation regime, the authors justified the use of a diffuse interface due to the high Weber number and low Stokes number (small droplet diameters and low surface tension).

1.3 Supercritical and transcritical injections

A single-species fluid or a mixture reaches a supercritical state when the pressure and temperature surpass its critical properties. In the critical region, repulsive interactions overcome the surface tension resulting in the existence of a single-phase that exhibits properties of both gases and liquids (e.g., gas-like diffusivity and liquid-like density). The injection of the Diesel in a compressed liquid state in the combustion chamber provokes the formation of droplets that are not completely evaporated and combust. By injecting the fuel in a supercritical state or with a temperature slightly lower than critical, the evaporation step can be avoided. The fuel-air mixing is improved as the diffusivity is much higher than that of molecules in a liquid phase, thus reducing the emissions of particulate matter and nitrogen oxides [28]–[30]. The reason why the fuel has to be injected at a high temperature is that Diesel/nitrogen mixtures are a TYPE IV mixture [25]. The critical temperature of the mixture is higher than the lower critical temperature of the components and lower than the higher critical temperature of the compounds. Starting at the critical point of n-dodecane (considering n-dodecane as a Diesel surrogate), the critical pressure of a N₂ + n-dodecane mixture grows by increasing the nitrogen concentration [31] and reaches higher pressures than the ones observed in Diesel engine combustion chambers, see Figure 1.1. Thus, to avoid the VLE state the fuel must be injected at a temperature higher than its critical value (supercritical) or slightly lower (transcritical) [32].

To simulate such cases, commonly diffuse interface methods are employed [21], [33], [34]. Three main difficulties are associated with these numerical simulations: (i) the treatment of large density gradients, (ii) the need to use a real-fluid EoS and (iii) the elimination of spurious pressure oscillations, typically occurring in simulations when fully conservative (FC) schemes are employed along with real-fluid EoS [35]. With regards to large density gradients, high order reconstruction methods can be used to describe sharp changes. In [36] the authors performed a two-dimensional large-eddy simulation (LES) of supercritical mixing and combustion employing a fourth-order flux-differencing scheme and a total-variation-diminishing (TVD) scheme in the spatial discretization. Similarly, in [37] a fourth-order central differencing scheme was applied together with a fourth-order scalar dissipation; this was found to stabilize the simulation of a cryogenic fluid injection and mixing under supercritical conditions. Moreover, in the work of [38] an eighth-order finite differencing scheme was employed to simulate homogeneous isotropic turbulence under supercritical pressure conditions. Furthermore, in [39] a density-based sensor was employed, which switches between a second-order ENO (Essentially non-oscillatory) and first-order scheme to suppress the oscillations.

Moving to the second issue, typically cubic EoS models like the PR [40] and Soave-Redlich-Kwong (SRK) [41] are used in supercritical and transcritical simulations. For example, in [34], [42]–[44] the SRK EoS was employed to close the Navier-Stokes equations and compute the fluid properties under supercritical and transcritical conditions. Similarly, in [33], [35], [39], [45] the non-ideal fluid behavior was modelled by applying the PR EoS. Nevertheless, cubic models commonly present low accuracy for computing the thermodynamic properties of hydrocarbons at high density ranges and temperatures that are typical for today's high pressure fuel injection systems [21].

[21] pointed out the issues of employing cubic EoS like PR and SRK modelling hydrocarbons at temperatures found in injection system [32], [46], [47]. Due to the 8.6% error (when compared to NIST) in the density prediction of n-dodecane at 363K (using PR) it was necessary to increase the injection velocity to match the mass-flow measurement leading to error in the velocity prediction of 50 m/s. The authors highlighted the possibility of using the developed numerical framework to simulate internal nozzle flow and jet breakup at the same time. However, the large error that cubic EoS present at high density ranges (especially in the sonic fluid velocity [46]) can be an important issue. These problems could be overcome by applying the PC-SAFT EoS [32], [46], [48]. This molecular-based EoS only requires three empirically determined parameters (when the association term is neglected) to model the properties of a specific component without the need for extensive model calibration, as is typically the case when the NIST library is used. In addition, PC-SAFT presents high accuracy when modelling the thermodynamic properties of multi-component mixtures while the NIST library presents limited component combinations.

Referring to the third issue, different QC (quasi-conservative) formulations were developed to avoid spurious pressure oscillations. However, the error in the conservation of the energy that these formulations present can be an issue for Diesel injection simulations where the temperature plays a significant role on determining the ignition time (see Section 1.5).

1.4 Subcritical injections (VLE interface)

If the fuel is not injected in a supercritical state or with a temperature slightly lower than its critical value (transcritical) the evaporation step cannot be avoided as the critical pressure of fuel/nitrogen mixtures is significantly higher than the pressures that can be found in a Diesel engine, see Figure 1.1 (considering n-dodecane as a Diesel surrogate). In [15], molecular simulations of three n-alkane fuels into nitrogen under various temperatures and pressures have been performed in order to study the injection, evaporation and mixing processes of

hydrocarbon fuels into a supercritical environment. The study was focused on understanding the transition from classical two-phase evaporation to one- phase diffusion-controlled mixing. Using as a dimensionless transition time (the time needed to transit from subcritical to supercritical respect to the liquid lifetime) of 0.35 as a threshold, the authors identified two regions on the P-T diagram, see Figure 4.5. Supercritical dominated: Due to the high critical pressures of TYPE IV mixtures, a VLE state is present at the beginning of the evaporation process. The temperature of the liquid core goes up until the VLE state disappears and only a diffusion-controlled mixing process exists. Subcritical dominated: A clear interface exists between the liquid core and the ambient gases. Nitrogen is not able to diffuse into the liquid core (constant fuel mass fraction close to 1 during evaporation, see Figure 4.7). There is a gradual decrease of the density of the liquid core as the fuel is heated up. The evaporation reaches a constant state with a constant liquid core. According to the classification presented by [15], the combustion chamber of a Diesel engine working at medium-high load operation conditions is in the supercritical dominated regime after the compression cycle, see Figure 4.5. At these ambient conditions, the nitrogen is able to rapidly diffuse into the liquid core (Figure 4.6) indicating that the interface has a Knudsen-number low enough to fall within the fluid mechanic continuum domain [11]. The results obtained have a high degree of agreement against the experimental results obtained by [14].

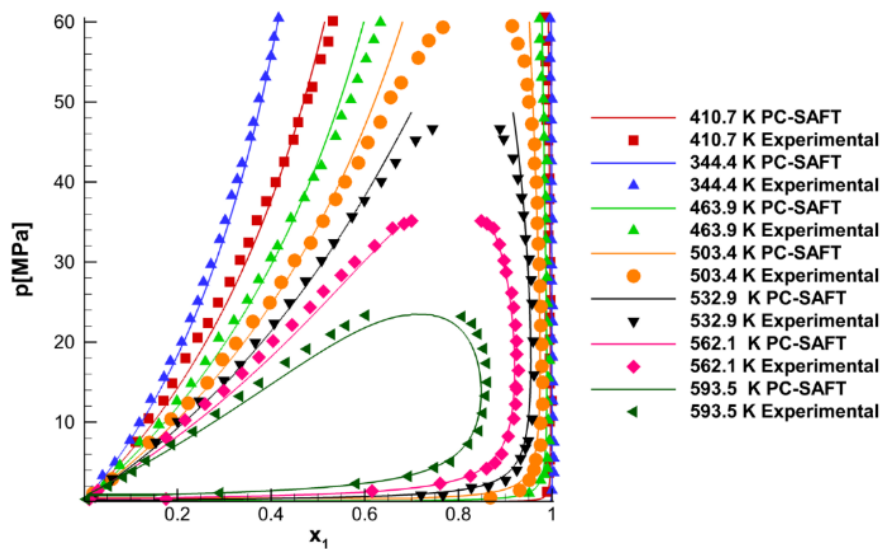


Figure 1.1: Experimental [49] and calculated pressure-composition phase diagram for the N₂ (1) + C₁₂H₂₆ (2) system. Solid lines: PC-SAFT EoS with $k_{ij} = 0.144$ [46]

1.5 Conservative and quasi-conservative formulations

If a FC formulation is employed along with a real-fluid EoS, spurious pressure oscillations may appear; the work of [34] has related this problem to computational stability issues, turbulence, and acoustics accuracy loss. The same authors of [34] developed a QC scheme solving a pressure evolution equation instead of the energy conservation equation, while [50] developed a QC framework where the artificial dissipation terms in the mass, momentum and energy equations are related and the pressure differential is considered to be zero. In [51] the double flux model was developed to avoid spurious pressure oscillations in simulations of compressible multicomponent flows that employ a perfect gas EoS; [52] extended it to reactive flows; and finally, [33], [35], [53] extended the double flux model to real-fluids and transcritical conditions. The use of the double-flux model of [33], [35], [53] can significantly reduce the required computational time if a complex EoS is employed as it is employed only once in the hyperbolic operator of the numerical model per time step [46]. However, recently it has been reported that the large energy conservation error in QC schemes produces an unphysical quick heat-up of the jet [21] and thus, making these schemes inadequate for Diesel injection simulations where the temperature plays a significant role on determining the ignition time. [32] proposes a modification to the calculation of the pressure and sonic fluid velocity at the cell faces in FC formulations; this is found to smooth-out the spurious pressure oscillations observed with previous methods. Additionally, it reduces the overall computational time allowing simulations of multicomponent Diesel surrogate fuels to be performed using complex EoS.

1.6 Perturbed Chain-Statistical Associating Fluid Theory

To simulate Diesel engine injections, the thermodynamic properties of the working fluids must be modelled with high accuracy over a wide range of conditions. Moreover, the EoS should be able to characterize the compounds using a small number of easily available parameters. Perturbation theories from statistical mechanics supposed an important advancement towards this kind of models [54]. In these theories, the thermodynamic properties of a system are mostly determined by the repulsive interactions of the molecules. A hard spheres system (which present only repulsive interactions) is commonly used as a reference. The deviations of the real system from the reference system (e.g., van der Waals attractive interactions, association interactions, polar or quadrupolar interactions or the non-spherical shape of the molecules) are

modelled as perturbations of the repulsive reference system. Numerous models of this type are based on SAFT. In this theory, each molecule is represented as a chain of tangent spherical segments. Different perturbation contributions are added to the Helmholtz energy of the hard-sphere reference system (A^{hs}): the hard-sphere chain formation of m segments to consider the non-spherical shape of molecules (A^{chain}); non-specific attractive interactions of the m (non-bonded) spherical segments (A^{disp}); and very short-range, strong attractive interactions like association (A^{assoc}). The total Helmholtz energy can be written as:

$$A^{res} = mA^{hs} + mA^{disp} + A^{hs} + A^{assoc} \quad (1)$$

The SAFT variant employed in this research is the PC-SAFT [55], [56]. In this model, the dispersion term is obtained applying a perturbation theory of second order to a reference system of hard chains instead of hard spheres to consider the influence on the number of intermolecular interactions of the molecule non-spherical shape. The hard-chain and association contributions are the same ones as the SAFT model. Then, the total Helmholtz energy is expressed as:

$$A^{res} = A^{hc} + A^{disp}(m) + A^{assoc} \quad (2)$$

Brief explanation of each contribution (PC-SAFT) [54]:

1) *Hard-Chain Contribution (A^{hc})*

The hard-chain reference fluid is formed of spherical segments without attractive interactions. The expression developed by [57] is used to describe the Helmholtz energy of this reference system. It is based on Wertheim's first-order thermodynamic perturbation theory [58]–[60]. It is modelled using two parameters, the number of segments (m) and the diameter of segments (σ).

2) *Dispersion Contribution (A^{disp})*

The dispersion contribution in PC-SAFT is computed by applying the perturbation theory of [61], [62] to the hard-chain reference system. Then, the non-spherical shape of molecules is considered on the attractive dispersion interactions. An additional parameter, the dispersion energy parameter (ε/k), is considered for describing the segment-segment interaction.

3) *Association Contribution (A^{assoc})*

The association model developed in [57], [63] is employed to calculate the contribution due to short-range association interactions (hydrogen bonding). It is considered that each molecule has one or more association sites, which can form hydrogen bonds. Two additional parameters are used to describe the association between two association sites: the association energy ($\varepsilon^{A_i, B_i}/k$), and the effective volume of an association interaction (k^{A_i, B_i}). Five pure-component parameters are needed to characterize an associating compound.

Figure 1.2 shows a schematic representation of the attractive and repulsive contributions of the SAFT EoS and the PC-SAFT EoS.

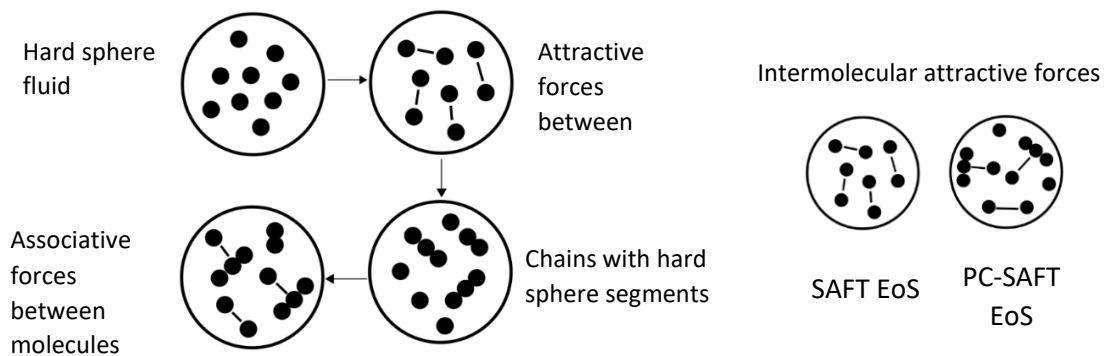


Figure 1.2: Schematic representation of the attractive and repulsive contributions of the SAFT EoS and the PC-SAFT EoS [64]

Several publications have highlighted the advantages of the SAFT models with respect to cubic EoS. [65] shows how the PC-SAFT model presents better results than cubic EoS predicting gas phase compressibility factors and oil phase compressibility. For example, AAD (Average Absolute Deviation) of the gas compressibility factors in the range $P=0-1000$ bar and $T=0-250$ °C for nC_6 are 0.0144 for PC-SAFT, 0.0479 for SRK (applying the Peneloux volume correction) and 0.0425 for PR (applying the Peneloux volume correction). For nC_5 , they are 0.0127, 0.0529 and 0.0296 respectively. [66] indicated that the PC-SAFT EoS shows a superior performance to the Cubic Plus Association (CPA) EoS in correlating second order derivative properties, such as speed of sound, dP/dV and dP/dT derivatives, heat capacities and the Joule–Thomson coefficient in the alkanes investigated. The CPA model presents a diverging behaviour in the speed attributed to the wrong description of the dP/dV derivative. AADs for speed of sound employing n -dodecane as working fluid at $T_r=0.5$ and $p=73$ MPa are 26% and 14%, utilising the CPA and PC-SAFT EoS respectively. Similarly, [67] points out the superiority of the SAFT-BACK (Boublik-Alder-Chen-Kreglewshi) model over the PR EOS. The SAFT-BACK EoS shows reasonable results for the

speed of sound in the vapor and liquid phases (AAD% = 2.3%, 2.1%, and 1.8% for methane, ethane, and propane, respectively). However, the results obtained by PR EOS are only similar to measured data at low pressure conditions. The predicted values by PR EOS at high density ranges present an AADs for methane, ethane, and propane of 28.6%, 14.7%, and 61.2%, respectively. Moreover, in [68] it was shown how cubic EoS predict a linear increase of the Z factor (compressibility factor) with pressure, while the PC-SAFT EoS presents a pressure dependence.

The main issues with using a complex EoS are the difficult implementation and the high computational cost [33]. Some tabulation methods have been developed for single-species cases [69] but these approaches cannot be utilised with mixtures of more than two components. Some of the surrogates employed in this research have four, five, eight and nine components so employing tables is not an option. The use of the double-flux model of [33], [35], [53] can significantly reduce the required computational time as the complex EoS is employed only once in the hyperbolic operator of the numerical model per time step [46]. However, the large energy conservation error in QC schemes is an important issue. The FC formulation proposed in [32] reduces the number of times the EoS is employed, making it possible to use complex EoS in affordable CPU time.

1.7 Diesel modelling

We have considered the A^{hc} and A^{disp} contributions. Intermolecular interaction terms accounting for segment self- or cross-associations (A^{assoc}) are not added due to the molecular structure of the surrogate Diesel compounds utilised. Then, three pure component parameters are enough to model the Diesel (m , σ and ε/k).

$$A^{res} = A^{hc} + A^{disp}(m) \quad (3)$$

Two approximations have been considered to model the properties of the fuel working fluids:

Multicomponent Diesel surrogates

[70] proposed four Diesel surrogates divided into two accuracy types depending on how close their composition is to real Diesel. V0a and V0b are two low-accuracy surrogates and V1 and V2 are the two high-accuracy surrogates. As pointed out in [71], the PC-SAFT EoS shows the highest degree of agreement with the experimental values in comparison with the results obtained [70] using the model developed at NIST for the employed Diesel surrogates. [32] shows a comparison of the thermodynamic properties of n-dodecane and the Diesel surrogates V0a, V0b, V1 and V2 at 6MPa, as calculated using the PC-SAFT EoS. The main differences between n-

dodecane and the Diesels can be found in the temperature and sonic fluid velocity at high densities. The temperature is an important thermodynamic property in transcritical simulations because it determines the transition to a supercritical state. The sonic fluid velocity plays a key role in the computation of the hyperbolic fluxes and in the time step calculation. The effects that these variables have in the CFD results can be seen in [32].

Pseudo-component method

[72] developed a technique that defines a single pseudo-component to represent the compounds found in a hydrocarbon mixture. It only requires two mixture properties as inputs, the number averaged molecular weight and the hydrogen-to-carbon ratio. The computational requirements are considerably reduced by decreasing the number of components solved in the PC-SAFT model.

1.8 Objectives

The objectives of this thesis can be summarized as follows:

- To develop a CFD code capable of simulating supercritical, transcritical and subcritical injections at Diesel engine relevant conditions.
- To couple the PC-SAFT model with the N-S and total energy conservation equations in a density-based numerical framework.
- To include VLE calculations in the developed model, which allows us to simulate injections where the fuel enters the combustion chamber at temperatures that are typical for Diesel injection systems.
- To consider real-fuel composition when modelling Diesel in the CFD simulations performed.
- To improve the overall computational time of codes employing complex EoS.

1.9 Thesis outline

The main body of this thesis has been divided into three chapters:

Simulation of transcritical and supercritical fluid jets using the PC-SAFT EoS

This chapter describes a numerical framework to simulate transcritical and supercritical flows utilising the compressible form of the Navier-Stokes equations coupled with the PC-SAFT EoS; both conservative and quasi-conservative formulations have been tested. Advection test cases and shock tube problems are included to show the overall performance of the developed

framework employing both formulations. Additionally, two-dimensional simulations of nitrogen and n-dodecane jets are presented to demonstrate the multidimensional capability of the developed model.

Simulation of supercritical and transcritical Diesel jets using the PC-SAFT EoS

The properties of Diesel fuel are modelled as surrogates comprising four, five, eight and nine components. The proposed FC numerical approach improves the overall computational time and overcomes the previously observed spurious pressure oscillations associated with the utilisation of conservative schemes. In the absence of experimental data, advection test cases and shock tube problems are included to validate the developed framework. Finally, two-dimensional simulations of planar jets of n-dodecane and a four component Diesel surrogate are included to demonstrate the capability of the developed methodology to predict supercritical and transcritical Diesel fuel mixing into air.

Simulation of subcritical Diesel jets at high-pressure conditions using the PC-SAFT EoS

This section presents a numerical framework that combines PC-SAFT and VLE calculations in a density-based solver of the Navier-Stokes equations to perform multicomponent two-phase simulations of Diesel injections at subcritical high-pressure conditions. Published molecular dynamic simulations have been employed to demonstrate that the algorithm properly captures the multicomponent VLE interface. A purely predictive method that employs the PC-SAFT EoS for developing pseudo-components, which are defined to replicate the properties of complex hydrocarbon mixtures (*e.g.*, diesel fuels), has been tested. The computational requirements are considerably reduced by decreasing the number of components solved in the molecular-based model. Advection test cases and shock tube problems were performed to validate the numerical framework. Two-dimensional simulations of planar Diesel jets are performed to demonstrate the capability of the developed methodology to model subcritical mixing at high pressure Diesel engine conditions.

2. Simulation of transcritical fluid jets using the PC-SAFT EoS

The present chapter describes a numerical framework to simulate transcritical and supercritical flows utilising the compressible form of the Navier-Stokes equations coupled with the PC-SAFT EoS; both conservative and quasi-conservative formulations have been tested [46]. This molecular model is an alternative to cubic EoS which show low accuracy computing the thermodynamic properties of hydrocarbons at temperatures typical for high pressure injection systems. Liquid density, compressibility, speed of sound, vapor pressures and density derivatives are calculated with more precision when compared to cubic EoS. Advection test cases and shock tube problems are included to show the overall performance of the developed framework employing both formulations. Additionally, two-dimensional simulations of nitrogen and n-dodecane jets are presented to demonstrate the multidimensional capability of the developed model.

2.1 Numerical method

The Navier-Stokes equations for a non-reacting multi-component mixture containing N species in a x-y 2D Cartesian system are given by:

$$\frac{\partial \mathbf{U}}{\partial t} + \frac{\partial \mathbf{F}}{\partial x} + \frac{\partial \mathbf{G}}{\partial y} = \frac{\partial \mathbf{F}_v}{\partial x} + \frac{\partial \mathbf{G}_v}{\partial y} \quad (4)$$

The vectors of eq. 5 are:

$$\mathbf{U} = \begin{bmatrix} \rho Y_1 \\ \vdots \\ \rho Y_N \\ \rho u \\ \rho v \\ \rho E \end{bmatrix}, \mathbf{F} = \begin{bmatrix} \rho u Y_1 \\ \vdots \\ \rho u Y_N \\ \rho u^2 + p \\ \rho u v \\ (\rho E + p)u \end{bmatrix}, \mathbf{G} = \begin{bmatrix} \rho v Y_1 \\ \vdots \\ \rho v Y_N \\ \rho v u \\ \rho v^2 + p \\ (\rho E + p)v \end{bmatrix}, \mathbf{F}_v = \begin{bmatrix} J_{x,1} \\ \vdots \\ J_{x,N} \\ \sigma_{xx} \\ \sigma_{xy} \\ u\sigma_{xx} + v\sigma_{xy} - q_x \end{bmatrix}, \quad (5)$$

$$\mathbf{G}_v = \begin{bmatrix} J_{y,1} \\ \vdots \\ J_{y,N} \\ \sigma_{yx} \\ \sigma_{yy} \\ u\sigma_{yx} + v\sigma_{yy} - q_y \end{bmatrix}$$

where ρ is the fluid density, u and v are the velocity components, p is the pressure, E is the total energy, J_i is the mass diffusion flux of species i , σ is the deviatoric stress tensor and q is the diffusion heat flux vector.

The finite volume method has been applied in this work for obtaining a numerical solution to the above equations. The PC-SAFT EoS is implemented to simulate supercritical and transcritical states. The developed numerical framework considers a condition of thermodynamic equilibrium in each cell. Phase separations or metastable thermodynamic states are beyond the scope of this chapter and are not considered.

2.1.1 Formulations

Since PC-SAFT EoS is rarely used in CFD simulations, two codes have been developed employing different formulations (conservative and quasi-conservative) to determine which one is more appropriate for the simulation of transcritical and supercritical fluid jets.

Conservative formulation

Operator splitting [73] is adopted to divide the physical processes into hyperbolic and parabolic sub-steps. The global time step is computed using the CFL (Courant–Friedrichs–Lewy) criterion of the hyperbolic operator.

- **Hyperbolic sub-step**

Approximate Riemann Solver

The HLLC (Harten-Lax-van Leer-Contact) solver is used to solve the Riemann problem [74]. For a one-dimensional and single-component case, the HLLC flux are given by:

$$\mathbf{F}^{\text{HLLC}} = \begin{cases} \mathbf{F}_L & \text{if } 0 \leq S_L, \\ \mathbf{F}_{*L} = \mathbf{F}_L + S_L(\mathbf{U}_{*L} - \mathbf{U}_L) & \text{if } S_L \leq 0 \leq S_*, \\ \mathbf{F}_{*R} = \mathbf{F}_R + S_R(\mathbf{U}_{*R} - \mathbf{U}_R) & \text{if } S_* \leq 0 \leq S_{*R}, \\ \mathbf{F}_R & \text{if } 0 \geq S_{*R}, \end{cases} \quad (6)$$

The left and right wave speeds (S_L and S_R) are computed as:

$$S_L = \min(u_L - c_L, u_R - c_R), \quad (7)$$

$$S_R = \max(u_L + c_L, u_R + c_R)$$

where c is the sound speed.

The star states are computed as:

$$\mathbf{U}_{*K} = \rho_K \begin{pmatrix} \frac{S_K - u_K}{S_K - S_*} \\ \frac{1}{S_*} \\ \frac{E_K}{\rho_K} + (S_* - u_K) \left(S_* + \frac{p_K}{\rho_K(S_K - u_K)} \right) \end{pmatrix} \quad (8)$$

where $K = R, L$

The speed in the middle wave is computed as:

$$S_* = \frac{p_R - p_L + \rho_L u_L (S_L - u_L) - \rho_R u_R (S_R - u_R)}{\rho_L (S_L - u_L) - \rho_R (S_R - u_R)} \quad (9)$$

Spatial reconstruction

Fifth-order WENO scheme

The conservative variables may be interpolated onto the cell faces using a fifth-order WENO scheme [75] due to its high order accuracy and non-oscillatory behavior. The interpolation of the variable Q to the cell edge $i + 1/2$ from the left is:

$$Q_{i+\frac{1}{2}} = \sum_{k=0}^r \omega_k^r Q_{k,i+\frac{1}{2}}^r \quad (10)$$

where r is the number of points used in each stencil, k is the individual stencil number and ω_k^r is the weighting factor of the k th stencil. The interpolation on each candidate stencil is:

$$Q_{k;i+\frac{1}{2}}^r = \sum_{j=0}^{r-1} a_{kj}^r Q_{i-r+k+j+1} \quad (11)$$

The candidate stencil weights are calculated as:

$$\omega_k^r = \frac{\alpha_k^r}{\sum_{j=0}^{r-1} \alpha_j^r} \quad (12)$$

where:

$$\alpha_k^r = \frac{C_k^r}{(I_{S_k} + \varepsilon)^p} \quad (13)$$

ε is a parameter used to avoid division by 0.

The smoothness coefficients are given by:

$$IS_k = \sum_{l=0}^{r-1} \sum_{j=0}^{r-1} d_{klj}^r Q_{i-r+k+l+1} Q_{i-r+k+j+1} \quad (14)$$

The coefficients $a_{kj}^r, C_k^r, d_{klj}^r$ can be obtained from [75].

Following the work of [73], the limiter developed by [76] is employed. Defining the slope limited interpolation as:

$$Q_{i+\frac{1}{2}} = Q_i + 0.5(Q_i - Q_{i-1})\phi_{TVD} \quad (15)$$

where ϕ is the TVD slope limiter:

$$\phi_{TVD} = \max \left[0, \min \left(\alpha, \alpha \frac{Q_{i+1} - Q_i}{Q_i - Q_{i-1}}, 2 \frac{\hat{Q}_{i+1/2} - Q_i}{Q_i - Q_{i-1}} \right) \right] \quad (16)$$

being $\hat{Q}_{i+1/2}$ the interpolated variable using the WENO scheme and α a constant set to two [73].

Second-order spatial reconstruction

The MUSCL-Hancock scheme [74] is applied. Data cell averages of the conservative variables are replaced by piece-wise linear functions in each cell:

$$\mathbf{U}_i(x) = \mathbf{U}_i^n + \frac{(x-x_i)}{\Delta x} \mathbf{\Delta}_i^C, x \in [0, \Delta x] \quad I_i = [x_{i-1/2}, x_{i+1/2}] \quad (17)$$

where $\mathbf{\Delta}_i^C$ is the slope vector of the conservative variables. The Minmod slope limiter is applied:

$$\mathbf{\Delta}_i^C = \text{minmod}(q_i - q_{i-1}, q_{i+1} - q_i)$$

$$\text{min mod}(a, b) = \begin{cases} a & |a| < |b| \text{ \& } ab > 0 \\ b & \text{if } |a| > |b| \text{ \& } ab > 0 \\ 0 & ab < 0 \end{cases} \quad (18)$$

The boundary extrapolated values of the conservative variables in global coordinates are computed using:

$$\mathbf{U}_i^L(x) = \mathbf{U}_i^n + \frac{1}{2} \mathbf{\Delta}_i^C \quad (19)$$

$$\mathbf{U}_i^R(x) = \mathbf{U}_i^n - \frac{1}{2} \mathbf{\Delta}_i^C$$

Time integration

The temporal integration is performed either using a second-order Runge–Kutta (RK2):

$$\frac{\partial \mathbf{U}}{\partial t} = -\frac{\partial \mathbf{F}}{\partial x} - \frac{\partial \mathbf{G}}{\partial y} = H_{xy} \quad (20)$$

$$\mathbf{U}^{(1)} = \mathbf{U}^n + \Delta t H_{xy}(\mathbf{U}^n),$$

$$\mathbf{U}^{n+1} = \frac{1}{2} \mathbf{U}^n + \frac{1}{2} [\mathbf{U}^{(1)} + \Delta t H_{xy}(\mathbf{U}^{(1)})] \quad (21)$$

or a third order strong-stability-preserving Runge–Kutta (SSP-RK3) [77]:

$$\mathbf{U}^{(1)} = \mathbf{U}^n + \Delta t H_{xy}(\mathbf{U}^n),$$

$$\mathbf{U}^{(2)} = \frac{3}{4} \mathbf{U}^n + \frac{1}{4} [\mathbf{U}^{(1)} + \Delta t H_{xy}(\mathbf{U}^{(1)})],$$

$$\mathbf{U}^{n+1} = \frac{1}{3} \mathbf{U}^n + \frac{2}{3} [\mathbf{U}^{(2)} + \Delta t H_{xy}(\mathbf{U}^{(2)})] \quad (22)$$

Figure 2.1 shows a representation of how the convective fluxes are computed using the fully conservative formulation.

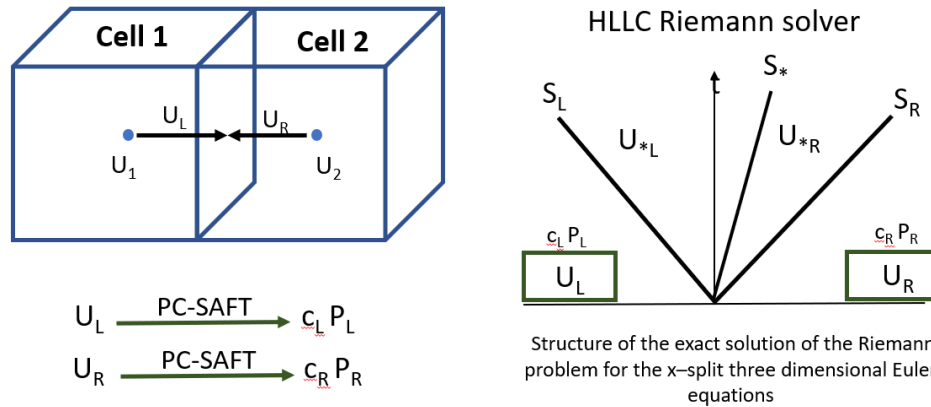


Figure 2.1: Schematic representation of hyperbolic sub-step employing a fully conservative formulation [74]

- **Parabolic sub-step.**

The method developed in [78] is applied to calculate the values of the dynamic viscosity and thermal conductivity of the mixture. The model of [79] is implemented to compute the diffusion coefficient. A RK2 (second-order Runge–Kutta) scheme is employed to perform the time integration of this sub-step. Linear interpolation is performed for computing the conservative variables, enthalpy and temperature on faces from cell centres.

Quasi-conservative formulation

The physical processes are divided into hyperbolic and parabolic sub-steps using operator splitting as well [73]. The CFL criterion of the hyperbolic operator is used to compute the global time step.

- *Hyperbolic sub-step.*

The double flux model of [33], [35], [53] has been implemented. The HLLC solver is used to solve the Riemann problem. In the one-dimensional cases presented, the primitive variables are interpolated onto the cell faces using a fifth-order WENO scheme [75]. In the two-dimensional cases, a sensor that compares the value of the density in the faces and the centre of the cells is employed to determine in which regions a more dissipative scheme must be applied [33]. If the sensor is activated, TVD limiters [73] are employed. The solution is then blended with a first-order scheme (90% WENO). Time integration is performed using a SSP-RK3 method [77].

The following steps were followed to implement the double flux model:

1) In each cell the values of γ^* and e_0^* are stored.

$$\gamma^* = \frac{\rho c^2}{p} \quad (23)$$

$$e_0^* = e - \frac{pv}{\gamma^*-1} \quad (24)$$

where p is the pressure, c is the sound speed, e is the internal energy and v is the specific volume.

2) Runge-Kutta scheme

a) The fluxes at the faces are computed using the primitive variables. The total energy in the left (L) and right (R) states are computed using eq.25.

$$(\rho E)_{L,R}^n = \frac{p_{L,R}^n}{\gamma_j^{*n}-1} + \rho_{L,R}^n e_{0,j}^{*,n} + \frac{1}{2} \rho_{L,R}^n \mathbf{u}_{L,R}^n \cdot \mathbf{u}_{L,R}^n \quad (25)$$

b) Update conservative variables using the RK scheme

c) Update primitive variables (using the double flux model to compute the pressure).

3) Update total energy: The total energy is updated from primitive variables based on the EoS (eq.26). Only at this point the PC-SAFT EoS is used to compute the internal energy, sound speed, temperature and enthalpy.

$$\rho E = \rho e + \frac{1}{2} \rho \mathbf{u} \cdot \mathbf{u} \quad (26)$$

Figure 2.2 presents a visual representation of how the convective fluxes are calculated employing the double flux model.

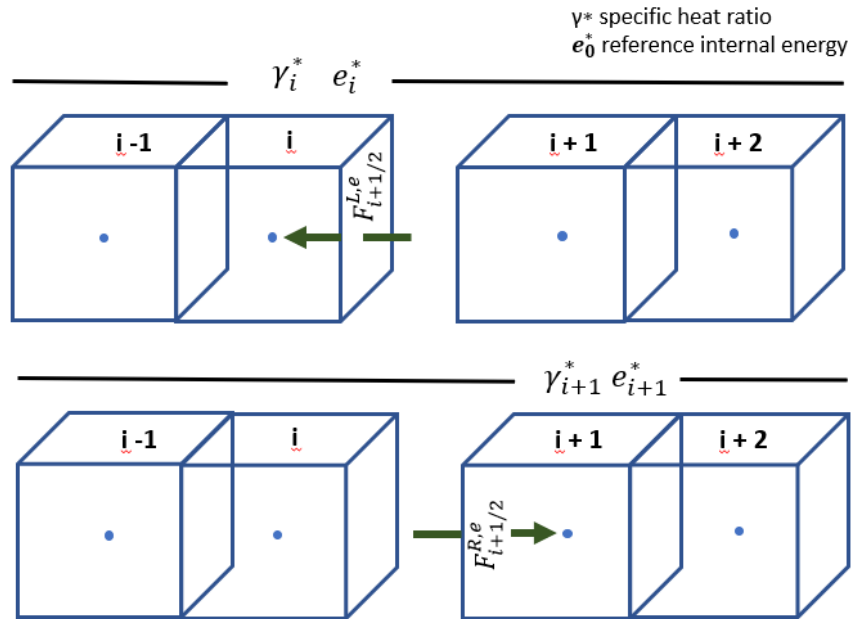


Figure 2.2: Schematic representation of hyperbolic sub-step employing the double flux model [33]

- **Parabolic sub-step**

The diffusion fluxes are calculated conservatively in the same way that is explained in the conservative formulation.

2.1.2 PC-SAFT EoS subroutine

A different subroutine has been developed for each formulation because of the different inputs of the EoS subroutine.

Conservative formulation

The thermodynamic variables computed in the CFD code by the PC-SAFT EoS are the temperature, pressure, sound speed and enthalpy. The algorithm inputs are the density, internal energy, molar fractions and three pure component parameters per component (number of segments per chain, energy parameter of each component and segment diameter), see Table

2.1. The density and the internal energy are obtained from the conservative variables of the CFD code. The molar fractions are computed using the mass fractions employed in the continuity equations and the molar weights of the components. The pure component parameters are specified in the initialization of the simulation. A Newton method is employed to compute the temperature that is needed to calculate the value of all other thermodynamic variables. The temperature dependent function used in the iterative method is the internal energy (Appendix: Algorithm A).

Quasi-conservative formulation

The thermodynamic variables computed in the CFD code by the PC-SAFT EoS are the temperature, internal energy, sound speed and enthalpy. The algorithm inputs are the density, pressure, molar fractions and three pure component parameters per component. The density and mass fractions (used to compute the molar fractions) are obtained from the conservative variables. The pressure is obtained employing the double flux model. The temperature is iterated until the difference between the pressure computed with the PC-SAFT model and the value obtained from the double flux model is lower than 0.001Pa (Appendix: Algorithm A(p)).

2.1.3 Peng-Robinson EoS and PC-SAFT EoS comparison

The most attractive feature of the PC-SAFT EoS is the better prediction of derivative properties such as compressibility and speed of sound. [67] shows the inaccuracy of cubic models to predict second derivative properties such as isobaric heat capacity and sound velocity in hydrocarbons at high density ranges. In the case of the sonic fluid velocity, the AAD% (Average Absolute Deviation) by PR EoS for methane, ethane, and propane are 28.6%, 14.7%, and 61.2%, respectively.

Figure 2.3 presents a comparison of the thermodynamic properties of n-dodecane at 6MPa computed using the PC-SAFT EoS and the Peng-Robinson EoS. NIST (REFPROP) library [80] has been used as reference due to its extensive validation with experimental data. While the results of both EoS are quite similar at density values lower than 550 Kg/m³, there is a significant difference at higher densities, especially in the sound speed. Cubic models commonly present low accuracy computing the thermodynamic properties of hydrocarbons at temperatures typical of injection systems [21]. However, the PC-SAFT EoS shows an accuracy similar to NIST without the need of an extensive model calibration as only three parameters are needed to model a specific component. Another advantage is the possibility of computing the thermodynamic properties of mixtures; NIST has limited mixture combinations.

2.2 Results

Initially, advection test cases and shock tube problems are solved to validate the hyperbolic part of the numerical framework employing the conservative and quasi-conservative formulations, while the parabolic part is omitted. Following, two-dimensional simulations of transcritical and supercritical nitrogen and n-dodecane jets are presented, including the parabolic part, to prove the multi-dimensional capability of the code.

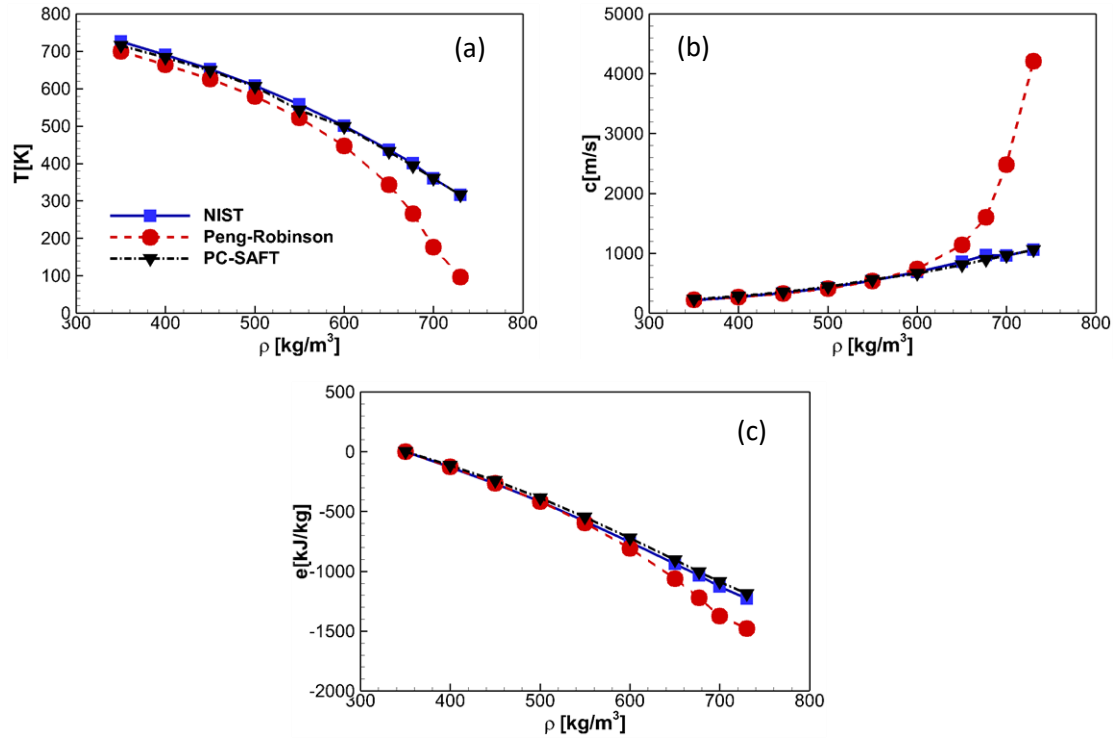


Figure 2.3: Comparison of thermodynamic properties of n-dodecane at 6MPa computed using the PC-SAFT EoS and the Peng-Robinson EoS: (a) density, (b) sound speed, (c) internal energy

2.2.1 One-dimensional cases

Advection test cases

Conservative formulation

Figure 2.4 shows the results of the supercritical Advection Test Case 1, see Table 2.2. Nitrogen is used as working fluid (The critical properties of nitrogen are $p_{c,N_2} = 3.4$ MPa and $T_{c,N_2} = 126.2$ K). The computational domain is $x \in [0, 1]$ m; the initial conditions in $0.25m < x < 0.75m$ are $\rho=250$ kg/m³, $p=5$ MPa, and $T=139.4$ K; in the rest of the domain are $\rho=45.5$ kg/m³, $p=5$ MPa, and $T=367.4$ K. The advection velocity applied is 50m/s; periodic boundary conditions are utilized; a uniform grid spacing of 0.01m is employed; the simulated time is $t=0.02s$; and the CFL

is set to be 0.5. Four spatial discretization schemes are compared: fifth-order WENO, second-order (based on the Minmod limiter), first order and a blend of the fifth-order WENO and the first-order schemes (95% WENO and rest 1st order).

The oscillations are more severe when high-order reconstruction schemes are applied. By blending a high-order scheme and a low-order model, dissipation can be used to smooth the numerical solution. If the advection test case is initialized using a smooth profile no spurious pressure oscillation appear in the solution as the sharp jumps in the thermodynamic properties between cells are avoided, see Figure 2.5. The smooth initial interface was generated as described in [42] using eq.27.

$$q = q_L(1 - f_{sm}) + q_R f_{sm} \quad (27)$$

$$f_{sm} = \frac{(1 + \text{erf}[\Delta R/\varepsilon])}{2} \quad (28)$$

Where L and R refers to the left and right states respectively and ΔR is the distance from the initial interface. $\varepsilon = C_\varepsilon \Delta x$, where Δx is the grid spacing and C_ε is a free parameter to determine the interface smoothness set to be 8.

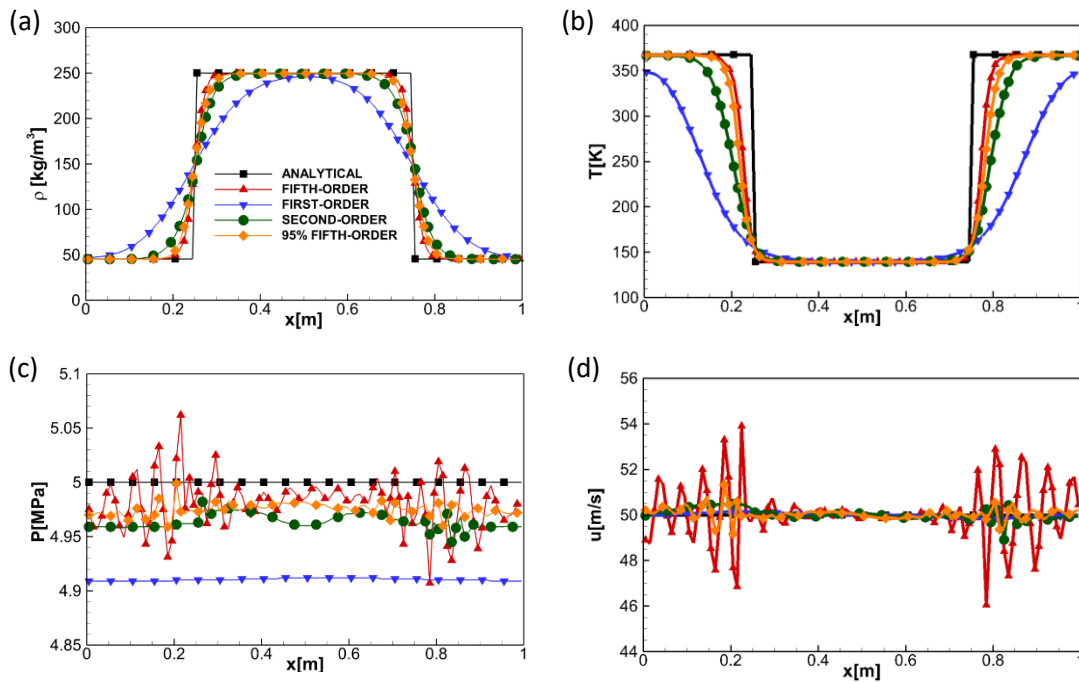


Figure 2.4: Advection Test Case 1 (N₂), FC formulation, CFL = 0.5, u = 50 m/s, 100 cells, t=0.02 s. Comparison of the (a) density, (b) temperature, (c) pressure and (d) x-velocity between the analytical and the numerical solution.

Quasi-conservative formulation

Figure 2.6 presents the results of the transcritical Advection Test Case 1 solved using the QC formulation. The advection velocity applied is 50m/s; periodic boundary conditions are applied; a uniform grid spacing of 0.01m is used; the simulated time is $t=0.02s$; and the CFL is set to be 1. Unlike the fully conservative scheme, spurious pressure oscillations are not present in the solution.

Figure 2.7 presents the results of the transcritical Advection Test Case 2 where nitrogen is used as working fluid, see Table 2.2. The computational domain is $x \in [0, 1]$ m; the initial conditions in $0.25 \text{ m} < x < 0.75 \text{ m}$ are $\rho=804.0 \text{ kg/m}^3$, $p=4 \text{ MPa}$, and $T=84.41 \text{ K}$; in the rest of the domain the initial conditions are $\rho=45.5 \text{ kg/m}^3$, $p=4 \text{ MPa}$, and $T=299.0 \text{ K}$. The advection velocity utilized is 100 m/s; periodic boundary conditions are used; the computational domain is $x \in [0, 1]$ m; 150 cells are employed; the simulated time is $t=0.01 \text{ s}$; a fifth-order WENO discretization scheme is used; and the CFL is set to be 1.0. It can be observed how large density gradients are solved without spurious pressure oscillations applying the double flux model.

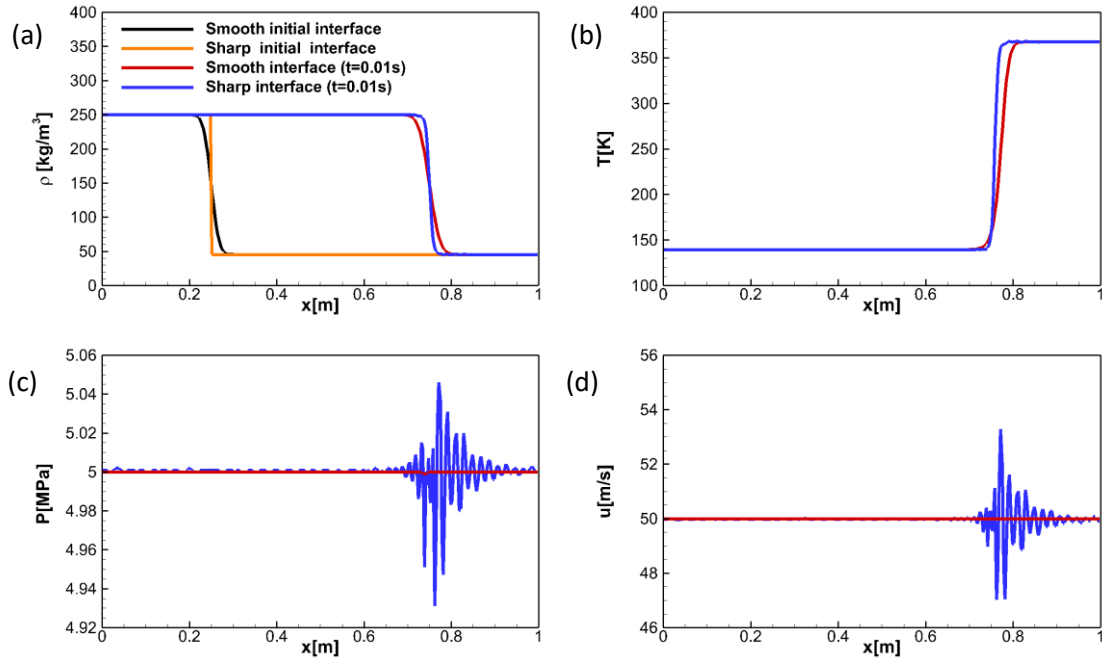


Figure 2.5: Advection Test Case 1 (N₂), FC formulation, CFL = 0.5, $u = 50 \text{ m/s}$, 300 cells, $t=0.01 \text{ s}$. Comparison of the (a) density, (b) temperature, (c) pressure and (d) x-velocity between the analytical and the numerical solution.

Figure 2.8 shows the results of the transcritical advection of n-dodecane at supercritical pressure and subcritical temperature ($p_{c,n\text{-dodecane}} = 1.817 \text{ MPa}$, $T_{c,n\text{-dodecane}} = 658.1 \text{ K}$) in supercritical nitrogen, Advection Test Case 3 (Table 2.2). The computational domain is $x \in [0,1]$ m; the initial conditions in $0.25 \text{ m} < x < 0.75 \text{ m}$ are $\rho_{n\text{-dodecane}} = 700.0 \text{ kg/m}^3$, $p_{n\text{-dodecane}} = 6 \text{ MPa}$, and

$T_{n\text{-dodecane}}=360.1$ K; in the rest of the domain $\rho_{N_2}=20.0$ kg/m³, $p_{N_2}=6$ MPa, and $T_{N_2}=965.7$ K. The advection velocity utilized is 100 m/s; periodic boundary conditions are used; 150 cells are employed; the simulated time is $t=0.01$ s; a fifth-order WENO discretization scheme is used; and the CFL is set to be 1.0. Unlike conservative codes, velocity and pressure equilibriums are preserved in multicomponent cases if the double flux model is applied.

Table 2.1: PC-SAFT pure component parameters [55]

| | m | $\sigma[\text{\AA}]$ | $\varepsilon/k[K]$ |
|------------|--------|----------------------|--------------------|
| nitrogen | 1.2053 | 3.3130 | 90.96 |
| n-dodecane | 5.3060 | 3.8959 | 249.21 |

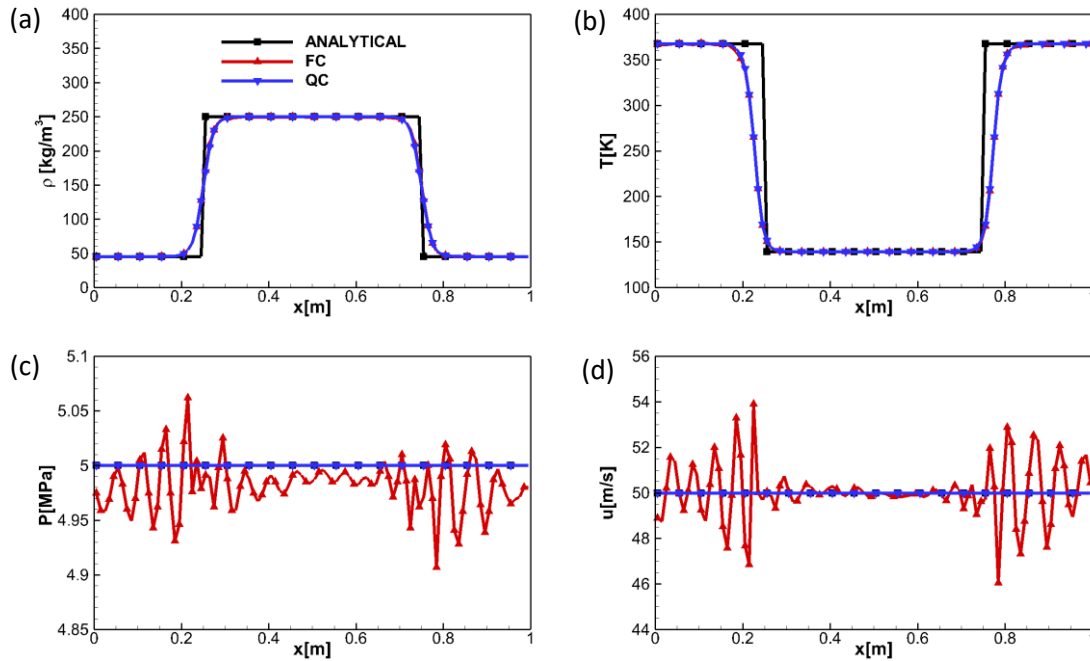


Figure 2.6: Advection Test Case 1 (N_2), FC and QC formulations, $CFL(FC) = 0.5$, $CFL(QC)=1.0$, $u = 50$ m/s, 100 cells, $t=0.02$ s. Comparison of the (a) density, (b) temperature, (c) pressure and (d) x-velocity between the analytical and the numerical solution.

Table 2.2: 1D Test Cases

| ADVECTION TEST CASES | | | |
|-----------------------------|------------------|------------------------------|-------------------|
| CASE 1 | Pressure [MPa] | Density [kg/m ³] | Temperature [K] |
| 0.25 m < x < 0.75 m | N_2 , 5 | N_2 , 250 | N_2 , 139.4 |
| 0.25 m > x or x > 0.75 m | N_2 , 5 | N_2 , 45.5 | N_2 , 367.4 |
| CASE 2 | | | |
| 0.25 m < x < 0.75 m | N_2 , 4 | N_2 , 804 | N_2 , 84.4 |
| 0.25 m > x or x > 0.75 m | N_2 , 4 | N_2 , 45.5 | N_2 , 299.0 |
| CASE 3 | | | |
| 0.25 m < x < 0.75 m | n-dodecane, 6.0 | n-dodecane, 700.0 | n-dodecane, 360.1 |
| 0.25 m > x or x > 0.75 m | N_2 , 6.0 | N_2 , 20.0 | N_2 , 965.7 |
| SHOCK TUBE PROBLEM | | | |
| PROBLEM | Pressure [MPa] | Density [kg/m ³] | Temperature [K] |
| x < 0.5 m | n-dodecane, 13.0 | n-dodecane, 700.0 | n-dodecane, 372.8 |
| x > 0.5 m | n-dodecane, 6.0 | n-dodecane, 150.0 | n-dodecane, 944.4 |

Table 2.3: 2D Test Cases

| CASE A | Pressure [MPa] | Density [kg/m ³] | Temperature [K] |
|---------|-----------------------|------------------------------|------------------------|
| JET | N ₂ , 4.0 | N ₂ , 804.0 | N ₂ , 84.4 |
| CHAMBER | N ₂ , 4.0 | N ₂ , 45.5 | N ₂ , 299.5 |
| CASE B | | | |
| JET | N ₂ , 4.0 | N ₂ , 440.0 | N ₂ , 127.0 |
| CHAMBER | N ₂ , 4.0 | N ₂ , 44.5 | N ₂ , 305.0 |
| CASE C | | | |
| JET | n-dodecane, 11.1 | n-dodecane, 450.0 | n-dodecane, 687.2 |
| CHAMBER | N ₂ , 11.1 | N ₂ , 37.0 | N ₂ , 972.9 |

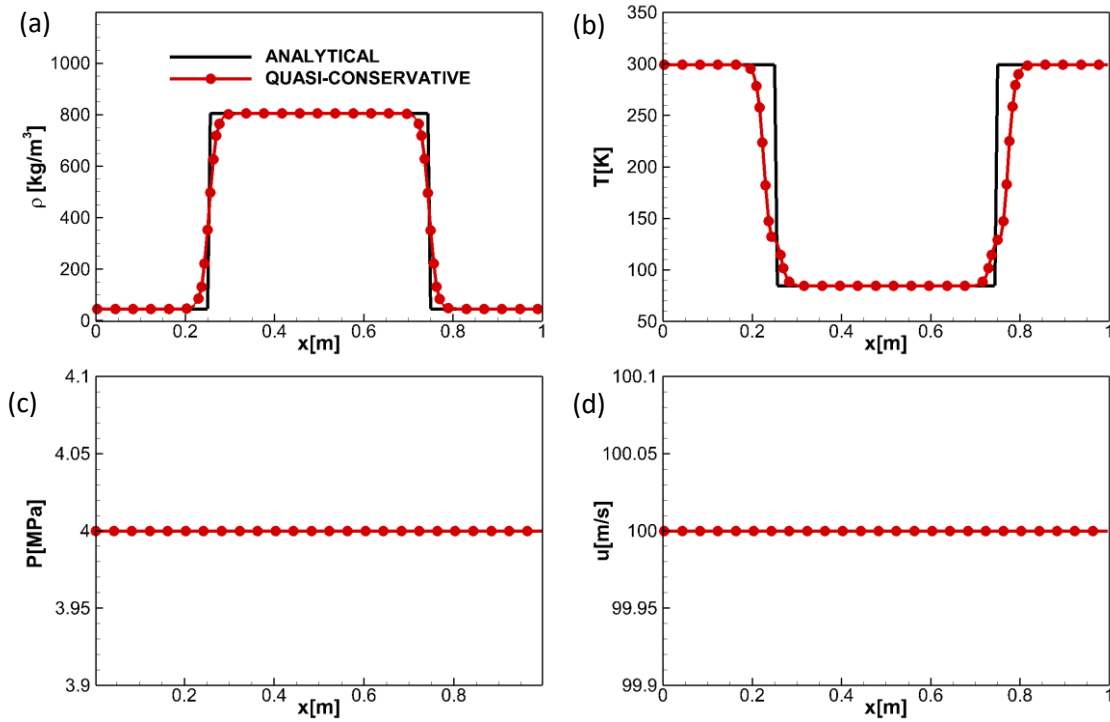


Figure 2.7: Advection Test Case 2 (N₂), QC formulations, CFL = 1.0, u = 150 m/s, 100 cells, t=0.01s. Comparison of the (a) density, (b) temperature, (c) pressure and (d) x-velocity between the analytical and the numerical solution.

Energy conservation error in the quasi-conservative formulation

The evolution of the energy conservation error of the Advection Test Case 2 is presented in Figure 2.9 . The error has been evaluated employing eq.29 [33].

$$\varepsilon = \left| \frac{\int_{\Omega} [(\rho E)(t) - (\rho E)(0)] dx}{\int_{\Omega} (\rho E)(0) dx} \right| \quad (29)$$

where ε is the relative error of the total energy with respect to initial conditions and Ω is the computational domain.

The energy conservation error is higher using the PC-SAFT EoS than Peng-Robinson EoS. This is related to the fact that the profiles of γ^* and e_0^* are smoother employing the cubic model. There are sharper jumps in internal energy and speed of sound employing the PC-SAFT EoS, see Figure 2.11. The error in the conservation of the energy depends on the jumps in the variables $1/(\gamma^* - 1)$ and e^* [33]. A convergence of the error to 0 exists increasing the refinement.

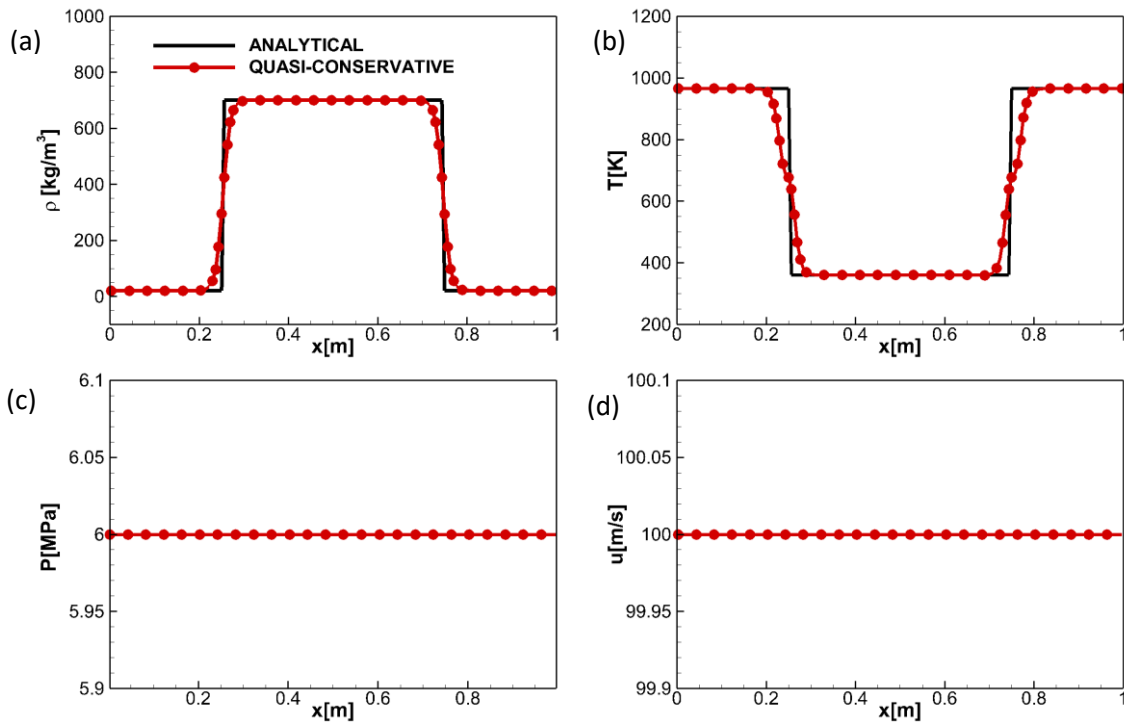


Figure 2.8: Advection Test Case 3 (N_2 - Dodecane), QC formulations, CFL = 1.0, $u = 100$ m/s, 150 cells, $t=0.01$ s. Comparison of the (a) density, (b) temperature, (c) pressure and (d) x-velocity between the analytical and the numerical solution.

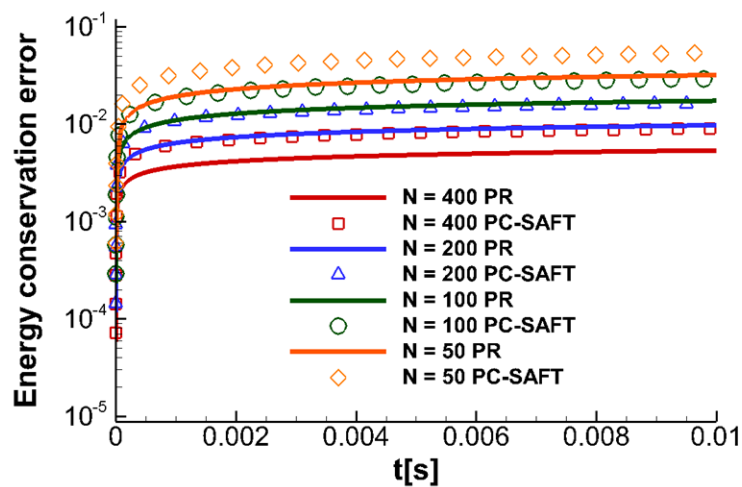


Figure 2.9: Relative energy conservation error of the QC formulation for the Advection Test Case 2 (Transcritical nitrogen) using the Peng-Robinson EoS (PR) and the PC-SAFT EoS. N is the number of cells employed.

Figure 2.10 presents the evolution of the energy conservation error of the Advection Test Case 3. Because of the different thermodynamic properties of the components, a higher energy conservation error than in the single-species cases appears. Although, a convergence to 0 is observed in one-dimensional cases increasing the refinement like in the single-species cases.

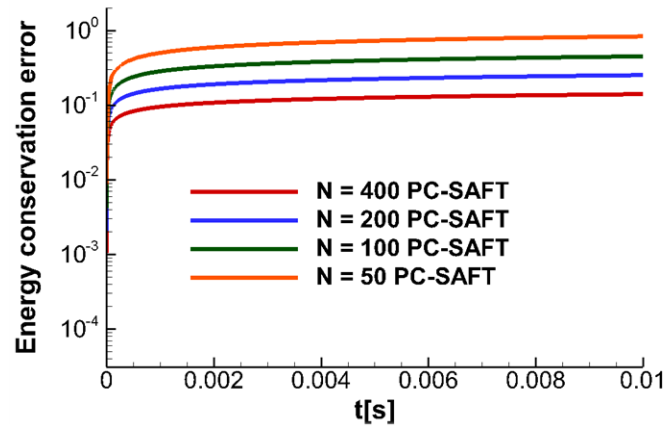


Figure 2.10: Relative energy conservation error of QC formulation for the Advection Test Case 3 using the PC-SAFT EoS. N is the number of cells employed.

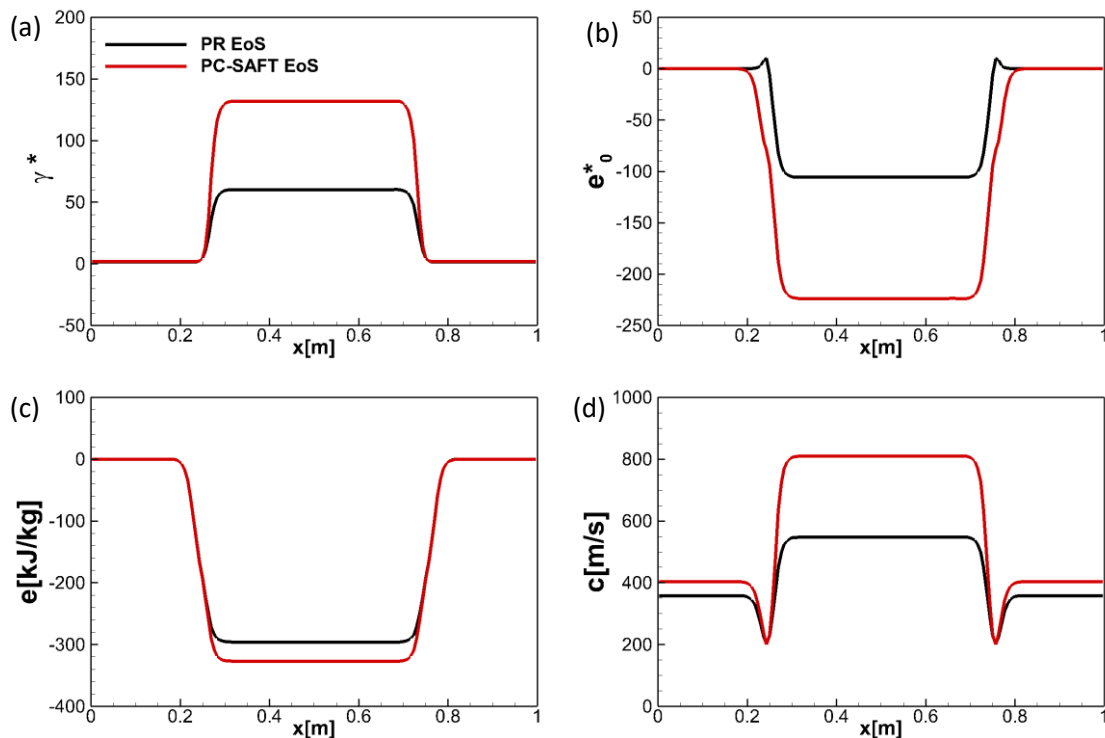


Figure 2.11: Advection Test Case 2 (N_2), QC formulation, CFL = 1.0, $u = 150$ m/s, 100 cells, $t=0.01$ s. Comparison of γ^* and e_0^* computed using the Peng Robinson EoS (PR EoS) and the PC-SAFT in the Advection Test Case 2.

Shock tube problems

The Euler equations are solved in this validation so a direct comparison with the exact solver can be done. The exact solution has been computed using the methodology described in [81].

Quasi-conservative formulation

The domain is $x \in [0, 1]$ m. The working fluid employed is n-dodecane. A fifth-order WENO scheme is employed to interpolate the primitive variables onto the cell faces. 800 equally spaced cells were used. Wave transmissive boundary conditions are implemented in the left and right sides. The double flux model is applied. The pressure exceeds the critical value in all the domain while there is a transition in the temperature from subcritical to supercritical from left to right. The initial conditions in the left state are $\rho_L=700 \text{ kg/m}^3$, $p_L=13 \text{ MPa}$, $u_L=0 \text{ m/s}$; and in the right state are $\rho_R=150 \text{ kg/m}^3$, $p_R=6 \text{ MPa}$, $u_R=0 \text{ m/s}$. The simulated time is $t=0.2 \text{ ms}$.

Figure 2.12 displays the results obtained for density, temperature, pressure and velocity. Despite being a quasi-conservative scheme, the double flux model [33], [35], [53] can solve strong shock waves in transcritical cases with a high degree of accuracy without generating spurious pressure oscillations.

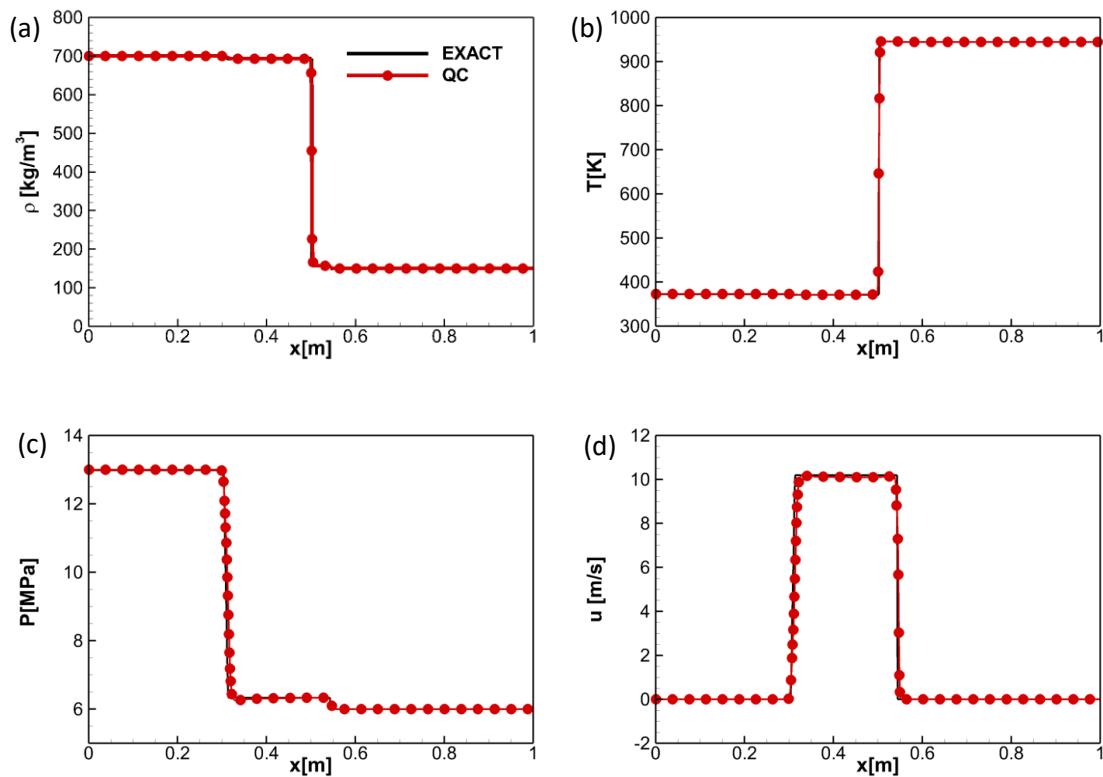


Figure 2.12: Shock Tube Problem 1 (Dodecane), QC formulation, CFL = 1.0, 800 cells, $t=0.2 \text{ ms}$. Comparisons of (a) density, (b) temperature, (c) velocity and (d) pressure profiles: exact solution and numerical solution.

Conservative formulation

The same shock tube problem described before is solved. A fifth-order WENO scheme is employed to interpolate the conservative variables onto the cell faces. Large spurious pressure oscillations appear in the solution because of the sharp jumps in the thermodynamic properties between cells, see Figure 2.13.

Comparison with the Peng-Robinson EoS (Quasi-conservative formulation)

Figure 2.14 shows the density, temperature, pressure, velocity, sound speed and internal energy of the same shock tube problem solved in a larger domain $x \in [0, 2]$ m using the PC-SAFT and the Peng-Robinson EoS. The simulated time is $t=0.3$ ms. The quasi-conservative formulation has been employed. 800 equally spaced cells were used. A significant difference can be observed in the results between the two EoS. Due to the high deviation in the sound speed computed by the Peng-Robinson EoS in the high-density region, the expansion wave travels much faster using the cubic model. Moreover, the calculated temperatures are much lower using the Peng-Robinson EoS in the high-density region.

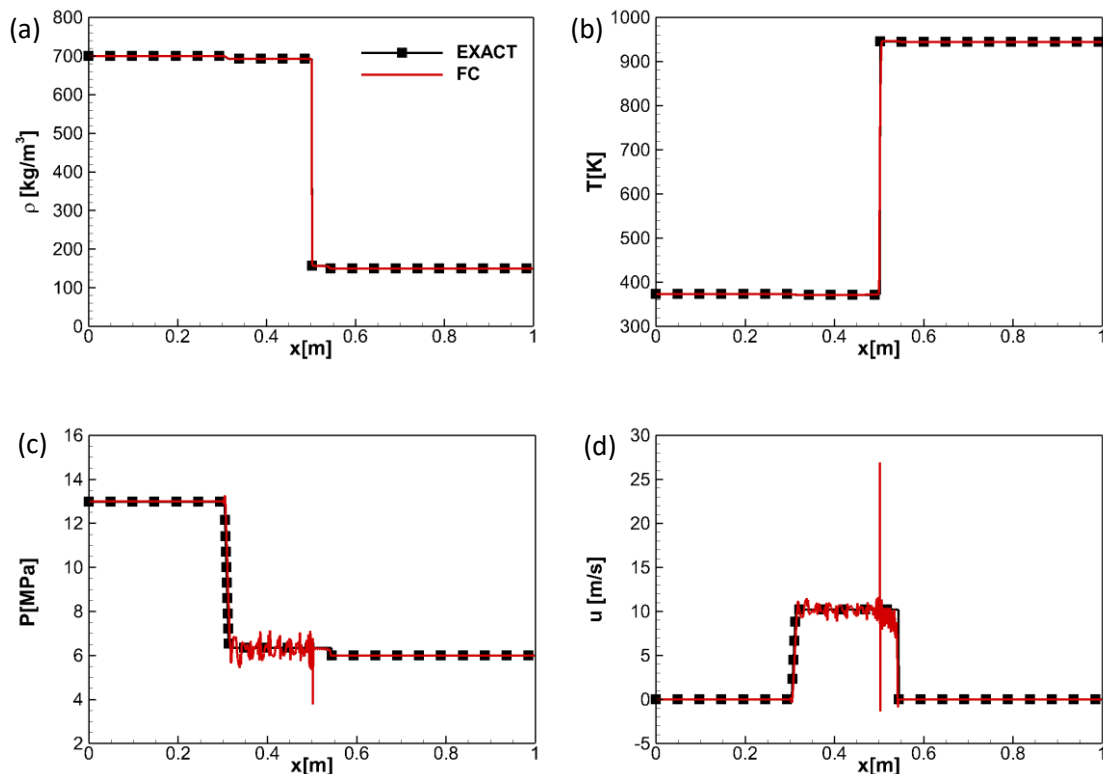


Figure 2.13: Shock Tube Problem 1 (Dodecane), FC formulation, CFL = 0.5, 4000 cells, $t=0.2$ ms. Comparisons of (a) density, (b) temperature, (c) velocity and (d) pressure profiles: exact solution and numerical solution.

2.2.2 Two-dimensional cases

Planar two-dimensional simulations of transcritical and supercritical jets are presented in this section. The initial conditions are summarized in Table 2.3. The parabolic sub-step is included into these simulations, without sub-grid scale modelling for turbulence or heat/species diffusion.

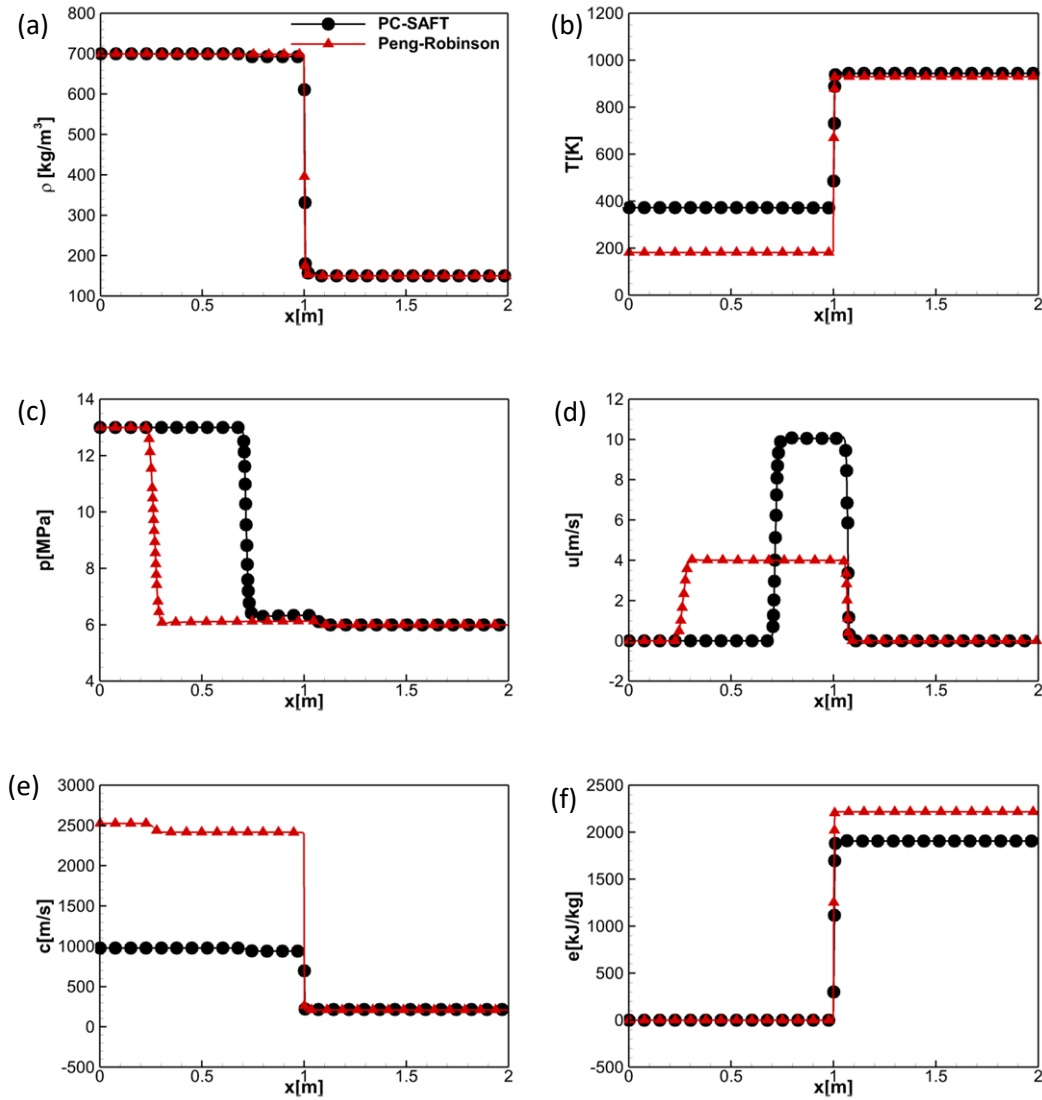


Figure 2.14: Shock Tube Problem 2 (Dodecane), QC formulation, CFL = 1.0, 800 cells, $t=0.3$ ms. Comparison of the (a) density, (b) temperature, (c) pressure, (d) x-velocity, (e) sound speed, (f) internal energy between the numerical solutions obtained using the Peng-Robinson EoS and the PC-SAFT EoS.

Transcritical nitrogen injection (Quasi-Conservative formulation, Case A)

A structured mesh is applied with a uniform cell distribution. The cell size is $0.043 \text{ mm} \times 0.043 \text{ mm}$. The domain used is $30 \text{ mm} \times 15 \text{ mm}$. Transmissive boundary conditions are applied at

the top, bottom and right boundaries while a wall condition is employed at the left boundary. A flat velocity profile is imposed at the inlet. The case is initialized using a pressure in the chamber of 4 MPa, the density of the nitrogen in the chamber is 45.5 kg/m^3 and the temperature is 299.5 K. The temperature of the jet is 84.4 K and the density is 804.0 kg/m^3 . The velocity of the jet is 100 m/s and the diameter of the exit nozzle is 1.0 mm.

When the jet enters the elevated temperature environment of the chamber, the velocity gradients at the jet surface generate a vortex rollup that finally breakup into ligament-shaped structures, see Figure 2.15. The Kelvin Helmholtz instability can be observed in the shear layer, which is similar to a gas/gas turbulent mixing case. No droplets are formed at these conditions. The jet is quickly heated to a gas-like supercritical state after the injection takes place. It must be highlighted that the mesh resolution is not enough to resolve all the scales (the aim of these simulations is to test the developed numerical framework). Moreover, 2D simulation cannot resolve turbulence. Figure 2.18 shows the density, temperature, pressure and sound speed results at $4 \times 10^{-4} \text{ s}$.

Figure 2.16 shows a scatter plot of pressure as a function of density for the planar cryogenic nitrogen jet. The simulated case remains in the hyperbolic region of the governing equations with a real-valued speed of sound. The mixing trajectory passes close to the critical point with a few individual points inside the saturation curve, which means that phase separation does not occur [31]. The larger fluctuations caused by the confined domain or the two-dimensionality of the case could be the reason why a small number of cells are in the unstable region [33].

Although one of reasons of the prevailing usage of cubic EoS is their efficiency, practical simulations can be performed using the PC-SAFT EoS. The quasi-conservative formulation is computationally less expensive than the conservative scheme because the PC-SAFT EoS has to be used only once in the hyperbolic operator in each time step. The computational time is 65-70% higher using the PC-SAFT EoS than utilizing the PR EoS. Figure 2.17 shows the time taken by the code to solve the transcritical nitrogen injection case depending on the number of cells used (only one core is used to perform the simulation). Figure 2.18 shows the density, temperature, pressure and sound speed results of the simulation at $t = 4 \times 10^{-4}$.

The PC-SAFT EoS is implemented using loops that depend on the number of components solved, which means that it takes more time to compute the properties of mixtures. However, knowing the mass fractions it is possible to determine how many components are present in a cell a priori. The PC-SAFT is then only solved for that specific number of components. Most cells

along the simulation in the combustion chamber contain only nitrogen. For this reason, a significant increment on time has not been observed performing two-component simulations.

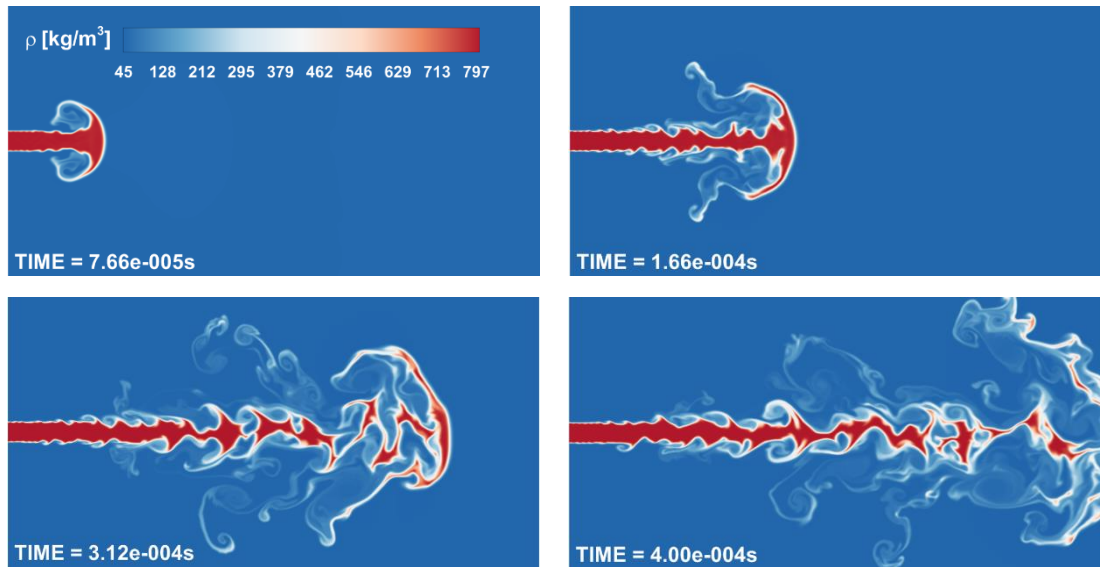


Figure 2.15: 2D Test Case A, CFL = 1.0, 245000 cells, QC formulation. Density results of the simulation of the planar cryogenic nitrogen jet at various times.

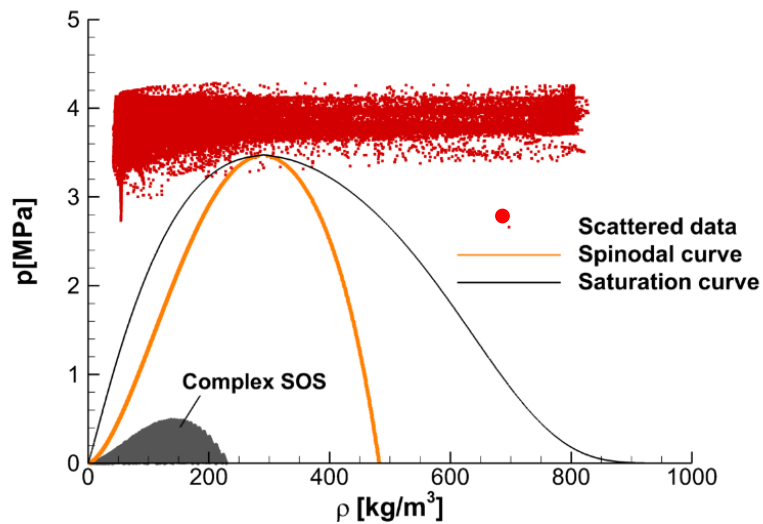


Figure 2.16: Scatter plot of pressure as a function of density for the transcritical nitrogen jet (Case A). The vapor dome, non-convex region and the region with complex speed of sound (SOS) are included.

Supercritical nitrogen injection (Conservative formulation, Case B)

The case is initialized using a pressure in the chamber of 4 MPa, the density of the nitrogen in the chamber is 45.5 kg/m³ and the density of the jet is 440.0 kg/m³ (Table 2.3). The velocity

of the jet is 50 m/s. The spatial reconstruction is carried out using a blending of the fifth-order WENO and the first-order schemes (95% fifth-order WENO).

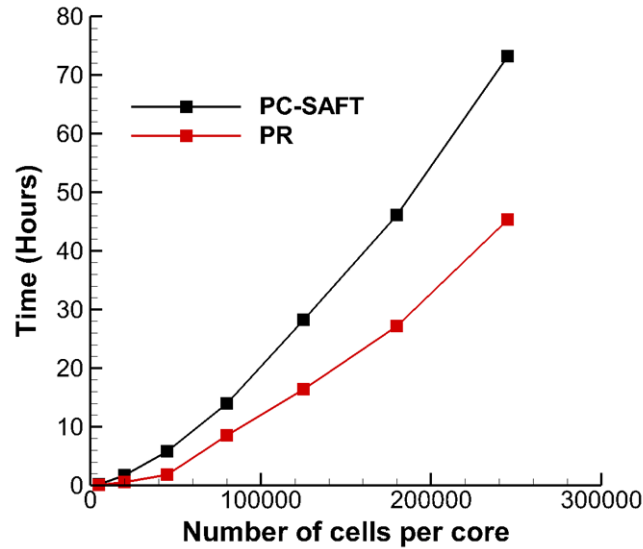


Figure 2.17: Computational time employed to compute the solution of the transcritical nitrogen jet (Case A) at $t = 4 \times 10^{-4}$ employing a variable number of cells.

The CFL number is set at 0.4. Transmissive boundary conditions are applied at the top, bottom and right boundaries while a wall condition is employed at the left boundary. A flat velocity profile is imposed at the inlet.

If sharp interface methods (i.e. front tracking method) are not applied, the interfaces are not sharp one-point jumps but smooth as they are resolved [82]. This is the reason why the wiggles that appear in this 2D simulation are not as severe as in the 1D cases, see Figure 2.19. The study of [82] shows how smooth interfaces can reduce the spurious pressure oscillations.

The minimum pressure encountered along the simulation is higher than the nitrogen critical pressure so there are no cells in the vapor-liquid equilibrium region. The heat-up of the jet follows the same density-temperature trajectory employing a FC or a QC formulation in single-species cases, see Figure 2.20. In the works of [21], [83] a different behaviour in multicomponent cases can be observed, where QC formulations follow an isobaric-isochoric mixing model for binary mixtures while conservative schemes follow an isobaric-adiabatic mixing model.

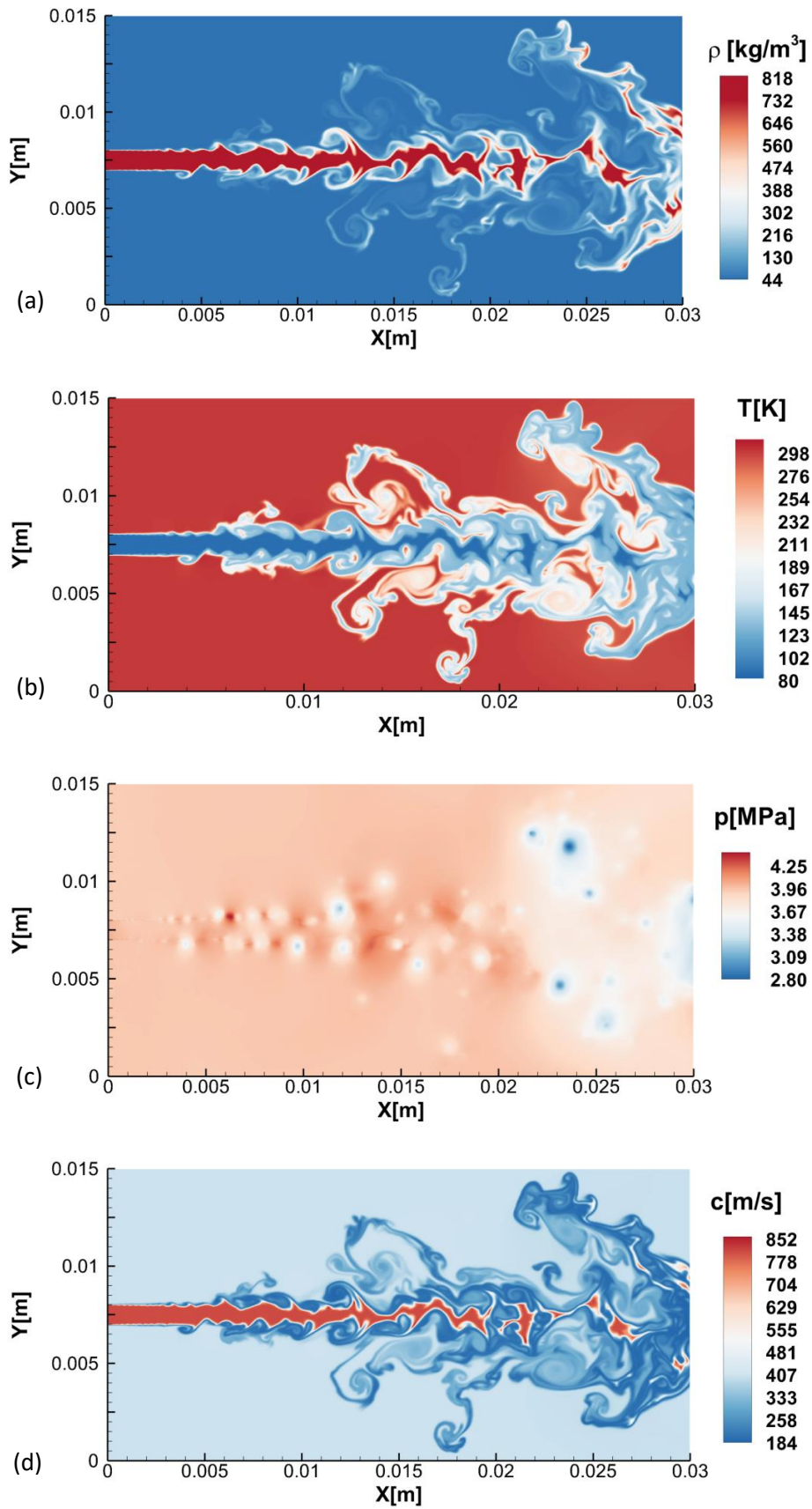


Figure 2.18: 2D Test Case A, CFL = 1.0, 245000 cells, QC formulation. Results of the simulation of the planar cryogenic nitrogen jet at $t = 4 \times 10^{-4}$ s using the quasi-conservative formulation: (a) density, (b) temperature, (c) pressure, (d) sound speed.

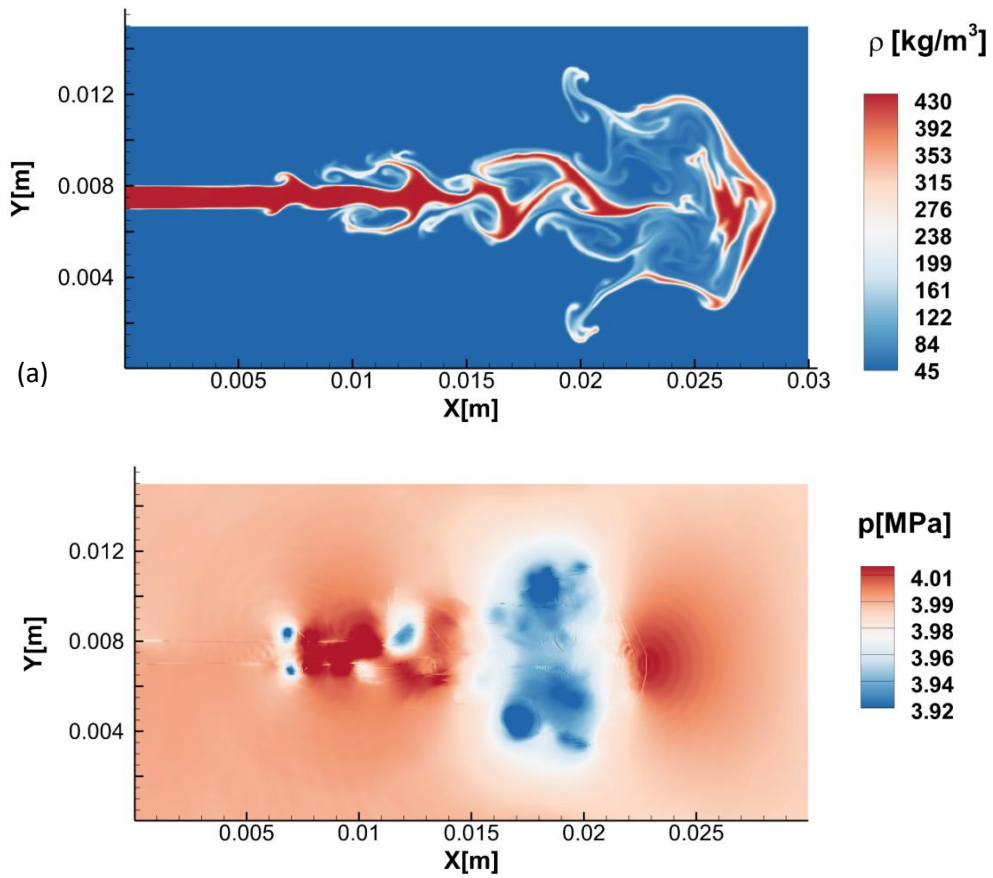


Figure 2.19: 2D Test Case B, CFL = 0.4, 180000 cells, FC formulation. Results of the simulation of the supercritical nitrogen jet at $t = 7.84 \times 10^{-4}$ s: (a) density, (b) pressure.

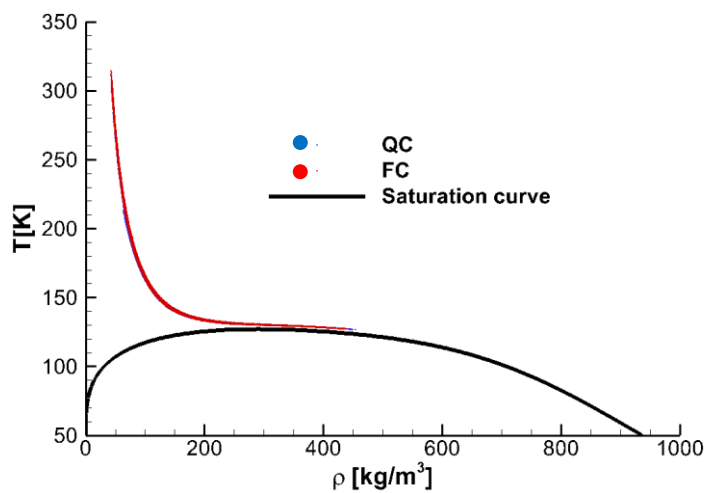


Figure 2.20: 2D Test Case B solved using the FC and QC formulations. Scattered data of density and temperature. The nitrogen vapor dome is included.

Supercritical n-dodecane injection (Conservative formulation, Case C)

Dodecane/nitrogen mixtures are Type IV as stated by [25], which means that the critical temperature of the mixture is an intermediate value of the critical temperature of both components and the mixture critical pressure is higher than the critical pressure of either component, see Figure 1.1. A simulation of a n-dodecane jet where VLE (Vapor-Liquid Equilibrium) conditions are avoided injecting the dodecane at a temperature higher than its critical value has been included to prove the multi-species capability of the code. To check that any cell is in a thermodynamic metastable state, the vapor-liquid saturation curves were computed (Section 2.2.4).

A structured mesh is applied with a uniform cell distribution. The cell size is $8.3\mu\text{m} \times 8.3\mu\text{m}$. The domain used is $5\text{mm} \times 2.5\text{mm}$. Transmissive boundary conditions are applied at the top, bottom and right boundaries while a wall condition is employed at the left boundary. A flat velocity profile is imposed at the inlet. The case is initialized using a pressure in the chamber of 11.1 MPa, the density and the temperature of the nitrogen in the chamber are 37.0 kg/m^3 and 973 K (high-load Diesel operation conditions [22]) respectively. The density and temperature of the jet are 450.0 kg/m^3 and 687 K (Table 2.3). The velocity of the jet is 200 m/s and the diameter of the exit nozzle is 0.1 mm.

As in the transcritical nitrogen case ligament-shaped structures appear and the Kelvin Helmholtz instability can be observed in the shear layer, see Figure 2.21. The jet is quickly heated-up from a liquid-like supercritical state to a gas-like supercritical state. Some spurious oscillations appear in the pressure field because of the high non-linearity of the EoS. The quasi-conservative formulation was not employed because of the incorrect prediction of the jet heat-up that appear in multi-component cases [21], [83].

A comparison of averaged scattered data of composition and temperature and an isobaric-adiabatic mixing process can be seen in Figure 2.22. As [83] stated, fully conservative schemes describe an isobaric-adiabatic mixing process. The isobaric-adiabatic line in the Figure 2.22 was computed using eq.30-31 and the initial conditions of this case.

$$\dot{m}_3 = \dot{m}_1 + \dot{m}_2 \quad (30)$$

$$\dot{m}_3 h_3 = \dot{m}_1 h_1 + \dot{m}_2 h_2 \quad (31)$$

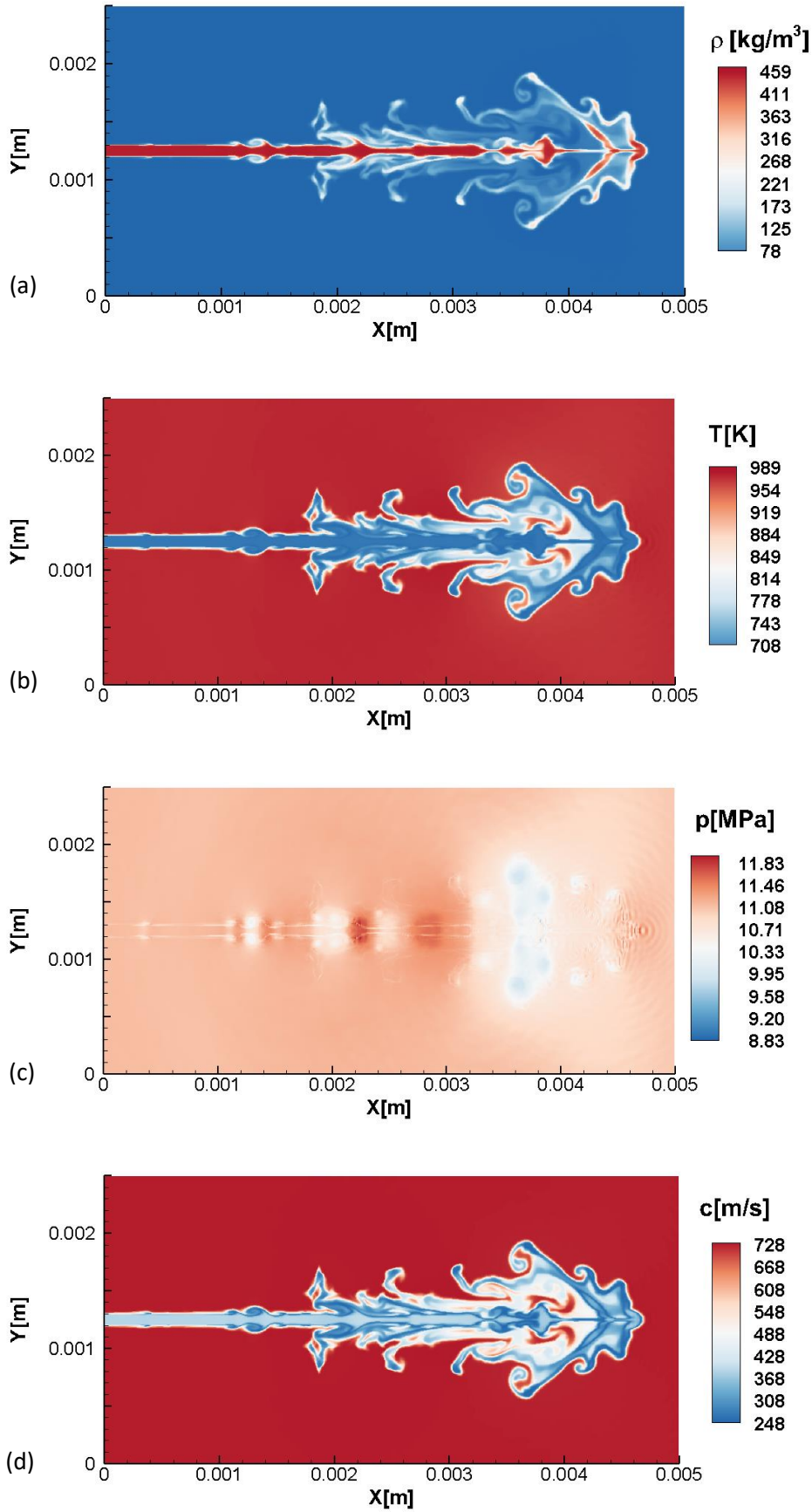


Figure 2.21: 2D Test Case C, CFL = 0.5, 180000 cells, FC formulation. Results of the simulation of the supercritical dodecane jet at $t = 2.5 \times 10^{-5}$ s: (a) density, (b) temperature, (c) pressure, (d) sound speed.

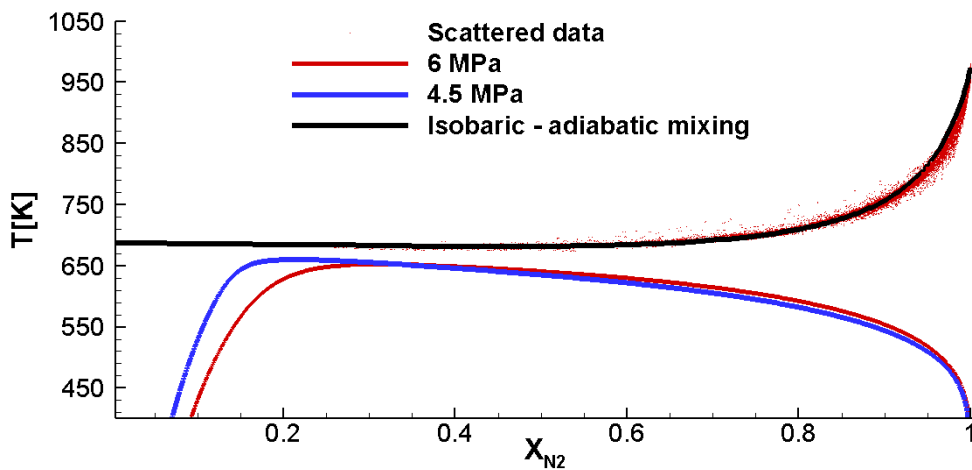


Figure 2.22: Scattered data of composition and temperature of the planar dodecane jet Case C. Solid lines are dodecane-nitrogen phase boundaries from VLE at 4.5 MPa and 6 MPa.

2.2.3 Hyperbolicity of Euler system with PC-SAFT EoS

The hyperbolicity of the Euler system relies on a real speed of sound [33]. Using the PC-SAFT, the speed of sound is always real outside of the vapor-liquid equilibrium state. Inside the vapor-liquid equilibrium region, the spinodal curves (determined by $(\partial p / \partial v)_T = 0$) enclose the unstable / non-convex region where a complex speed of sound could be found, see Figure 2.23.

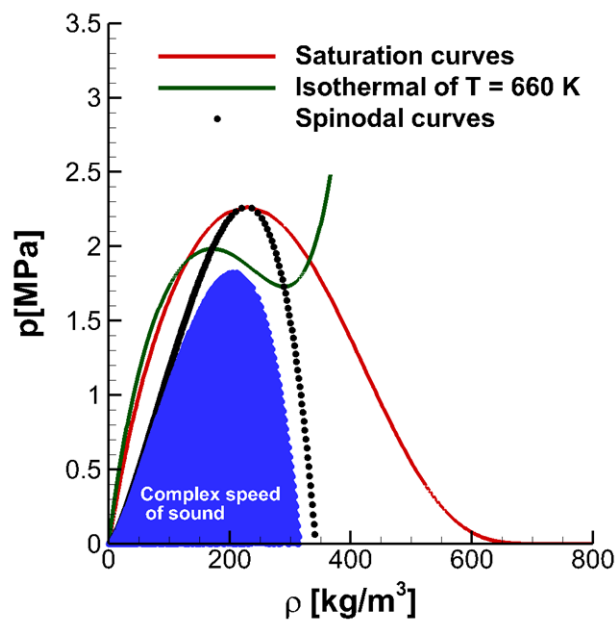


Figure 2.23: The vapor dome, non-convex region and the region with complex speed of sound of dodecane computed using the PC-SAFT EoS.

2.2.4 Pressure-composition phase diagram for the $N_2+C_{12}H_{26}$ system

The calculation of the number of phases present in a mixture in a certain condition is a recognized problem in the utilization of any EoS. In some cases, the number of phases is assumed a priori and then the composition in every phase is calculated by imposing equilibrium conditions. However, this technique often leads to divergence in the iterative methods used to achieve these. In our case, this is solved by an isothermal flash calculation after a stability analysis using the Tangent Plane Criterion Method proposed by [84] and applied to the PC-SAFT EoS by [85], see Figure 1.1.

2.2.5 Conclusions

The PC-SAFT was utilized to close the Navier-Stokes equations using both a conservative and a quasi-conservative formulation, where the double flux model of [33], [35], [53] is applied. The PC-SAFT EoS presents a precision similar to NIST without the need of an extensive calibration as only three parameters are needed to model a specific component. It is presented as an alternative to the commonly used cubic EoS that present a low accuracy for computing the thermodynamic properties of hydrocarbons at temperatures typical for high pressure injection systems. Advection test cases and shock tube problems have been used to validate the hyperbolic operator of the developed numerical framework. The conservative formulation generates spurious pressure oscillations, like it has been reported with other diffuse interface density-based codes employing a real-fluid EoS. Due to fact that the interfaces are not sharp one-point jumps but smooth, as they are resolved in 2D simulations, the wiggles generated do not compromise the stability of the simulation. The quasi-conservative scheme can model transcritical single- and multicomponent cases without spurious pressure oscillations. Errors in the energy conservation that appear employing this formulation may produce an unphysical quick heat-up of the injected jet in multicomponent cases. Two-dimensional simulations of nitrogen and n-dodecane jets have been presented to demonstrate the multidimensional and multicomponent capability of the numerical framework.

3. Simulation of supercritical Diesel jets using the PC-SAFT EoS

In this chapter, supercritical Diesel injections are performed employing a FC formulation of the Navier-Stokes equations along with the conservation of the energy equation [32]. Multi-component fuel-air mixing is simulated by considering a diffused interface approximation. The thermodynamic properties are predicted using the PC-SAFT EoS. PC-SAFT can handle flexibly the thermodynamic properties of multi-component mixtures, which is an advantage compared to the NIST library, where only limited component combinations are supported. This has allowed for the properties of Diesel fuel to be modelled as surrogates comprising four, five, eight and nine components. The numerical approach proposed in this chapter improves the overall computational time and overcomes the previously observed spurious pressure oscillations associated with the utilization of conservative schemes. In the absence of experimental data, advection test cases and shock tube problems are included to validate the developed framework. Finally, two-dimensional simulations of planar jets of n-dodecane and a four component Diesel surrogate are included to demonstrate the capability of the developed methodology to predict supercritical Diesel fuel mixing into air.

3.1 Numerical method

The way the PC-SAFT EoS has been coupled with the Navier-Stokes equations is described in Chapter 2 for FC formulations (Appendix: Algorithm A). Phase separations or metastable thermodynamic states are beyond the scope of this chapter and are not considered. The HLLC solver is applied to solve the Riemann problem. In density-based codes, once the spatial reconstruction scheme has been used to compute the left and right states of the Riemann problem, the EoS is applied to compute the pressure and sonic fluid velocity at both sides (considering that the conservative variables have been reconstructed). Eq.32 shows the pressure expressed in a form equivalent to a general EoS [34]:

$$p(\rho, e, Y_i) = F(\rho, Y_i)\rho e + G(\rho, Y_i) \quad (32)$$

However, the computed pressure may present a large error if the functions F or G depend on the interpolated conservative variables. Even in single-species cases, if these functions are density-dependent and consist of high-order density terms, a small change in the interpolated density can produce large variations in the calculated pressure. The incorrect pressure

introduces an error in the computation of the fluxes, which finally generate spurious oscillations during the numerical solution. In the present study, this is avoided by reconstructing the primitive variables (or only the pressure) and the conservative variables at the cell faces at the same time. This simple modification has been found to smooth-out the spurious pressure oscillations generated by the high-nonlinearity of the EoS.

By reconstructing the pressure, the only variable left to compute the fluxes at the cell faces is the speed of sound. Instead of using the EoS to calculate this variable, the sonic fluid velocity is interpolated using cell centre values as well. Therefore, the PC-SAFT EoS is used only once per cell in each RK sub-time step, thus reducing significantly the computational time.

3.1.1 Spatial reconstruction methods and Riemann solver

Second-order spatial reconstruction and Riemann solver

A variation of the MUSCL-Hancock scheme [74] is applied. The fluxes are computed in the following way:

Step 1: Data reconstruction.

Once the conservative variables are updated after each Runge-Kutta sub-time step, the primitive variables and the sonic fluid velocity are computed and stored at the cell centres. The one-dimensional vector of primitive variables (considering a single-species case) stored in each cell centre is:

$$\mathbf{W}_i = (\rho, u, p)$$

Data cell averages of the primitive variables are replaced by piece-wise linear functions in each cell:

$$\mathbf{W}_i(x) = \mathbf{W}_i^n + \frac{(x-x_i)}{\Delta x} \Delta_i^P, x \in [0, \Delta x] \quad I_i = [x_{1-1/2}, x_{1+1/2}] \quad (33)$$

where Δ_i^P is the slope vector of the primitive variables; the Minmod slope limiter is employed again.

The boundary extrapolated values of the primitive variables in global coordinates are computed as:

$$\mathbf{W}_i^L(x) = \mathbf{W}_i^n + \frac{1}{2} \Delta_i^P \quad (34)$$

$$\mathbf{W}_i^R(x) = \mathbf{W}_i^n - \frac{1}{2} \Delta_i^P$$

The boundary extrapolated values of the sonic fluid velocity are computed as well:

$$\begin{aligned}
c_i^L(x) &= c_i^n + \frac{1}{2}\Delta_i^s \\
c_i^R(x) &= c_i^n - \frac{1}{2}\Delta_i^s
\end{aligned} \tag{35}$$

where Δ_i^s is the slope scalar of the speed of sound. The Minmod slope limiter is applied as well.

Step 2: Evolution.

The boundary extrapolated values of the primitive variables are evolved by a time $1/2\Delta t$ using eq.36 [74]:

$$\overline{W}_i^{L,R} = W_i^{L,R} + \frac{1}{2} \frac{\Delta t}{\Delta x} \mathbf{A}(W_i^n) [W_i^L - W_i^R] \tag{36}$$

where A is computed using the data cell average W_i^n .

$$\mathbf{A} = \begin{pmatrix} u & \rho & 0 \\ 0 & u & \frac{1}{\rho} \\ 0 & \rho a^2 & u \end{pmatrix}$$

The boundary extrapolated values of the conservative variables are evolved by a time $1/2\Delta t$ using eq.37:

$$\begin{aligned}
\overline{U}_i^L &= U_i^L + \frac{1}{2} \frac{\Delta t}{\Delta x} [\mathbf{F}(U_i^L) - \mathbf{F}(U_i^R)] \\
\overline{U}_i^R &= U_i^R + \frac{1}{2} \frac{\Delta t}{\Delta x} [\mathbf{F}(U_i^L) - \mathbf{F}(U_i^R)]
\end{aligned} \tag{37}$$

The fluxes $\mathbf{F}(U_i^{L,R})$ are computed as:

$$F = \begin{pmatrix} \rho u \\ \rho u^2 + p \\ (\rho E + p)u \end{pmatrix}$$

were ρ, u and E are obtained from the evolved conservative variables (\overline{U}_i) and p is obtained from the evolved primitive variables (\overline{W}_i).

Step 3: The Riemann Problem.

The Riemann problem is solved to compute the intercell flux using the evolved conservative variables, the evolved primitive variables and the interpolated speed of sound.

$$U_L \equiv \bar{U}_i^R ; U_R \equiv \bar{U}_{i+1}^L$$

$$W_L \equiv \bar{W}_i^R ; W_R \equiv \bar{W}_{i+1}^L$$

$$c_L, c_R$$

Within the variables needed to solve the Riemann problem, ρ, u, E are obtained from the reconstructed conservative variables, p is obtained from the evolved primitive variables and c is the interpolated speed of sound. There is no need of using the EoS at the cell faces as the speed of sound and the pressure are already known from the previous operation. The HLLC solver is employed to solve the Riemann problem.

Fifth-order WENO spatial reconstruction and Riemann solver

The conservative variables, primitive variables and speed of sound are reconstructed at the cell faces using a fifth-order WENO scheme [75].

Figure 3.1 presents a visual representation of how the convective fluxes have been computed.

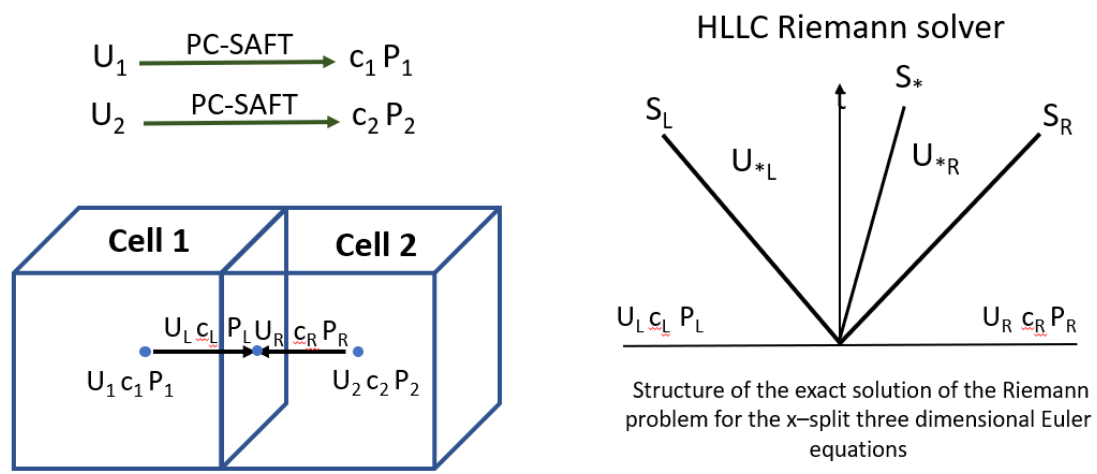


Figure 3.1: Schematic representation of hyperbolic sub-step

Temporal integration

In many cells the sum of the fluxes is practically 0. Applying a SSP-RK3 scheme, this means that in these cells:

$$U_i^{(1)} = U_i^n, U_i^{(2)} = U_i^{(1)} \text{ or } U_i^{(n+1)} = U_i^{(2)}$$

which can be translated into:

$$W_i^{(1)} = W_i^n, W_i^{(2)} = W_i^{(1)} \text{ or } W_i^{(n+1)} = W_i^{(2)}$$

and

$$c_i^{(1)} = c_i^n, c_i^{(2)} = c_i^{(1)} \text{ or } c_i^{(2)} = c_i^{(1)}.$$

Therefore, there is no need to employ the EoS in all these cases to update the pressure, speed of sound, temperature and enthalpy, which are all stored at the cell centres.

3.1.2 Diesel surrogates

Table 3.1 shows a comparison between the experimentally measured surrogate densities computed at 293.15K and 0.1MPa with the densities calculated employing the EoS-based method developed at NIST [80] and the PC-SAFT EoS. The composition of the Diesel surrogates was proposed by [70]. They are divided into two accuracy types depending on how closely they match the composition of real Diesel. More specifically, V0a and V0b are two low-accuracy surrogates and V1 and V2 are the two high-accuracy surrogates. Their molar composition is summarized in Table 3.2. The results obtained by the PC-SAFT EoS shows the highest degree of agreement with the experimental values [71] in comparison with the results obtained by [70] applying the method developed at NIST, see Table 3.1. Table 3.3 presents the PC-SAFT pure component parameters employed.

Table 3.1: Comparison between experimentally measured surrogate densities (kg/m³) at 293.15 K and 0.1MPa with the NIST and PC-SAFT predictions [71].

| Surrogate | Experiment | NIST | PC-SAFT |
|-----------|------------|-------|---------|
| V0a | 818 | 809.1 | 814.9 |
| V0b | 837.5 | 821.6 | 833.2 |
| V1 | 828.4 | 814.1 | 825.2 |
| V2 | 853 | 839.9 | 861.8 |

Table 3.2: Molar composition for the four Diesel fuel surrogates (V0a, V0b, V1, V2) [70]

| Compound | V0a | V0b | V1 | V2 |
|---------------------------|------|------|------|------|
| n-hexadecane | 27.8 | - | 2.70 | - |
| n-octadecane | - | 23.5 | 20.2 | 10.8 |
| n-eicosane | - | - | - | 0.80 |
| heptamethylnonane | 36.3 | 27.0 | 29.2 | - |
| 2-methylheptadecane | - | - | - | 7.3 |
| n-butylcyclohexane | - | - | 5.10 | 19.1 |
| triisopropylcyclohexane | - | - | - | 11.0 |
| trans-decalin | 14.8 | - | 5.50 | - |
| perhydrophenanthrene | - | - | - | 6.00 |
| 1,2,4-trimethylbenzene | - | 12.5 | 7.5 | - |
| 1,3,5-triisopropylbenzene | - | - | - | 14.7 |
| tetralin | - | 20.9 | 15.4 | 16.4 |
| 1-methylnaphthalene | 21.1 | 16.1 | 14.4 | 13.9 |

Table 3.3: PC-SAFT pure component parameters [71], [86]

| Compound | m | σ (Å) | ϵ/k (K) |
|-------------------------------|-------|--------------|------------------|
| n-hexadecane | 6.669 | 3.944 | 253.59 |
| n-octadecane | 7.438 | 3.948 | 254.90 |
| n-eicosane | 8.207 | 3.952 | 255.96 |
| heptamethylnonane | 5.603 | 4.164 | 266.46 |
| 2-methylheptadecane | 7.374 | 3.959 | 254.83 |
| n-butylcyclohexane | 3.682 | 4.036 | 282.41 |
| 1,3,5-triisopropylcyclohexane | 4.959 | 4.177 | 297.48 |
| trans-decalin | 3.291 | 4.067 | 307.98 |
| perhydrophenanthrene | 4.211 | 3.851 | 337.52 |
| 1,2,4-trimethylbenzene | 3.610 | 3.749 | 284.25 |
| 1,3,5-triisopropylbenzene | 5.178 | 4.029 | 296.68 |
| tetralin | 3.088 | 3.996 | 337.46 |
| 1-methylnaphthalene | 3.422 | 3.901 | 337.14 |

3.1.3 Phase diagrams

The number of phases is solved by an isothermal flash calculation after a stability analysis using the Tangent Plane Criterion Method proposed by [84] and applied to the PC-SAFT EoS by [85] using the code developed by [71] like in Chapter 2. This methodology has not been implemented in the CFD code. It is used to obtain the phase diagrams employed to check that the VLE state is not present in the solution of the performed simulations.

3.2 Results

Firstly, a comparison of the temperature, sonic fluid velocity and internal energy of n-dodecane, V0a, V0b, V1 and V2 Diesel surrogates is presented to point out the importance of an accurate fuel properties modelling. Then, several advection test cases and shock tube problems are solved to validate the hyperbolic part of the numerical framework and show how the reconstruction technique explained in Section 3.1 smooths-out the spurious pressure oscillations. Finally, two-dimensional simulations at high-load Diesel operation conditions of supercritical n-dodecane and Diesel surrogate V0a are presented to demonstrate the multicomponent and multidimensional capability of the developed numerical solver.

3.2.1 N-dodecane and Diesel comparison

Figure 3.2 shows a comparison of the thermodynamic properties of n-dodecane and the Diesel surrogates V0a, V0b, V1 and V2 at 6MPa, as calculated using the PC-SAFT EoS. The main differences between n-dodecane and the Diesels can be found in the temperature and sonic

fluid velocity at high densities. The temperature is an important thermodynamic property in transcritical simulations because it determines the transition to a supercritical state. The sonic fluid velocity plays a key role in the computation of the hyperbolic fluxes and in the time step calculation. The effects that these variables have in the CFD results can be seen in Figure 3.12.

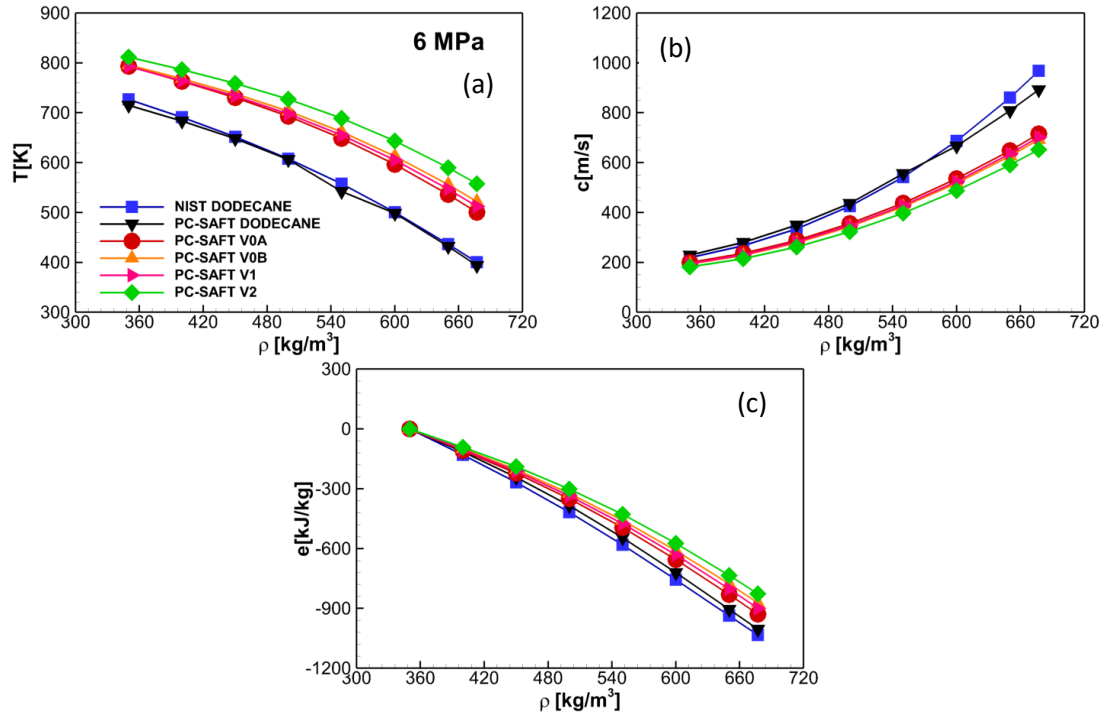


Figure 3.2: Comparison of thermodynamic properties of n-dodecane and Diesel surrogates at 6MPa: (a) density, (b) sonic fluid velocity, (c) internal energy

3.2.2 Advection test cases

Single-species advection test case

Table 3.4 summarises the advection test cases simulated. Figure 3.3 shows the results of the Advection Test Case 1, where nitrogen is used. The initial conditions are the same as the ones used by [42] in the interface advection problem. The computational domain is $x \in [0, 1]$ m. In $0.0 < x < 0.3$ m, the initial conditions are $\rho=450\text{kg/m}^3$, $p=4\text{MPa}$, and $u=10.0\text{m/s}$; in the rest of the domain they are $\rho=45.0\text{kg/m}^3$, $p=4\text{MPa}$, and $u=10.0\text{m/s}$. A uniform grid spacing of 0.01m is employed; the simulated time is $t=0.04\text{s}$; the CFL is set to be 0.5. Wave transmissive boundary conditions are implemented in the left and right sides of the computational domain. The spatial reconstruction has been performed in two different ways. In the first one, the PC-SAFT EoS is used to compute the sonic fluid velocity and the pressure using the reconstructed conservative

variables. In the second one, the pressure and sonic fluid velocity are interpolated onto the cell faces, as described in Section 3.1.

Large wiggles appear in the velocity and pressure fields at 0.04s using the classic spatial reconstruction method, as can be seen in Figure 3.3. The start-up error is present for a long period of time in the simulation and contaminates the solution. This can be observed in the Figure 3.4-3.5, both reveal the maximum wiggles amplitude (calculated as the maximum difference between the analytical solution and the computed profile [42]) along time in the pressure and velocity fields. More specifically, Figure 3.4 presents the results obtained using the second-order MUSCL-Hancock scheme, while Figure 3.5 shows the results calculated utilizing the fifth-order WENO scheme. By applying the schemes proposed in Section 3.1, once the oscillations generated by the start-up error have travelled upstream and downstream with their characteristic speeds and reach the boundaries of the computational domain, the solution shows no wiggles. A smooth initial interface can be used for avoiding the initial start-up error [82]. By employing a diffuse interface method, the interfaces are not sharp one-point jumps but smooth as they are resolved. Then, a smooth initial profile is a realistic initial condition. To initialize the simulation using a smooth interface the primitive variables are calculated employing eq.27.

Employing this formula, the number of grid points used in the initial interface does not depend on the grid resolution. The interface will be sharpened in space if the number of cells utilized is increased but the number of points across of the interface does not change. Figure 3.4-3.5 shows that for the spatial reconstruction methods proposed the start-up error is not present in the obtained solution for values of C_ε bigger than 2.

Table 3.4: ADVECTION TEST CASES

| ADVECTION TEST CASES | | | |
|-----------------------------|-----------------------|------------------------------|------------------------|
| CASE 1 | Pressure [MPa] | Density [kg/m ³] | Temperature [K] |
| 0.25 m < x | N ₂ , 4.0 | N ₂ , 450.0 | N ₂ , 126.6 |
| 0.25 m > x | N ₂ , 4.0 | N ₂ , 45.0 | N ₂ , 302.0 |
| CASE 2 | | | |
| 0.25 m < x | Diesel V0a, 11.1 | Diesel V0a, 450.0 | Diesel V0a, 782.2 |
| 0.25 m > x | N ₂ , 11.1 | N ₂ , 37.0 | N ₂ , 972.9 |

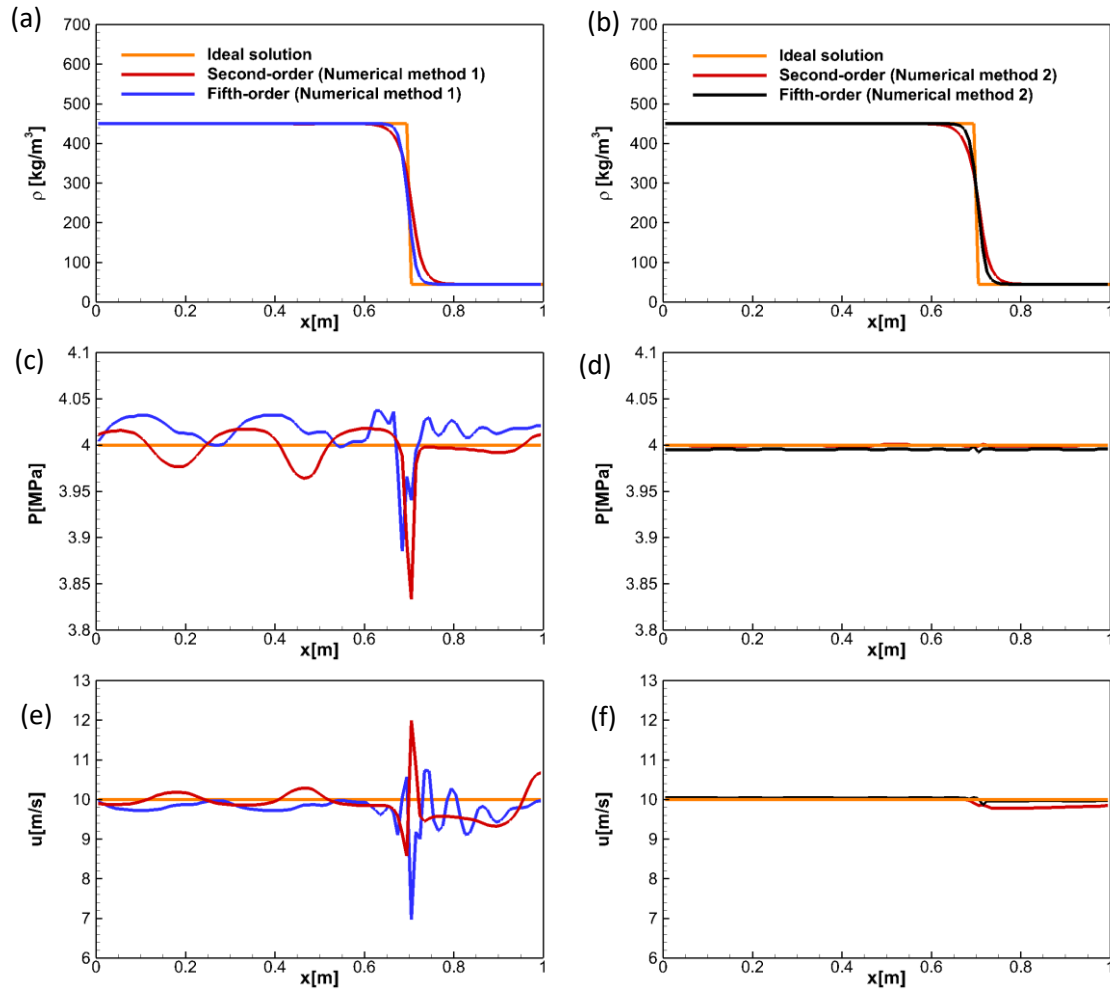


Figure 3.3: Advection Test Case 1 (N_2), CFL = 0.5, $u = 10$ m/s, 100 cells, $t=0.04$ s. Comparison of the (a-b) density, (c-d) pressure and (e-f) x-velocity between the analytical and the numerical solutions. Numerical solution 1: Pressure and sonic fluid velocity computed at the faces using the EoS. Numerical solution 2: Pressure and sonic fluid velocity interpolated at the faces.

Multi-component advection test case

Figure 3.7 shows the results of the advection of the Diesel surrogate V0a in nitrogen (Table 3.4). The computational domain is $x \in [0, 1]$ m; the initial conditions in $0.25\text{m} < x < 0.75\text{m}$ are $\rho_{V0A} = 450.0$ kg/m³, $p_{V0A} = 11.1$ MPa, and $T_{V0A} = 782.2$ K; in the rest of the domain $\rho_{N_2} = 37.0$ kg/m³, $p_{N_2} = 11.1$ MPa, and $T_{N_2} = 972.9$ K. The advection velocity utilized is 10 m/s; periodic boundary conditions are used; 500 cells are employed; the simulated time is $t=0.1$ s; the fifth-order WENO discretization scheme presented is used; and the CFL is set to be 0.5. A smooth interface is applied ($C_\epsilon = 2$). The oscillations in the velocity and pressure field are lower than 1.0% and 0.3% respectively of the initial values. The VLE state is not present in the solution, as can be seen in Figure 3.6 where the maximum temperature encountered by the Diesel surrogate V0a - nitrogen phase boundary at 7 MPa is 705K (this value is lower at higher pressures). The minimum temperature reached in the simulation is 782k.

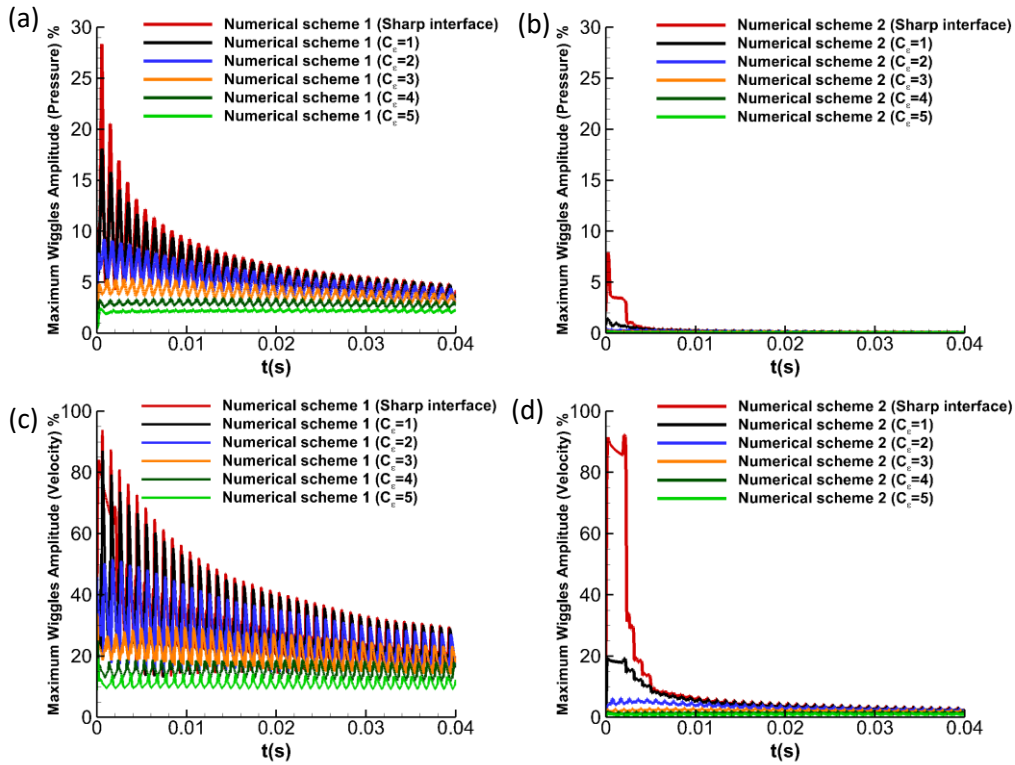


Figure 3.4: Advection Test Case 1 (N_2), CFL = 0.5, $u = 10$ m/s, 100 cells. Maximum wiggles amplitude in the velocity and pressure fields. Analysis of smooth and sharp initial interfaces using the second-order MUSCL-Hancock scheme. Numerical solution 1: Pressure and sonic fluid velocity computed at the faces using the EoS. Numerical solution 2: Pressure and sonic fluid velocity interpolated at the faces.

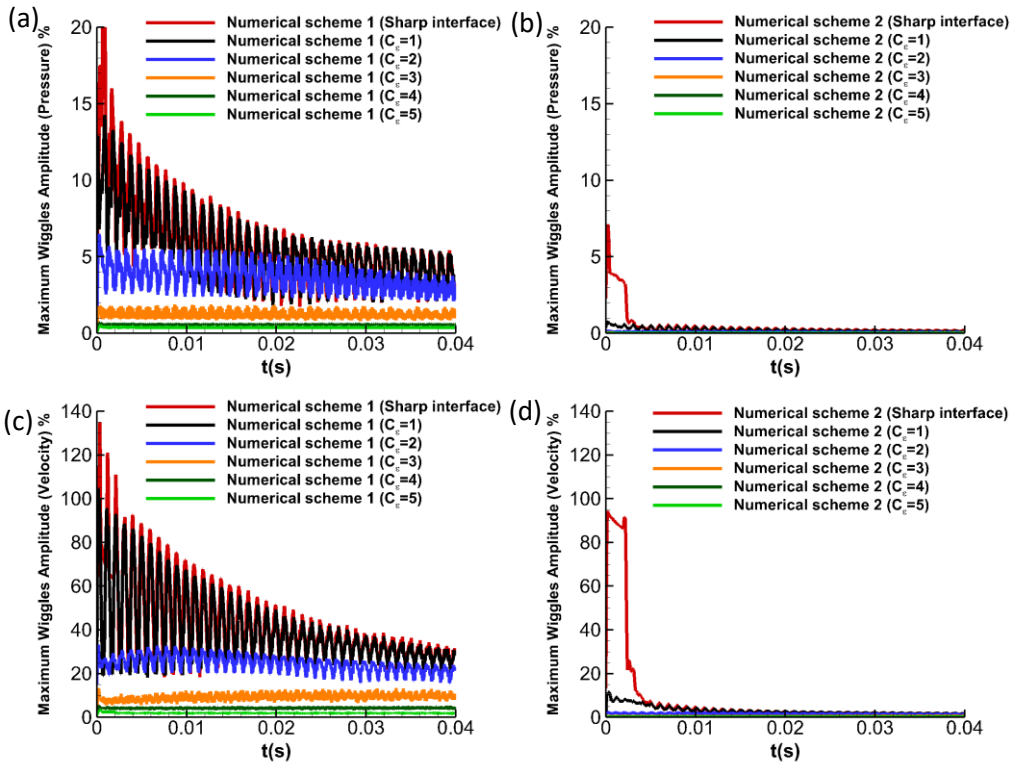


Figure 3.5: Advection Test Case 1 (N_2), CFL = 0.5, $u = 10$ m/s, 100 cells. Maximum wiggles amplitude in the velocity and pressure fields. Analysis of smooth and sharp initial interfaces using the fifth-order WENO scheme. Numerical solution 1: Pressure and sonic fluid velocity computed at the faces using the EoS. Numerical solution 2: Pressure and sonic fluid velocity interpolated at the faces.

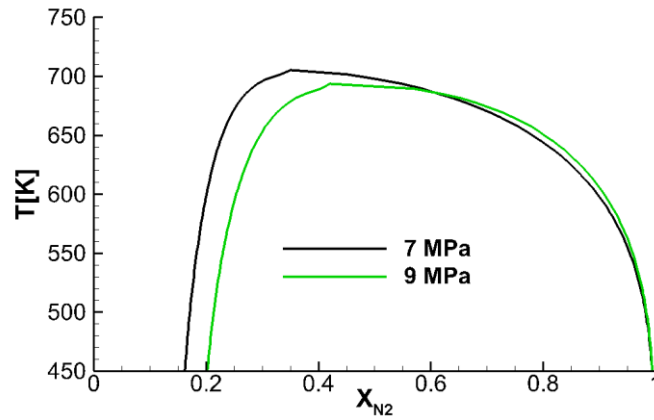


Figure 3.6: Diesel surrogate V0a - nitrogen phase boundary from VLE at different pressures.

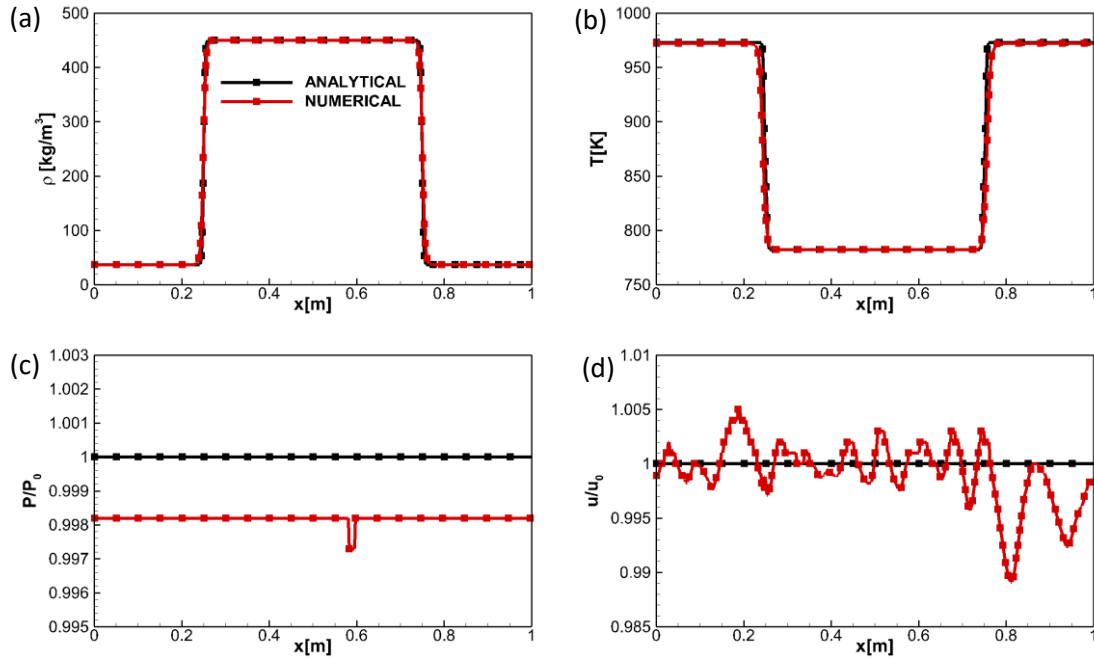


Figure 3.7: Advection Test Case 2 (Diesel surrogate V0a – N2), CFL=0.5 $u = 10$ m/s, 500 cells, $t=0.1$ s. Comparison of the (a) density, (b) temperature, (c) pressure and (d) x-velocity between the analytical and the numerical solution.

3.2.3 Shock tube problems

The Euler equations are solved in this exercise, so direct comparison with the exact solver can be performed to validate the hyperbolic part of the developed numerical framework. The exact solution has been computed using the methodology described in [81].

Shock Tube Problem 1, 2, 3

Figure 3.8-3.11 displays the results of three shock tube problems which employ n-dodecane as working fluid. The domain is $x \in [-0.5, 0.5]$ m; 1000 equally spaced cells were used. Wave transmissive boundary conditions are implemented in the left and right sides. The initial conditions are summarized in Table 3.5. The simulated time is $5 \cdot 10^{-4}$ s in the Shock Tube Problem 1 and 2, and $2.5 \cdot 10^{-4}$ s in the Shock Tube Problem 3. The CFL is set to 0.3 to stabilize the cases with large spurious pressure oscillations. The reconstruction step has been performed in two different ways. In the first one, the PC-SAFT EoS is used to compute the sonic fluid velocity and the pressure using the reconstructed conservative variables. In the second one, the pressure and sonic fluid velocity are interpolated onto the cell faces.

In the Shock Tube Problem 1 (Figure 3.8-3.9), the variation of the thermodynamic properties between the right and left states is not large enough to generate spurious pressure oscillations. However, spurious pressure oscillations appear in the Shock Tube Problem 2 (Figure 3.10) because of the sharper jump in the thermodynamic conditions. Employing the modified reconstruction, the spurious oscillations are significantly reduced. In the Shock Tube Problem 3 (Figure 3.11) the larger variation in the thermodynamic properties between the left and right states provoke the formation of large spurious pressure oscillations. Using the modified reconstruction, the oscillations can be significantly reduced (specially is the MUSCL- Hancock scheme is employed) like in the Shock Tube Problem 2.

Table 3.5: SHOCK TUBE PROBLEMS

| CASE 1 | Pressure [MPa] | Density [kg/m ³] | Velocity [m/s] |
|---------------|----------------|------------------------------|----------------|
| $x < 0.5$ m | 30.0 | 438.0 | 0.0 |
| $x > 0.5$ m | 10.0 | 100.0 | 0.0 |
| CASE 2 | | | |
| $x < 0.5$ m | 30.0 | 620.0 | 0.0 |
| $x > 0.5$ m | 10.0 | 100.0 | 0.0 |
| CASE 3 | | | |
| $x < 0.5$ m | 30.0 | 710.0 | 0.0 |
| $x > 0.5$ m | 10.0 | 100.0 | 0.0 |
| CASE 4 | | | |
| $x < 0.5$ m | 30.0 | 620.0 | 0.0 |
| $x > 0.5$ m | 10.0 | 100.0 | 0.0 |

Shock Tube Problem 4

Figure 3.12 displays the density, temperature, pressure, velocity, sonic fluid velocity and internal energy results of a transcritical shock tube problem, which employs n-dodecane and the V0a, V0b, V1 and V2 Diesel surrogates as working fluids. The domain is $x \in [0, 1]$ m. 800 equally

spaced cells were used. Wave transmissive boundary conditions are implemented in the left and right sides. The initial conditions in the left state are $\rho_L=620\text{kg/m}^3$, $p_L=30\text{MPa}$, $u_L=0\text{m/s}$; and in the right state are $\rho_R=100\text{kg/m}^3$, $p_R=10\text{MPa}$, $u_R=0\text{m/s}$. The fifth-order WENO discretization scheme presented in Section 2.a. is used. The CFL is set to 0.8. The simulated time is $5 \cdot 10^{-4}\text{s}$.

The obtained results suggest that there is a significant difference between n-dodecane and the Diesel surrogates. The temperatures computed using Diesel surrogates are higher than those obtained for n-dodecane throughout the whole computational domain. The different sonic fluid velocities in the high-density region forces the expansion wave to move with different velocities. The larger variations in the Diesel internal energy may be related to the different velocity profiles computed. There is not a significant difference in the results obtained using the different Diesels.

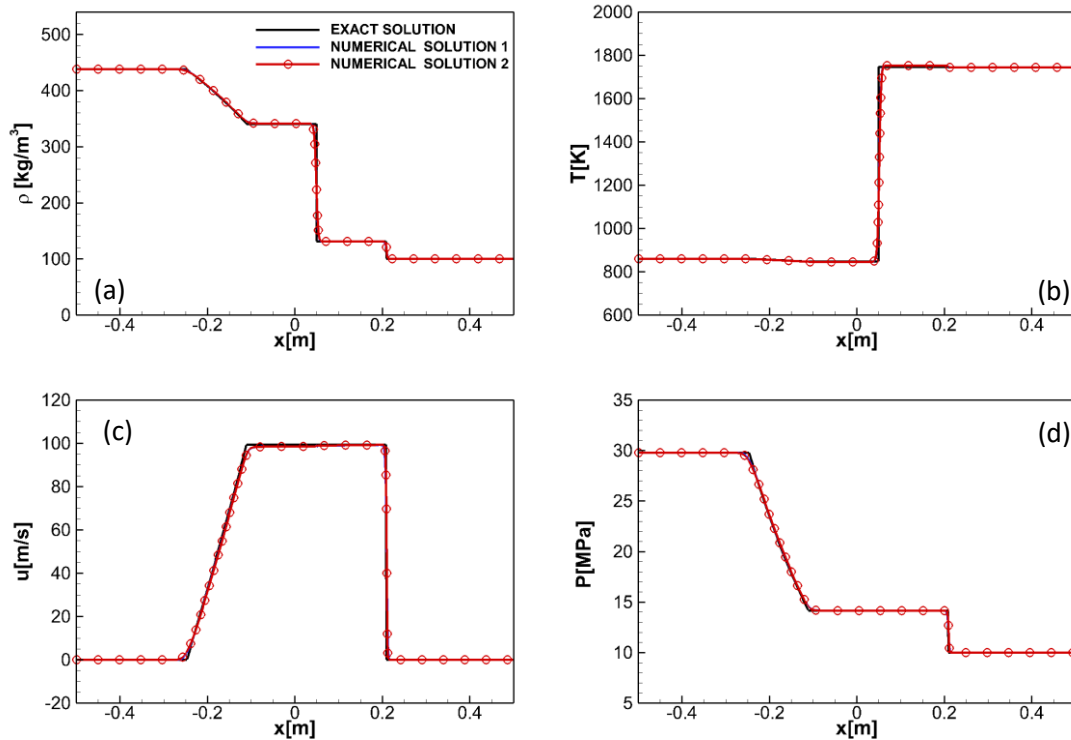


Figure 3.8: Shock Tube Problem 1 (MUSCL-Hancock scheme, Dodecane). CFL = 0.5, $u = 10$ m/s, 1000 cells, $t=5 \cdot 10^{-4}$ s. Comparisons of (a) density, (b) temperature, (c) velocity and (d) pressure profiles: exact solution and numerical solutions. Numerical solution 1: Pressure and sonic fluid velocity computed at the faces using the EoS. Numerical solution 2: Pressure and sonic fluid velocity interpolated at the faces.

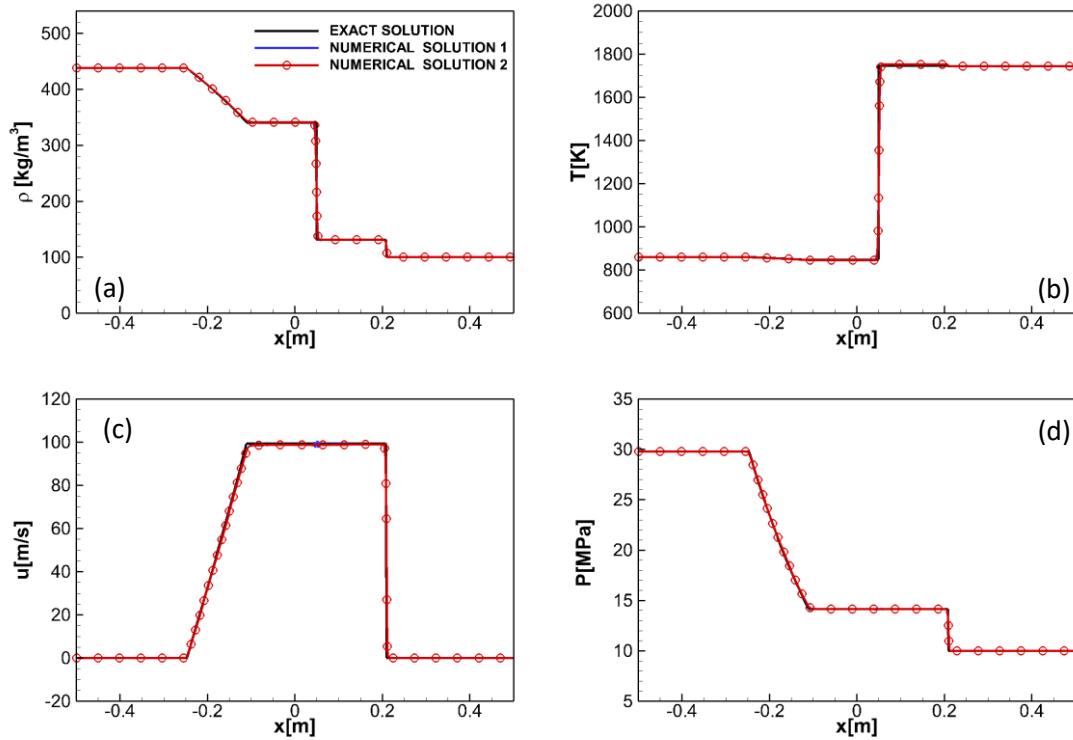


Figure 3.9: Shock Tube Problem 1 (Fifth-order WENO, Dodecane). CFL = 0.3, 1000 cells, $t=5 \cdot 10^{-4}$ s. Comparisons of (a) density, (b) temperature, (c) velocity and (d) pressure profiles: exact solution and numerical solutions. Numerical solution 1: Pressure and sonic fluid velocity computed at the faces using the EoS. Numerical solution 2: Pressure and sonic fluid velocity interpolated at the faces.

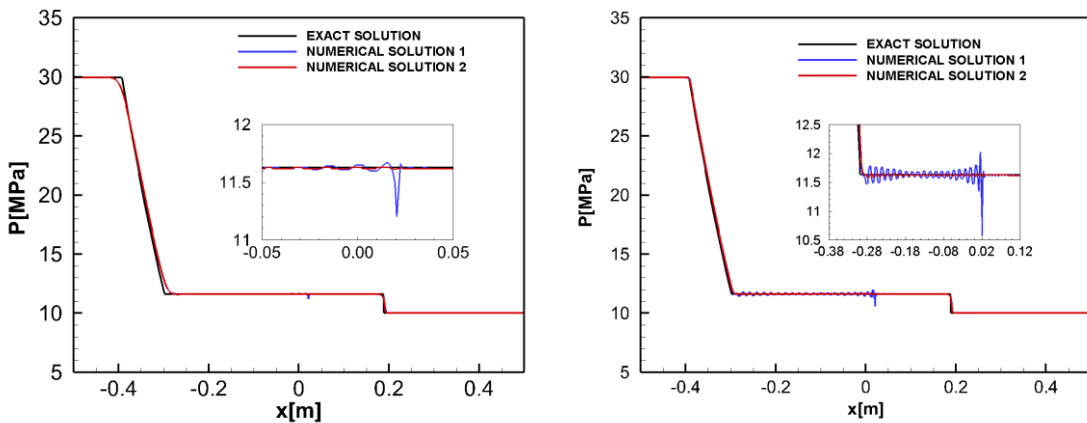


Figure 3.10: Shock Tube Problem 2 (Dodecane). CFL = 0.3, 1000 cells, $t=5 \cdot 10^{-4}$ s. Comparison of pressure profiles: exact solution and numerical solutions. Numerical solution 1: Pressure and sonic fluid velocity computed at the faces using the EoS. Numerical solution 2: Pressure and sonic fluid velocity interpolated at the faces. (a) MUSCL- Hancock scheme, (b) Fifth-order WENO.

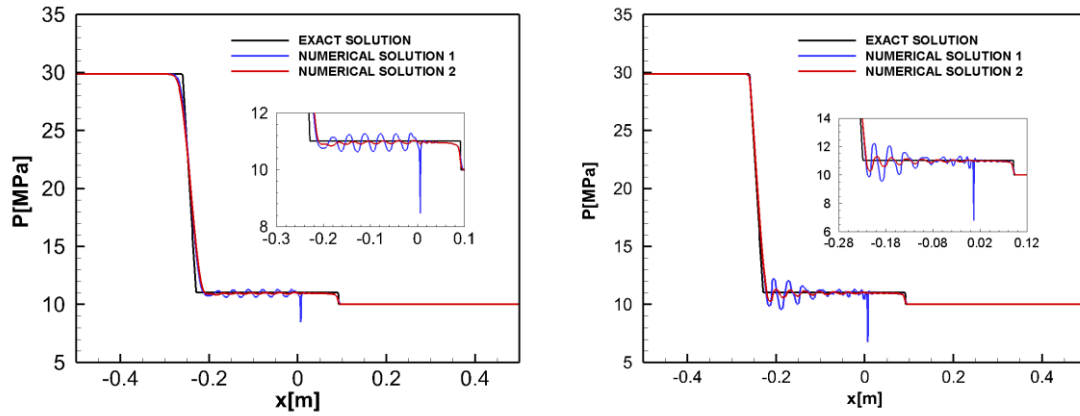


Figure 3.11: Shock Tube Problem 3 (Dodecane). CFL = 0.3, 1000 cells, $t=2.5 \cdot 10^{-4}$ s.

Comparison of pressure profiles: exact solution and numerical solutions. Numerical solution 1: Pressure and sonic fluid velocity computed at the faces using the EoS. Numerical solution 2: Pressure and sonic fluid velocity interpolated at the faces. of (a) MUSCL- Hancock scheme, (b) Fifth-order WENO.

Table 3.6: 2D Test Cases

| CASE A | Pressure [MPa] | Density [kg/m^3] | Temperature [K] |
|--------------------------|---------------------|------------------------------------|----------------------|
| JET (n-dodecane) | n-dodecane, 11.1 | n-dodecane, 400.0 | n-dodecane, 736.8 |
| CHAMBER (N_2) | N_2 , 11.1 | N_2 , 37.0 | N_2 , 972.9 |
| CASE B | | | |
| JET (V0a) | V0a, 11.1 | V0a, 490.0 | V0a, 742.2 |
| CHAMBER (N_2) | N_2 , 11.1 | N_2 , 37.0 | N_2 , 972.9 |

The PC-SAFT EoS is implemented using loops that depend on the number of components solved, which means that it takes more time to compute the properties of mixtures. This is the reason why the Diesel surrogate V0a will be used in the 2D simulation, as the results obtained using the two low accuracy surrogates (V0a and V0b) and the two high-accuracy surrogates (V1 and V2) are practically the same. The Diesel surrogate V0a is the one with less compounds.

3.2.4 Two-dimensional cases

The results of planar two-dimensional injections are presented in this section. As mentioned earlier, the fuels employed are n-dodecane and the Diesel surrogate V0a. A structured mesh is applied with a uniform cell distribution. The cell size is $5.5\mu\text{m} \times 5.5\mu\text{m}$. The domain used is $5\text{mm} \times 2.5\text{mm}$. The parabolic sub-step is included into these simulations, without sub-grid scale modelling for turbulence or heat/species diffusion. The CFL number is set at 0.5. The fifth-order WENO discretization scheme presented in Section 3.1 is used. Transmissive boundary conditions are applied at the top, bottom and right boundaries while a wall condition is employed at the left boundary. A flat velocity profile is imposed at the inlet. The velocity of the jet is 200 m/s and the diameter of the exit nozzle is 0.1mm. 405,000 cells are employed.

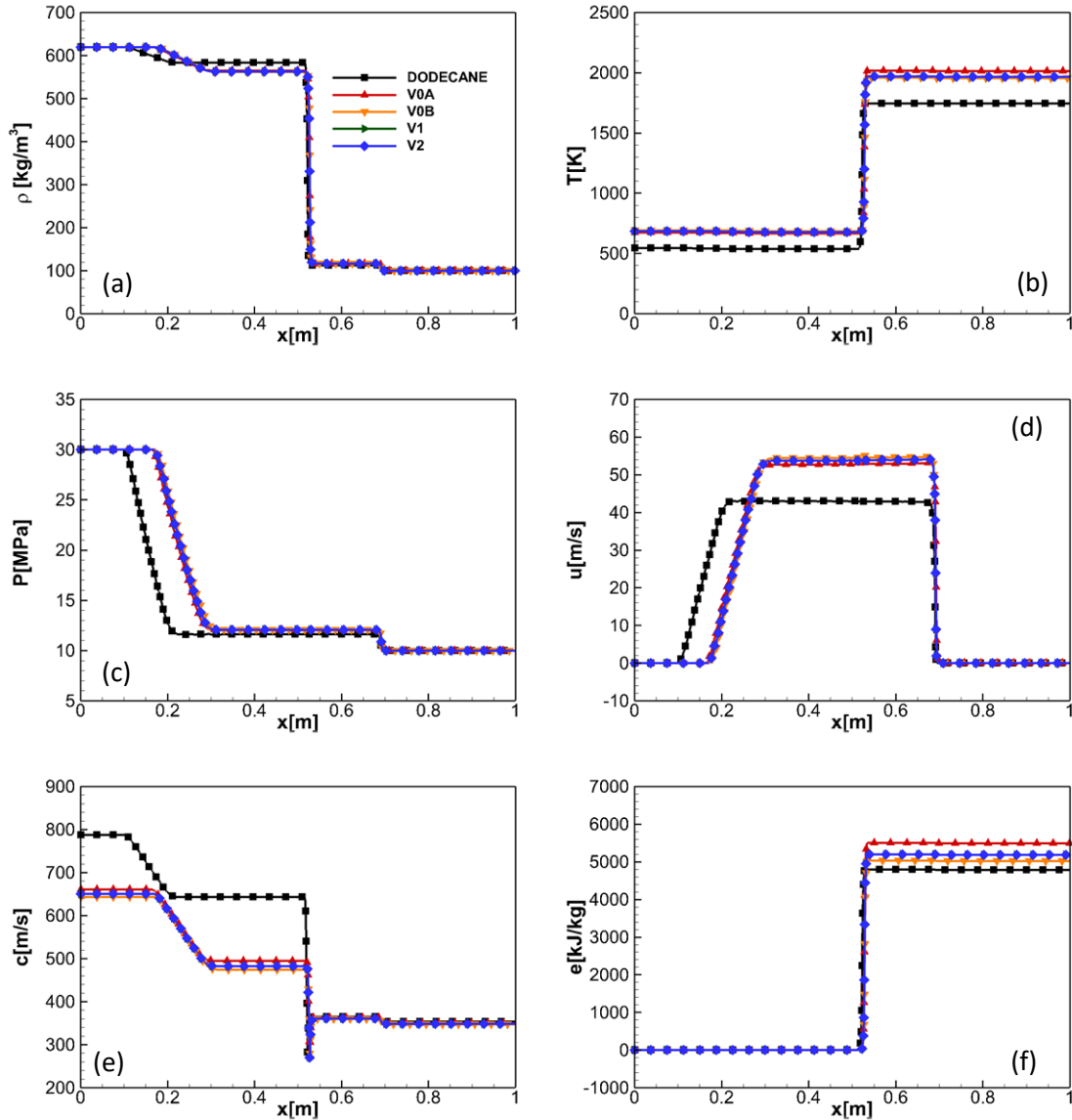


Figure 3.12: Shock Tube Problem 4. CFL = 0.8, 800 cells, $t=2.5 \cdot 10^{-4}$ s. Comparison of the (a) density, (b) temperature, (c) pressure, (d) x-velocity, (e) sonic fluid velocity, (f) internal using as working fluids dodecane and the surrogate Diesels.

N-dodecane jet

A multicomponent simulation has been included to prove the multi-species capability of the developed framework. Starting at the critical point of n-dodecane, the critical pressure of a $N_2 + n$ -dodecane mixture grows by increasing the nitrogen concentration [31]. It reaches higher pressures than the ones observed in Diesel engine combustion chambers (Figure 1.2). Thus, to avoid the VLE state the n-dodecane is injected at a temperature higher than its critical value in the performed simulation. The case is initialized using a pressure in the chamber of 11.1 MPa; the density and the temperature of the nitrogen in the chamber are 37.0 kg/m³ and 973 K (high-

load Diesel operation conditions [22]), respectively. The density and temperature of the jet are 400.0 kg/m^3 and 736.8 K , see Table 3.6.

The Kelvin Helmholtz instability is developing in the shear layer, as it can be seen in Figure 3.13. No pressure oscillations appear in the results. The jet is quickly heated-up from a liquid-like supercritical state to a gas-like supercritical state. A comparison of averaged scattered data of composition and temperature and an isobaric-adiabatic mixing process can be seen in Figure 3.14. As [83] stated, fully conservative schemes describe an isobaric-adiabatic mixing process.

The number of times the PC-SAFT model is solved in the hyperbolic operator per time step is lower than 20% the times it is employed using a classic FC implementation. As already mentioned, by interpolating the pressure and sonic fluid velocity at the cell faces, the EoS is solved once per cell in each RK sub-time step instead of once per cell face in the hyperbolic operator. Additionally, in many cells the EoS is not used to update the temperature, pressure, sonic fluid velocity and enthalpy values as the sum of the fluxes is approximately 0 (Section 3.1). This can be clearly observed in Figure 3.16. The significant reduction on the number of times the PC-SAFT model has to be solved allows to carry out simulations at affordable CPU times using a FC formulation. In the cases presented here, the time taken to solve $3.5 \times 10^{-5} \text{ s}$ were 93.8 hours on a single CPU.

Diesel surrogate V0a jet

This case is initialized using a pressure in the chamber of 11.1 MPa ; the density and the temperature of the nitrogen in the chamber are 37.0 kg/m^3 and 973 K (high-load Diesel operation conditions [22]), respectively. The density and temperature of the jet are 490.0 kg/m^3 and 742 K (Table 3.6). The temperatures encountered along the simulation are higher than the temperatures at which VLE exists, as can be seen in Figure 3.6. The binary interaction parameter used between the nitrogen and the Diesel compounds is the same one used in the nitrogen / n-dodecane mixture ($k_{ij} = 0.1446$).

Figure 3.17 shows the density, temperature and pressure at $3.4 \times 10^{-5} \text{ s}$. For this multi-component fuel simulations, the time taken to solve $3.5 \times 10^{-5} \text{ s}$ were 165 hours on the same CPU utilised for the n-dodecane simulation ($\sim 75\%$ longer). By knowing the mass fractions in each cell, it is possible to determine how many components are present in a cell a priori. The PC-SAFT is then only solved for that specific number of components. Most cells along the simulation in the combustion chamber contain only nitrogen. For this reason, this strategy significantly reduces the computational time. Like in the n-dodecane injection case, no pressure oscillations appear in the solution.

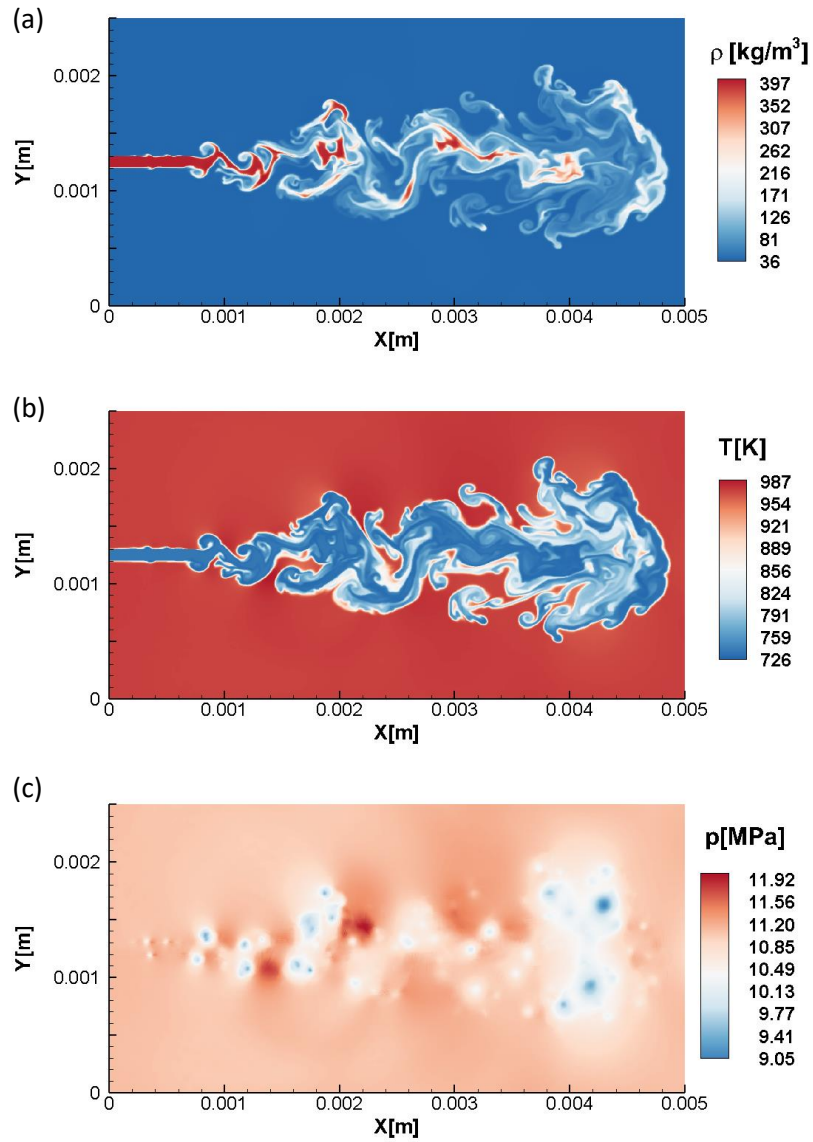


Figure 3.13: CFL = 0.5, 405000 cells. Results of the simulation of the supercritical n-dodecane jet at $t = 3.4 \times 10^{-5}$ s: (a) density, (b) temperature, (c) pressure.

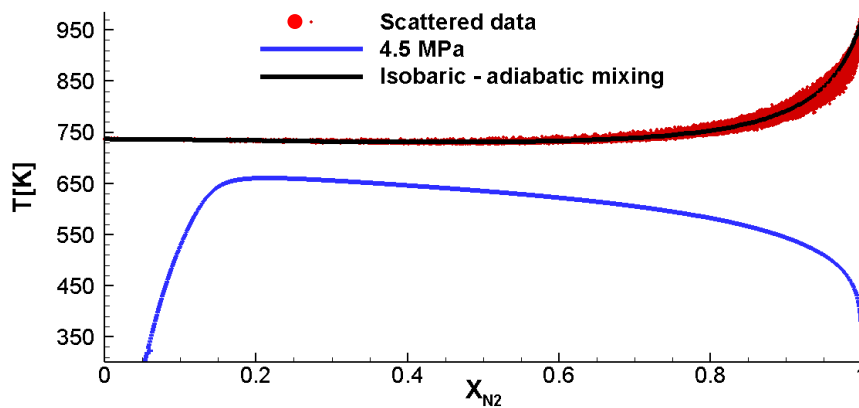


Figure 3.14: Scattered data of composition and temperature of the planar dodecane jet, dodecane-nitrogen phase boundary from VLE at 4.5 MPa and isobaric-adiabatic mixing line.

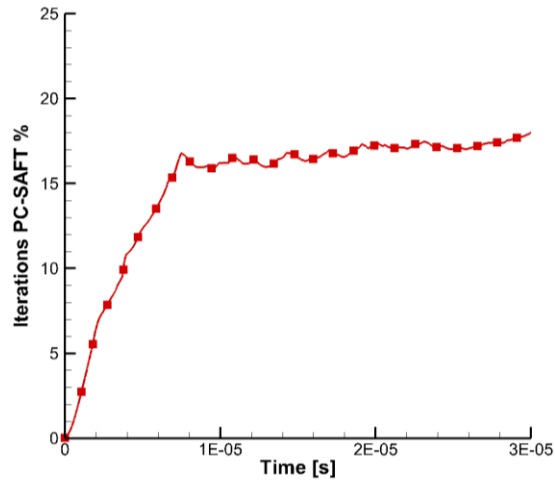


Figure 3.15: Percentage number of times the PC-SAFT model is solved in the hyperbolic operator respect a classic implementation of a FC formulation.

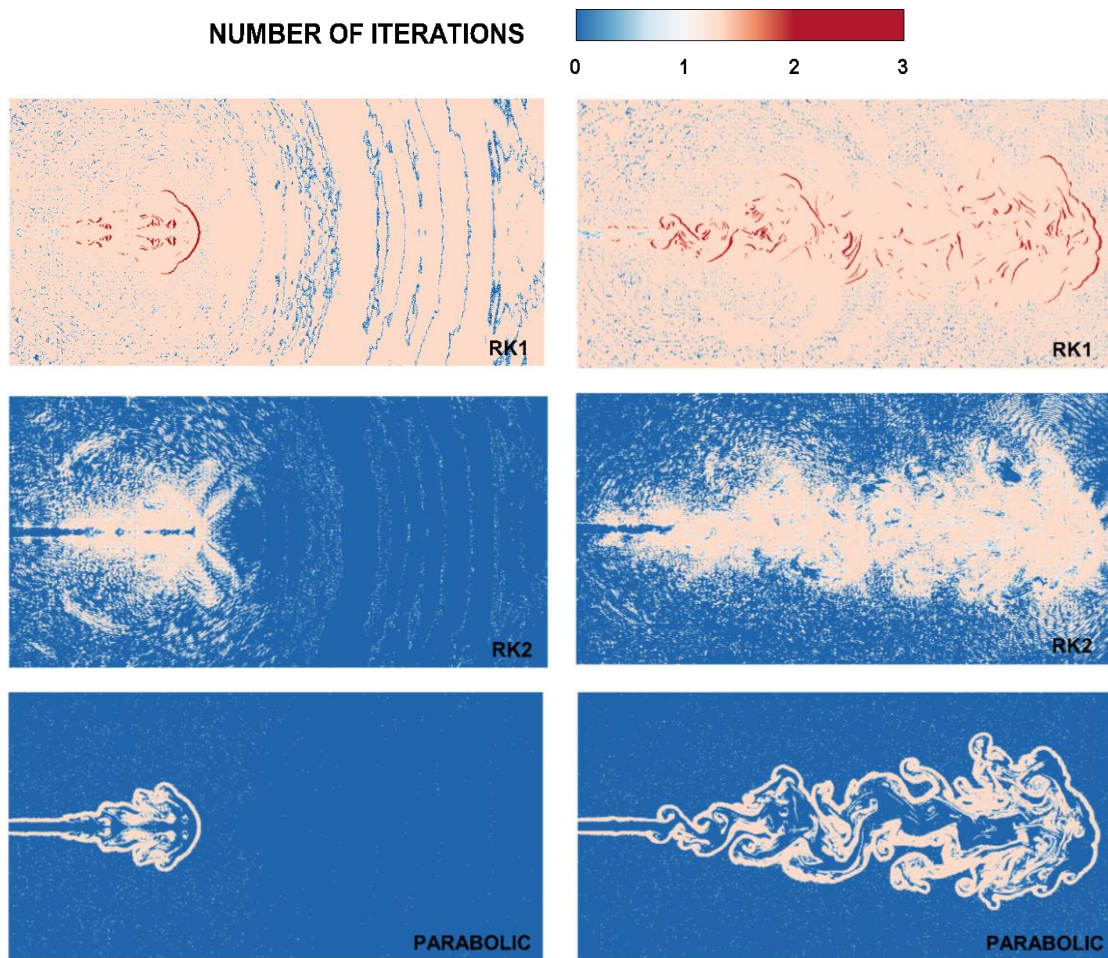


Figure 3.16: Number of times the PC-SAFT is solved per cell in the first RK sub-time-step (RK1), the second RK sub-time-step (RK2), and the parabolic operator at 1.24×10^{-5} s and 3.43×10^{-5} s.

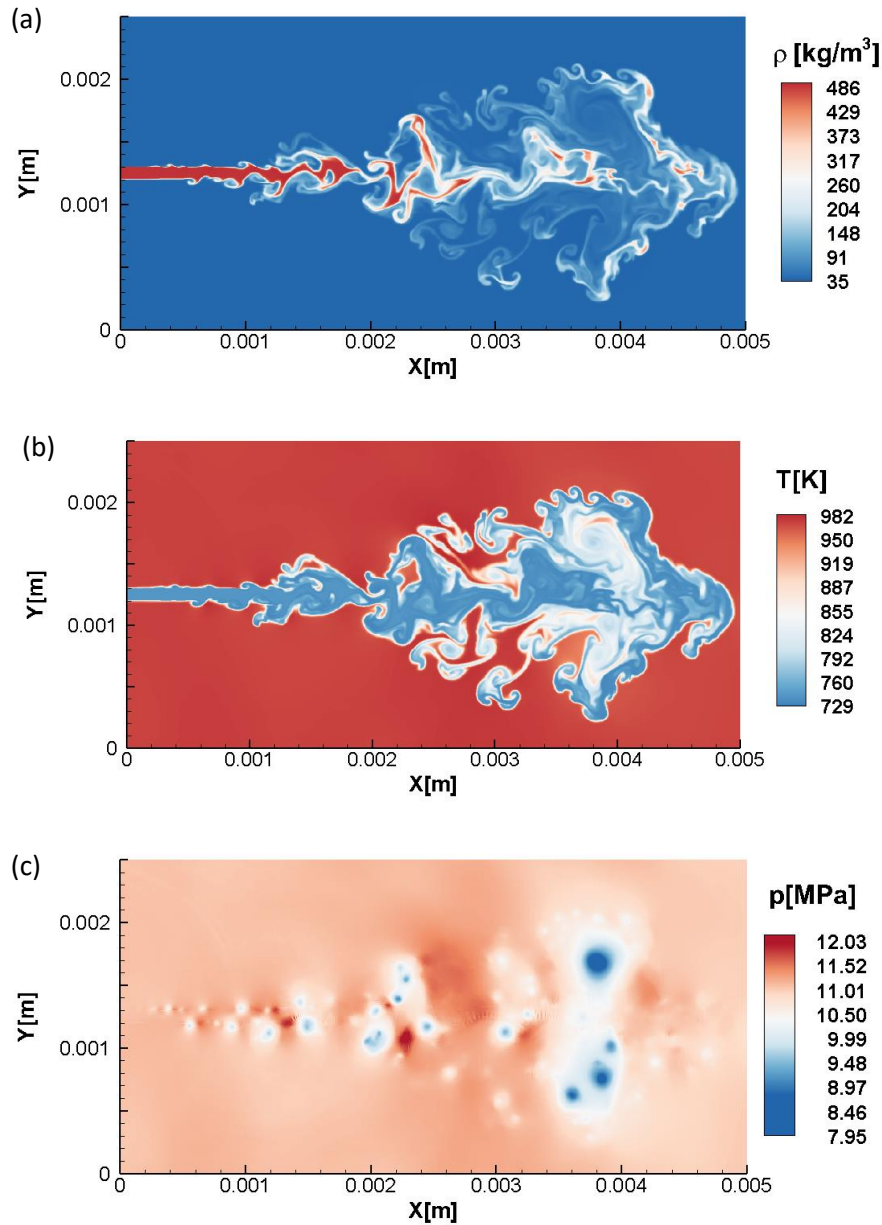


Figure 3.17: CFL = 0.5, 405000 cells. Results of the simulation of the supercritical Diesel surrogate V0a jet at $t = 3.4 \times 10^{-5}$ s: (a) density, (b) temperature, (c) pressure.

3.3 Conclusions

Four different Diesel surrogates have been tested and the thermodynamic properties have been modelled using the PC-SAFT EoS. This molecular-based EoS shows an accuracy similar to NIST, but without the need of an extensive model calibration; this is because only three parameters are needed to model a specific component. Moreover, it can easily compute the thermodynamic properties of multi-component mixtures, which is an additional advantage compared to NIST that supports only limited mixture combination. The Diesel surrogates utilised

can be divided into two types, depending on how closely they match the composition of Diesel fuel. All the multi-component surrogates tested show different properties than n-dodecane. Simulations at affordable CPU times can be carried out by reducing the number of times the PC-SAFT EoS is solved, by computing the pressure and sonic fluid velocity in the cell centres and performing a reconstruction of these variables at each cell face. This technique has been found to smooth-out the spurious pressure oscillations associated with conservative schemes when used along with real-fluid EoS. Additionally, if the updated conservative variables do not change with respect to the values obtained in the previous sub-time step, there is no need to use the EoS to update the values of the temperature, sonic fluid velocity, pressure and enthalpy stored at the cell centres. This strategy further reduces the overall simulation time. Advection test cases and shock tube problems have demonstrated the validity of the hyperbolic operator of the developed framework. Moreover, two-dimensional simulations of planar jets of n-dodecane and a four component Diesel surrogate (V0a) are included to demonstrate the capability of the scheme to predict supercritical Diesel fuel injection and mixing into air.

4. Simulation of subcritical Diesel jets at high-pressure conditions using the PC-SAFT EoS

The PC-SAFT has been coupled with VLE calculations in a density-based solver of the Navier-Stokes equations to perform multicomponent two-phase simulations of Diesel injections at high-pressure conditions [87]. Complex hydrocarbon mixtures have been modelled as single pseudo-components knowing the number averaged molecular weight and hydrogen-to-carbon ratio of the mixture. Additionally, published molecular dynamic simulations have been utilised to demonstrate that the developed algorithm properly captures the VLE interface at high-pressure conditions. Several advection test cases and sock tube problems were performed to validate the numerical framework using analytical and exact solutions. Moreover, two-dimensional simulations of n-dodecane and Diesel injections at subcritical conditions into nitrogen are included to demonstrate the multidimensional, multispecies and multiphase capability of the numerical framework.

4.1 Numerical method

The Navier-Stokes equations have been solved employing a finite volume method on a Cartesian numerical grid. Operator splitting as described in [73] is utilised to separate the hyperbolic and parabolic operators. The global time step is computed using the CFL (Courant-Friedrichs-Lewy) criterion of the hyperbolic part. A thermodynamic solver inspired by the work of [21] is employed to approximate the mixture thermophysical properties by performing PC-SAFT and VLE calculations.

4.1.1 CFD Code

The multicomponent HLLC solver is applied to solve the Riemann problem [37]. The conservative variables, pressure and speed of sound values needed to solve the Riemann problem are interpolated at the cell faces from cell centres using the fifth-order reconstruction scheme described in Chapter 3 [32]. The temporal integration of the hyperbolic operator is

carried out using a second-order Runge–Kutta (RK2) scheme applying the filter presented in Chapter 3 [32].

4.1.2 Diesel modelling

Two approximations have been considered to model the properties of Diesel.

Multicomponent Diesel surrogates

As explained in Chapter 3, four Diesel surrogates have been proposed in [70]. The V0a and V0b are two low-accuracy surrogates while V1 and V2 are the two higher-accuracy surrogates. Their molar composition is summarized in Table 3.2.

Pseudo-component method

In [72] was developed a technique that defines a single pseudo-component to represent the compounds found in a hydrocarbon mixture. It only requires two mixture properties as inputs, the number averaged molecular weight (MW) and hydrogen-to-carbon ratio (HN/CN). The group contribution (GC) parameters of [86] are used to develop the correlations shown in Table 4.1 for n-alkanes and poly-nuclear aromatics (PNAs) that numerically bound the pseudo-component PC-SAFT parameter values. An averaging parameter, Z , is used to calculate the pseudo-component parameters using eq.38-41. Equations 42-44 show that Z is calculated using MW and HN/CN ratio, which can be directly calculated knowing the mixture components or can be obtained using elemental analysis for unknown mixtures. Considering that the PC-SAFT is implemented using loops that depend on the number of components solved, this method allows us to model complex hydrocarbon mixtures as one component, thus, reducing significantly the computational requirements of the simulation but with increasing its accuracy.

$$m_{\text{pseudo-component}} = (1 - Z)m_{\text{n-alkane}} + Zm_{\text{PNA}} \quad (38)$$

$$(m\sigma)_{\text{pseudo-component}} = (1 - Z)(m\sigma)_{\text{n-alkane}} + Z(m\sigma)_{\text{PNA}} \quad (39)$$

$$\left(\frac{\varepsilon}{k}\right)_{\text{pseudo-component}} = (1 - Z)\left(\frac{\varepsilon}{k}\right)_{\text{n-alkane}} + Z\left(\frac{\varepsilon}{k}\right)_{\text{PNA}} \quad (40)$$

$$Z = \begin{cases} \frac{\text{DoU}_{\text{mixture}}}{\text{DoU}_{\text{PNA}}}, & \text{MW}_{\text{mixture}} < 178 \text{ g/mol} \\ \frac{\text{DoU}_{\text{mixture}}}{10}, & \text{MW}_{\text{mixture}} \geq 178 \text{ g/mol} \end{cases} \quad (41)$$

$$\text{DoU}_{\text{PNA}} = 0.05993 \times \text{MW} - 0.68158 \quad (42)$$

$$\text{CN}_{\text{mixture}} = \frac{\text{MW}_{\text{mixture}}}{12.01 + 1.01((\text{HN}/\text{CN})_{\text{mixture}})} \quad (43)$$

$$\text{DoU}_{\text{mixture}} = \frac{1}{2}(2 \times \text{CN}_{\text{mixture}} + 2 - \text{HN}_{\text{mixture}}) \quad (44)$$

The methodology developed by [72] was validated for modelling density, isothermal compressibility and volumetric thermal expansion coefficient of hydrocarbon mixtures, jet and diesel fuels. However, the pseudo-component must correctly model the internal energy (employed in the conservation of the total energy equation) speed of sound (used to calculate the hyperbolic fluxes and time step), enthalpy (employed in the parabolic operator of the Navier-Stokes equations) and fugacity coefficients (to perform VLE calculations). Using the PC-SAFT, the internal energy, enthalpy and heat capacities at constant pressure and volume (needed to compute the speed of sound) are computed as the sum of ideal and residual contributions. The PC-SAFT pure component parameters obtained employing the method of [72] are used to calculate the residual contributions. The ideal enthalpy of each component is calculated by integrating the ideal heat capacity at constant pressure with respect to temperature [88]. The molar composition of the mixture is used to calculate the ideal enthalpy of the mixture. The ideal internal energy of the mixture is computed employing the ideal enthalpy of the mixture. The ideal heat capacities at constant pressure of each component are computed employing the correlations published in [88]; then, molar fractions are used to compute the ideal heat capacity at constant pressure of the mixture, which is employed to calculate the ideal heat capacity at constant volume.

Table 4.1: PC-SAFT parameter correlations as a function of MW (g/mol) for n-alkanes and PNAs using the GC parameters of [86]

| | n-alkane | PNA |
|---------------------|------------------------------------|-----------------------------------|
| m | $0.0274\text{MW} + 0.4648$ | $0.0163\text{MW} + 0.9256$ |
| $m\sigma$ (Å) | $0.1092\text{MW} + 1.5677$ | $0.0612\text{MW} + 3.5324$ |
| ε/k (K) | $\exp(5.5811 - 10.2507/\text{MW})$ | $\exp(5.5657 - 8.6620/\text{MW})$ |

4.1.3 Thermodynamic solver (PC-SAFT + VLE)

The thermodynamic solver is employed to compute temperature, pressure, sound speed and enthalpy once the conservative variables have been updated. The inputs are the density, internal energy and mass fraction of the components. Three pure component parameters per compound (number of segments per chain, energy parameter and segment diameter) are specified for initialisation. Only an overview of the method is included in this section. Figure 4.1 shows a schematic representation of the CFD code. By interpolating the conservative variables, speed of sound and pressure at the cell faces in the hyperbolic operator, the thermodynamic solver can be directly applied to the updated conservative variables. Thus, it is not employed twice per cell face in each Runge-Kutta subtime-step [32]. In the parabolic operator, the conservative variables, temperature, and enthalpy are interpolated at the cell faces. Again, the thermodynamic solver is applied to the updated conservative variables.

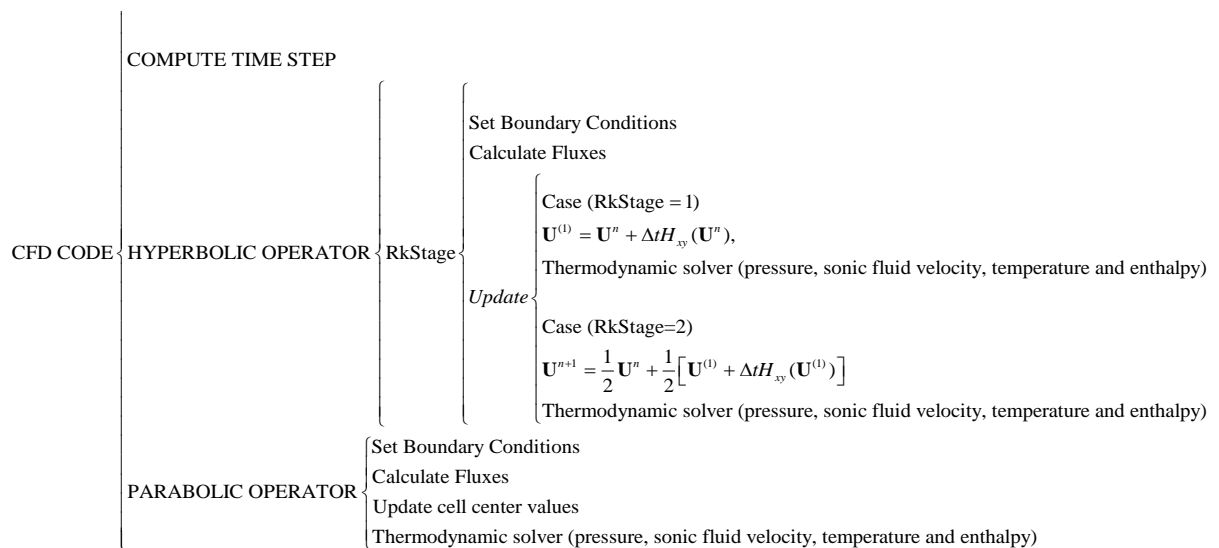


Figure 4.1: Schematic representation of the CFD code

Algorithm

1. **Filter.** The first step is to determine if only one phase exists checking the molar fractions of the components, see the schematic representation of the thermodynamic solver in Figure 4.2. This step is employed to decrease the computational time by reducing VLE calculations. By checking the molar fractions of the components, it can be determined whether only one phase exists. Isobaric-adiabatic lines can be computed using the initial conditions of the case of interest (temperature in the chamber, temperature of the fuel

injected and pressure in the combustion chamber) to determine the molar fractions at which VLE is not expected. As we can see in Figure 4.3, by performing an injection of n-dodecane at 363K in a combustion chamber at 900K and 11MPa, the nitrogen mole fraction at which the fuel starts vaporizing is close to 0.15. The VLE results were validated using the experimental results of [49], see Figure 4.4.

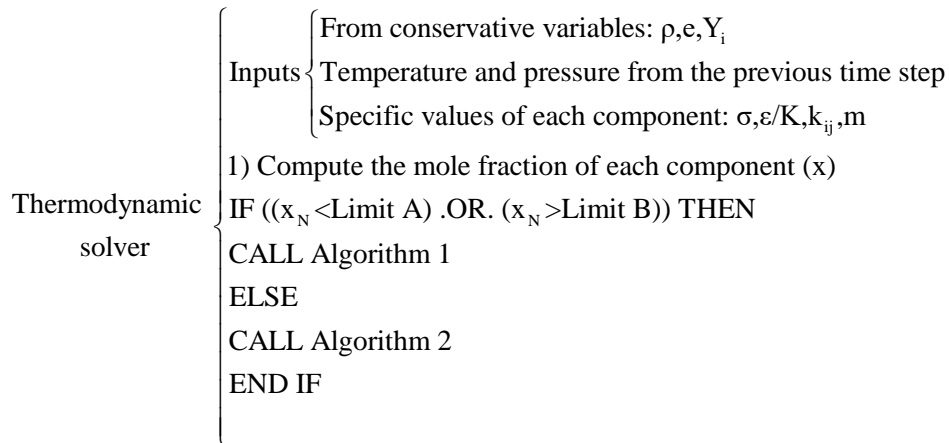


Figure 4.2: Schematic representation of the thermodynamic solver

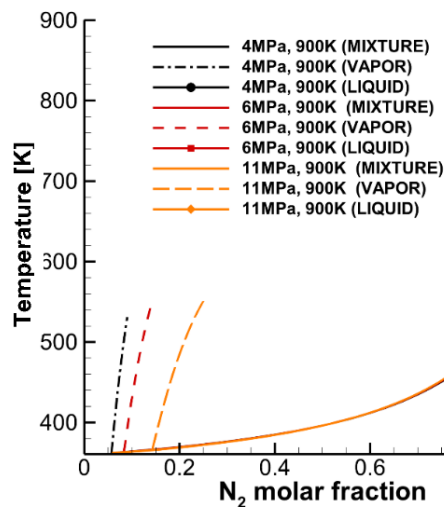


Figure 4.3: Isobaric-adiabatic mixing lines at different pressures in the combustion chamber

2. **One phase.** When knowing that the mixture is stable the molecular density of the mixture can be computed and used as an input to the PC-SAFT model. A Newton method is employed to compute the temperature that is needed to calculate the value of all other thermodynamic variables. The temperature dependent function used in the iterative method is the internal energy. The derivative of the internal energy with respect to the temperature at constant molecular density can be directly obtained as

these are the independent variables of the PC-SAFT model. This algorithm is explained in the Chapter 2.

3. **Two phases.** If the state of the mixture is unknown the density cannot be used as an input. The pressure and the temperature are iterated employing a multidimensional Newton method until the density and the internal energy obtained using the PC-SAFT + VLE calculations are the ones obtained from the conservative variables. For each P-T calculation a stability analysis is performed to determine if the mixture is stable (Appendix: Algorithm 2).

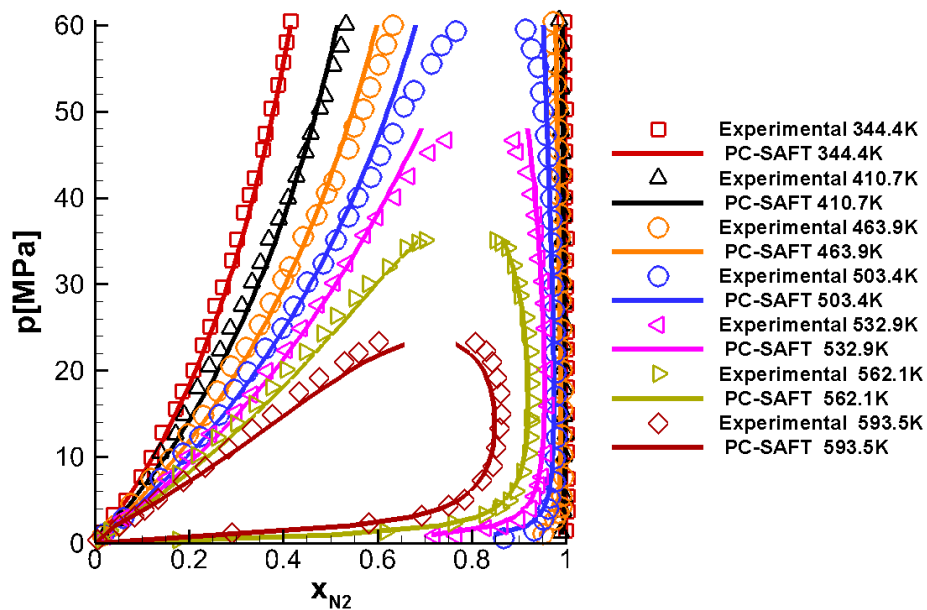


Figure 4.4: Experimental [49] and calculated pressure-composition phase diagram for the N₂ (1) + C₁₂H₂₆ (2) system. Solid lines: PC-SAFT EoS with $k_{ij} = 0.144$. It was computed using the thermodynamic algorithm described in the Appendix.

- a. **Mixture stable:** The PC-SAFT model is solved. The reduced density is iterated until the computed pressure is the input pressure (Appendix: Algorithm B).
- b. **Mixture unstable:** The isothermal-isobaric flash problem (TPn flash) is solved and the properties of the fluid in a VLE state are computed (Appendix: TPn algorithm, VLE properties).

4.1.4 VLE interface

In [15], molecular dynamic simulations of three n-alkane fuels into nitrogen under various temperatures and pressures were performed to study the injection, evaporation and mixing processes of hydrocarbon fuels into a supercritical environment. The study was focused on understanding the transition from classical two-phase evaporation to one-phase diffusion-controlled mixing. Using as threshold a dimensionless transition time (the time needed to transit from subcritical to supercritical respect to the liquid lifetime) of 0.35, the authors identified two regions on the P-T diagram, see Figure 4.5. Supercritical dominated: Due to the high critical pressures of TYPE IV mixtures, a VLE state is present at the beginning of the evaporation process. The temperature of the liquid core goes up until the VLE state disappears and only a diffusion-controlled mixing process exists. Subcritical dominated: A clear interface exists between the liquid core and the ambient gases. Nitrogen is not able to diffuse into the liquid core (constant fuel mass fraction close to 1 during evaporation, see Figure 4.7). There is a gradual decrease of the density of the liquid core as the fuel is heated up. The evaporation reaches a constant state with a constant liquid core.

According to the classification presented by [15], the combustion chamber of a Diesel engine working at medium-high load operation conditions is in the supercritical dominated regime after the compression cycle, see Figure 4.5. At these ambient conditions, the nitrogen is able to rapidly diffuse into the liquid core indicating that the interface has a Knudsen-number low enough to fall within the fluid mechanic continuum domain [11]. At 20MPa, the molar fraction of nitrogen in the liquid core (before the transition to a diffusion-controlled mixing process) at 0.5ns is almost 20%, see Figure 4.6. Therefore, the heat-up of the liquid core is dominated by diffusion phenomena. This can be proven by showing how isobaric-adiabatic mixing lines can replicate the heat-up profiles obtained in the molecular simulations of [15]. The isobaric-adiabatic lines where computed using eq.45. Figure 4.7 clearly shows how this hypothesis is not applicable in the subcritical dominated regime where after 5 ns the N₂ molar fraction in the liquid core has a constant value of 2%.

$$h_{mixture} = y_{C_{12}H_{26}} h_{C_{12}H_{26}} + y_{N_2} h_{N_2} \quad (45)$$

$$p = 20MPa$$

being y the mass fraction.

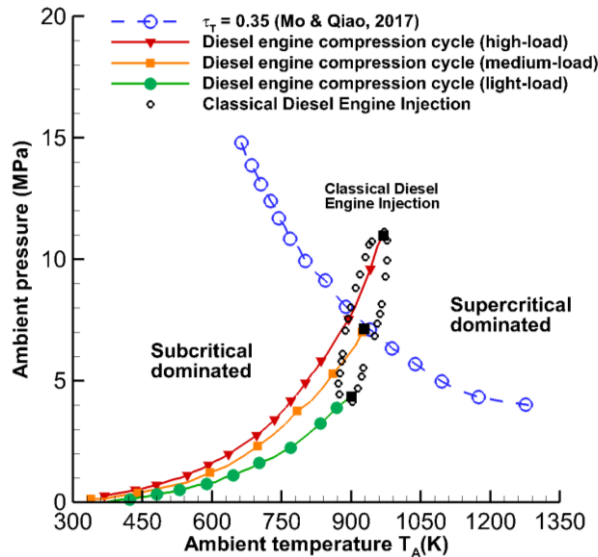


Figure 4.5: Diesel engine compression cycles [22] and contours of dimensionless transition time on pressure-temperature diagram of n-dodecane [15]

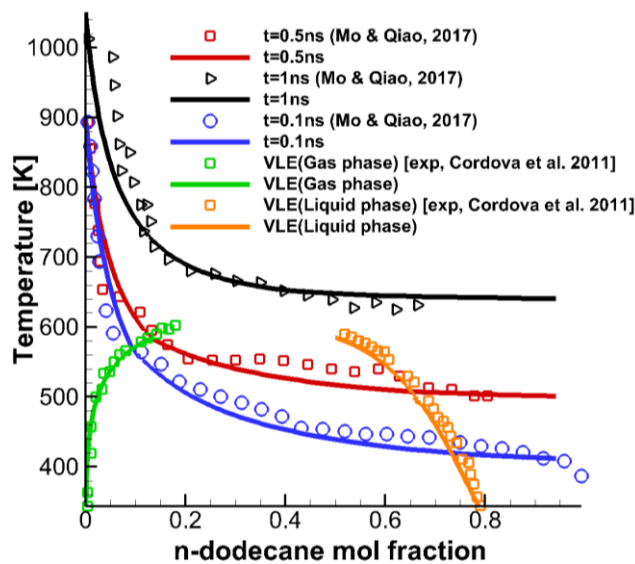


Figure 4.6: Development of gas-liquid interface shown on VLE diagram at 20 MPa [15], VLE experimental data [49] and isobaric-adiabatic mixing lines.

The hypothesis employed in this paper is that the vaporization process at high-pressure Diesel fuel injections is located at the subcritical vaporization stage of the supercritical vaporization regime described by [15] without a transition to the diffusion-controlled mixing process. Being the convective forces much more dominant than the diffusion phenomena, N₂-n-dodecane mixing takes place in a time several orders of magnitude lower than the one observed in Figure 4.6 where only diffusion is present. Thus, the heat-up of the jet describes a single isobaric-adiabatic mixing line instead of multiple adiabatic lines at different times. This can be corroborated observing the results obtained by [21], [22] where the heap-up of the heat follows an isobaric-adiabatic mixing line constant in time solving both, convection and diffusion

phenomena in their simulations. A diffuse interface method, which describe an adiabatic heat-up of the jet, must be applied during Diesel engine injection simulations at high-pressure conditions (supercritical dominated regime) to properly characterize how the fuel vaporize.

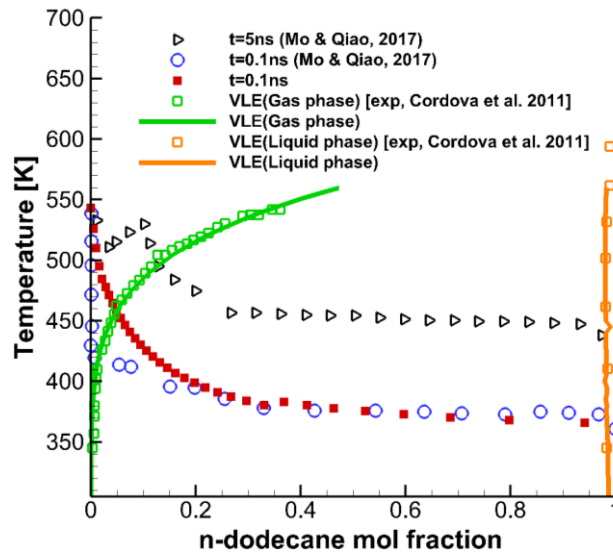


Figure 4.7: Development of gas-liquid interface shown on VLE diagram at 1 MPa [15], VLE experimental data [49] and isobaric-adiabatic mixing line.

4.1.5 Results

The working fluids employed are the following: (i) n-dodecane, (ii) a mixture of n-octane, n-dodecane and n-hexadecane; (iii) a pseudo-component that replicate the properties of the previous mixture; (iv) V0a Diesel, and (v) a pseudo-component that replicate the properties of the V0a Diesel.

Shock Tube Problems

Shock Tube Problem 1 (One phase, one component)

A shock tube problem is used to validate the numerical solution of the hyperbolic operator. The results are compared with an exact solution computed using the methodology described in [81]. N-dodecane is utilized as working fluid; the domain is $x \in [-0.5, 0.5]$ m; 300 equally spaced cells were employed; wave transmissive boundary conditions are used in the left and right sides; the simulated time is $5 \cdot 10^{-4}$ s; the initial conditions in the left state are $\rho_L=438\text{kg/m}^3$, $p_L=30\text{MPa}$, $u_L=0\text{m/s}$; and in the right state are $\rho_R=100\text{kg/m}^3$, $p_R=10\text{MPa}$, $u_R=0\text{m/s}$. Figure 4.8 shows how the density, temperature, velocity and pressure results agree with the exact solution.

Shock Tube Problem 2 (One phase, multicomponent/pseudo-component)

The working fluids employed are a mixture of n-octane, n-dodecane and n-hexadecane (Table 4.2) and a pseudo-component that replicate the properties of the mixture (Table 4.3) [72]. Figure 4.9 shows a comparison of the results obtained employing the multicomponent mixture and the results obtained by [72]. This comparison was performed to validate the PC-SAFT implementation in the code.

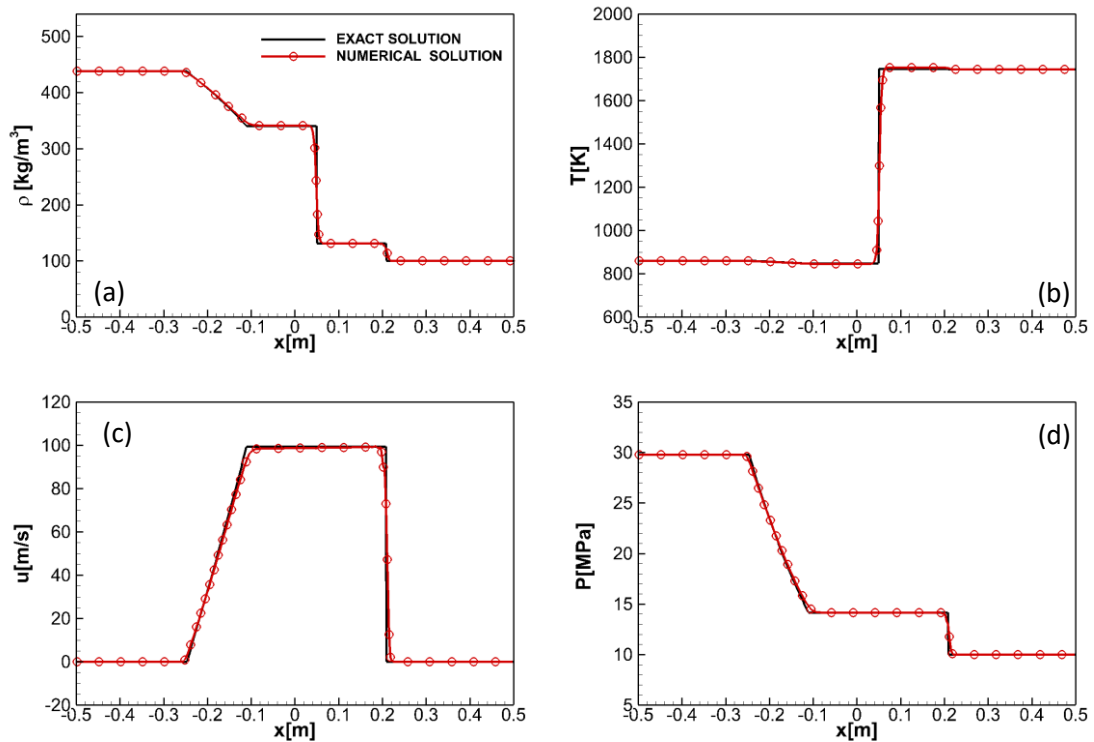


Figure 4.8: Shock Tube Problem. CFL = 0.5, $u = 0$ m/s, 300 cells, $t=5 \cdot 10^{-4}$ s. Comparisons of (a) density, (b) temperature, (c) velocity and (d) pressure profiles: exact solution and numerical solutions.

The domain is $x \in [-0.5, 0.5]$ m; 800 equally spaced cells were employed; wave transmissive boundary conditions are used in the left and right sides; the simulated time is $5 \cdot 10^{-4}$ s; the initial conditions in the left state are $\rho_L=438$ kg/m³, $t_L= 859.5$ K, $u_L=0$ m/s; and in the right state are $\rho_R=100$ kg/m³, $t_R=1744$ K, $u_R=0$ m/s. Figure 4.10 presents the density, temperature, pressure, velocity, speed of sound and internal energy results. The pseudo-component results are the same as the multicomponent ones indicating that the methodology developed by [72] can be used to model complex hydrocarbon mixtures as a pseudo-component in CFD simulations that present one phase.

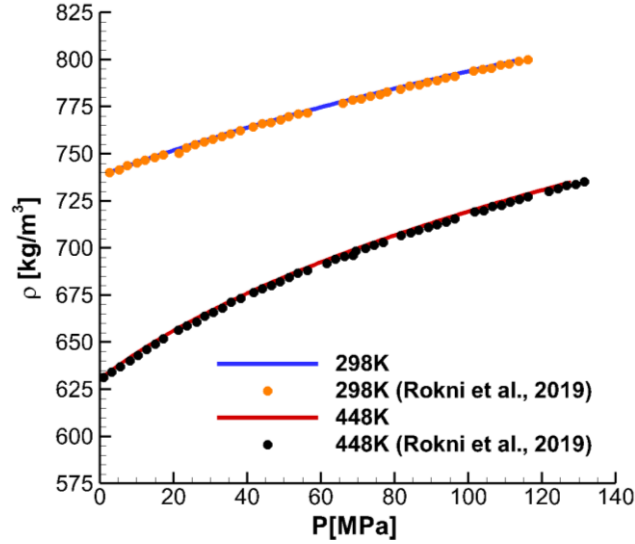


Figure 4.9: Density predictions for the hydrocarbon mixture presented in Table 4.2.

Table 4.2: Molar composition of hydrocarbon mixture employed in Shock Tube Problem 2 [72]

| Compound | Hydrocarbon mixture (Molar composition) |
|--------------|--|
| n-hexadecane | 0.232 |
| n-octane | 0.460 |
| n-dodecane | 0.232 |

Table 4.3: PC-SAFT pure component parameters employed to model the pseudo-component employed in Shock Tube Problem 2 [72]

| Compound | m | σ (Å) | ε/k (K) |
|------------------|-------|--------------|---------------------|
| Pseudo-component | 7.387 | 3.400 | 234.47 |

Advection test cases

The computational domain is $x \in [-10^{-5}, 10^{-5}]$ m; the simulated time is 10^{-6} s; the left initial conditions are fuel at $p=11$ MPa, $u=10.0$ m/s and $t=362$ K; the right initial conditions are nitrogen at $p=11$ MPa, $u=10.0$ m/s and $t=972$ K; a uniform grid spacing (100 cells) is applied; CFL is set to be 0.5; wave transmissive boundary conditions are implemented in the left and right sides of the computational domain; and a smooth initial interface is applied to reduce the initial start-up error [82]. When a diffuse interface method is employed, the interfaces are not sharp one-point jumps but smooth as they are resolved [82]. Thus, a smooth initial profile is a realistic initial condition. The initial interface was computed employing eq.46 [21].

$$Y_{FUEL} = 0.5 - 0.5 \operatorname{erf}\left\{\frac{(x_1 + 0.25l_{ref})}{(0.01l_{ref})}\right\} \quad (46)$$

The initialization of each cell located in the interface is performed knowing the pressure, enthalpy of the mixture (eq.46) and the molar fraction of the components.

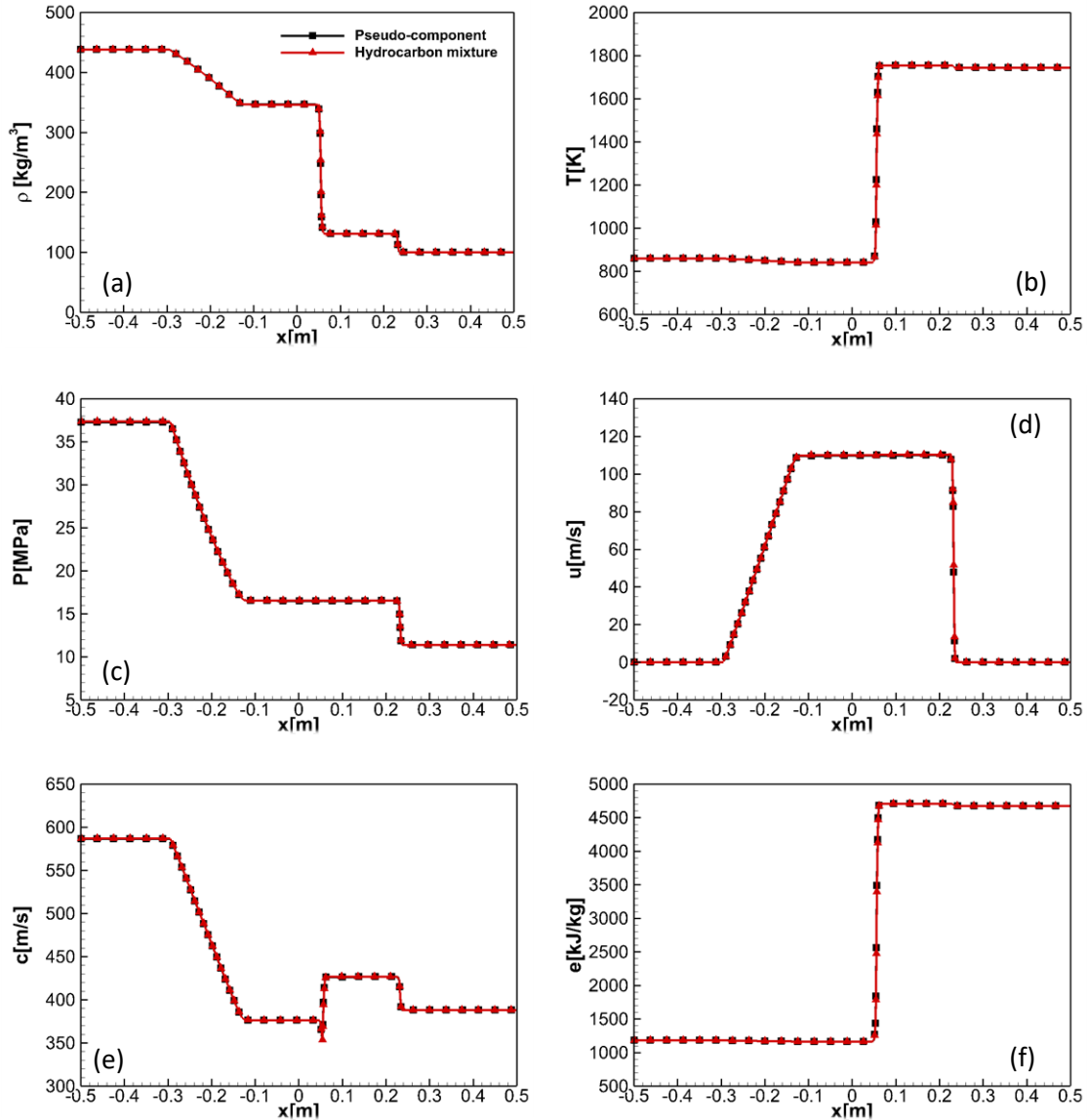


Figure 4.10: Shock Tube Problem 2. CFL = 0.5, 800 cells, $t=5 \cdot 10^{-4}$ s. Comparison of the (a) density, (b) temperature, (c) pressure, (d) x-velocity, (e) sonic fluid velocity, (f) internal energy using as working fluids are a mixture of n-octane, n-dodecane and n-hexadecane (Table 4.2) and a pseudo-component that replicate the properties of the mixture (Table 4.3) [72].

Advection test case 1 (Two phases, n-dodecane/nitrogen)

Figure 4.11 shows the results of this advection test case where n-dodecane is employed as fuel. The binary interaction parameter applied is $k_{ij} = 0.1446$. The numerical framework perfectly captures the large density and temperature gradients present in this multicomponent-multiphase one-dimensional test case. Small spurious pressure oscillations appear in the solution. This problem is well known in multicomponent density based codes employing highly non-linear EoS ([21], [33], [46]). The combination of VLE + PC-SAFT calculations allows to properly model: (1) the properties of n-dodecane at high-density ranges where cubic models

show large deviations in the sonic fluid velocity (used in density based CFD codes to compute the hyperbolic fluxes and time step [46]), temperature and internal energy; (2) and a correct (adiabatic) subcritical evaporation process in the interface.

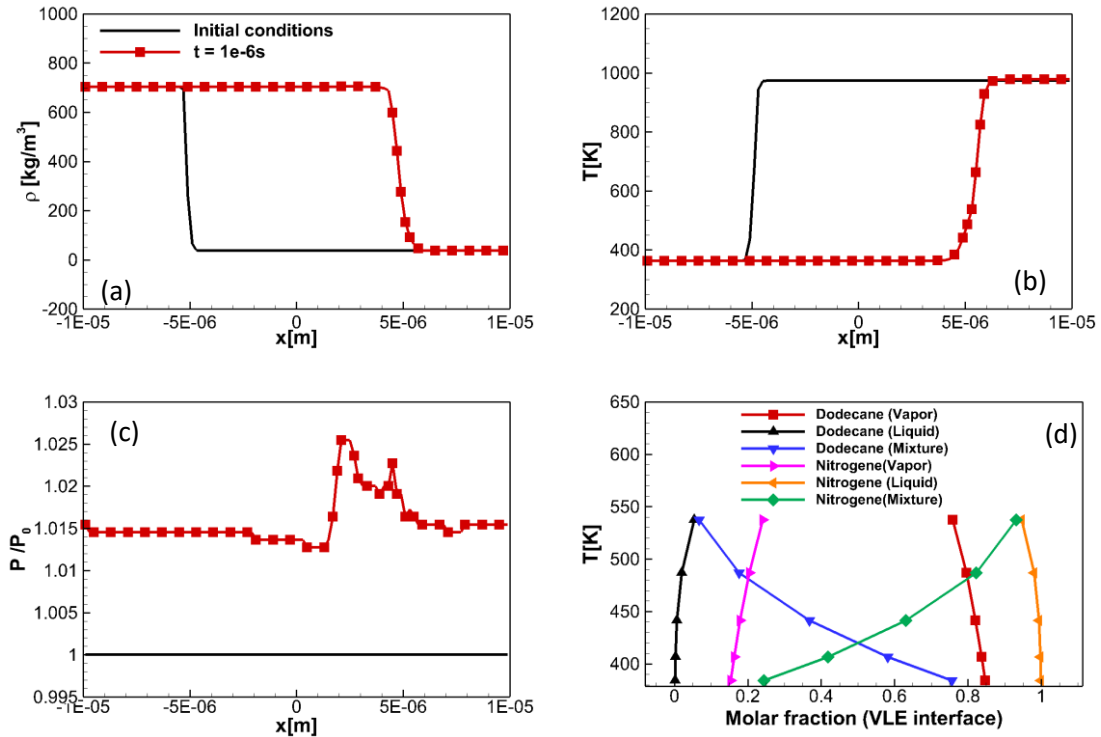


Figure 4.11: Advection Test Case 1 (N₂- C₁₂H₂₆), CFL = 0.5, $u = 10$ m/s, 100 cells. Results of (a) density, (b) temperature, (c) pressure and (d) VLE interface at 10^{-6} s.

Advection test case 2 (Two phases, V0a Diesel/ nitrogen, pseudo - V0a Diesel / nitrogen)

Figure 4.12 shows the temperature, density, speed of sound and internal energy results of an advection test case that employs the multicomponent Diesel V0a and the pseudo-Diesel V0a (Table 4.4) as fuels. The binary interaction parameter used between the nitrogen and the Diesel compounds or the pseudo-component is the same one used in the N₂/n-dodecane mixtures ($k_{ij} = 0.1446$). The pseudo-component presents an error (using as reference the multicomponent Diesel results) of 1.6% in density, 3.7% in sonic fluid velocity and 5.5% in internal energy. However, the computational time required to solve the multicomponent V0a Diesel advection test case is 432% the time consumed by the pseudo-Diesel advection test case. The different computational requirements will be even bigger in multidimensional cases or simulations where the hydrocarbon mixture presents more components (e.g., V0b, V1 and V2 Diesel surrogates). In the case of the Diesel surrogate V0a, the equilibrium state of five components must be computed in each cell of the interface, see Figure 4.13. Using the methodology of [72], the number of working fluids is limited to 2 (pseudo-Diesel + N₂).

Figure 4.14 shows how the phase boundary from VLE at 11MPa is different if the multicomponent Diesel V0a or its pseudo-component are employed. The use of a pseudo-component must not alter how the fuel is heat-up, especially in Diesel injection simulations where the temperature plays a significant role on determining the ignition time. However, Figure 4.15 presents how the results in the VLE interface are the same employing both working fluids (multicomponent mixture and pseudo-component. The mixture properties employing Diesel V0a or its pseudo-component are very similar along the isobaric-adiabatic mixing path found in the interface.

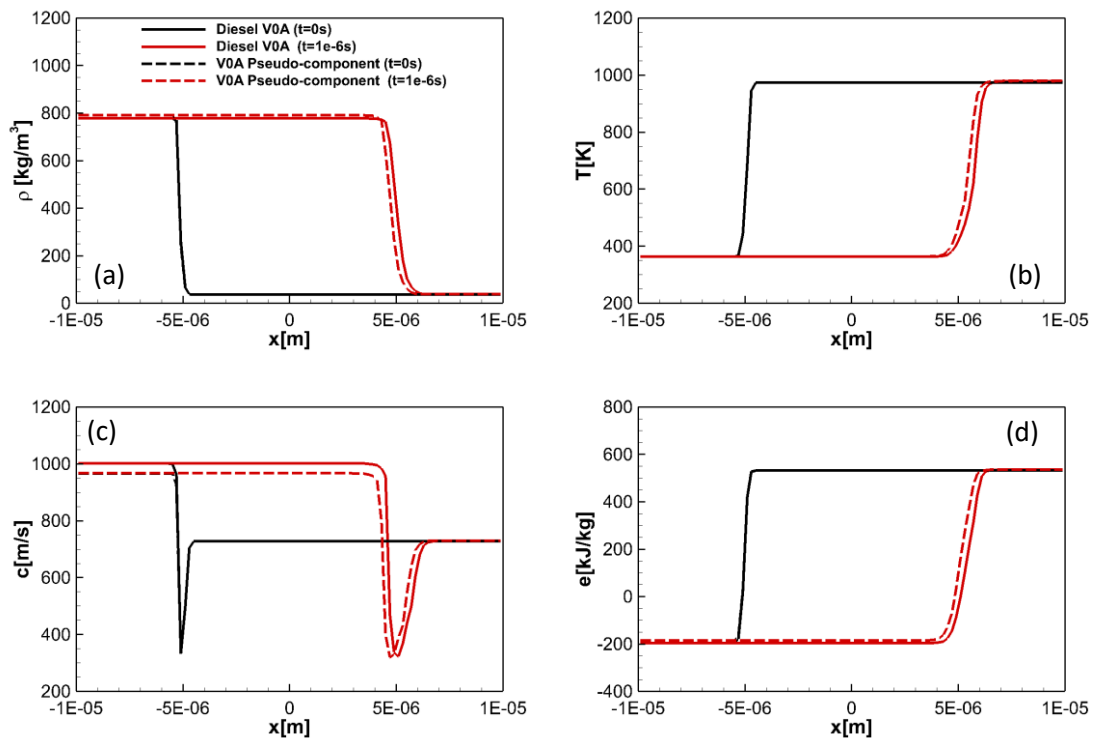


Figure 4.12: Advection Test Case 2 (N₂- V0a/ pseudo-Diesel V0a), CFL = 0.5, u = 10 m/s, 100 cells. Results of (a) density, (b) temperature, (c) speed of sound and (d) internal energy results at 10⁻⁶ s.

Two-dimensional cases

Planar two-dimensional injections of n-dodecane and a Diesel pseudo-component are presented to demonstrate the multidimensional capability of the numerical framework.

N-dodecane jet

A structured mesh is applied with a uniform cell distribution; the domain used is 12mm × 6mm; 1,216,800 cells are employed; the parabolic sub-step is included into these simulations without sub-grid scale modelling for turbulence or heat/species diffusion; the CFL number is set at 0.5; the fifth-order WENO discretization scheme presented in [32] is used; transmissive boundary conditions are applied at the top, bottom and right boundaries while a wall condition

Table 4.4: Pseudo-component PC-SAFT parameters employed to model the pseudo-Diesel V0a using the correlations developed by utilizing the GC parameters of Tihic et al. [86]

| Compound | m | σ (Å) | $\frac{\epsilon}{k}$ (K) |
|------------------|-------|--------------|--------------------------|
| Pseudo-component | 5.436 | 3.908 | 256.700 |

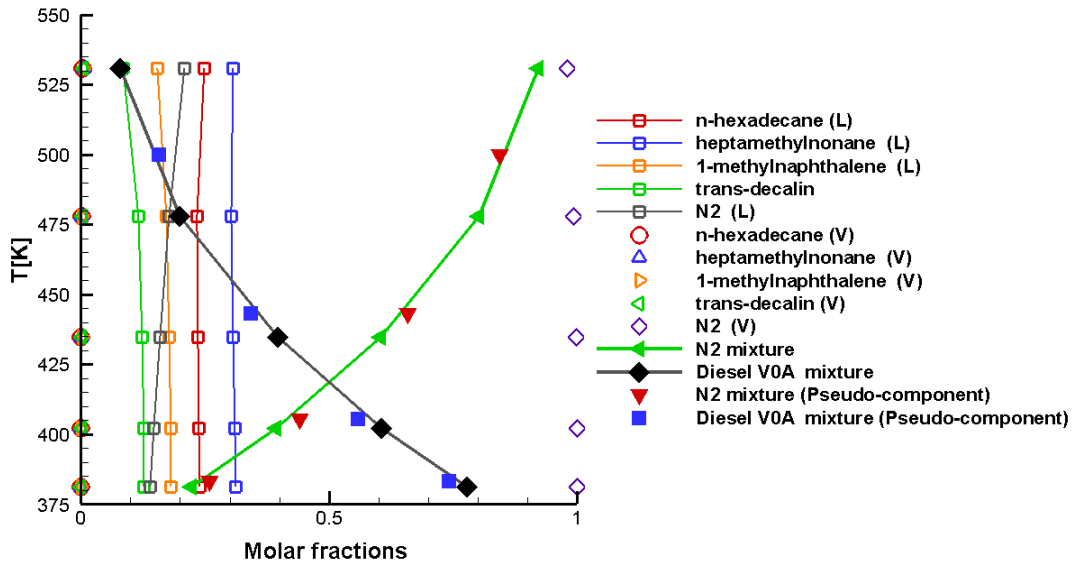


Figure 4.13: VLE Interface, Advection Test Case 2 (N₂- V0a/ pseudo-Diesel V0a), CFL= 0.5, u = 10 m/s, 100 cells. Results of VLE interface at 10⁻⁶s.

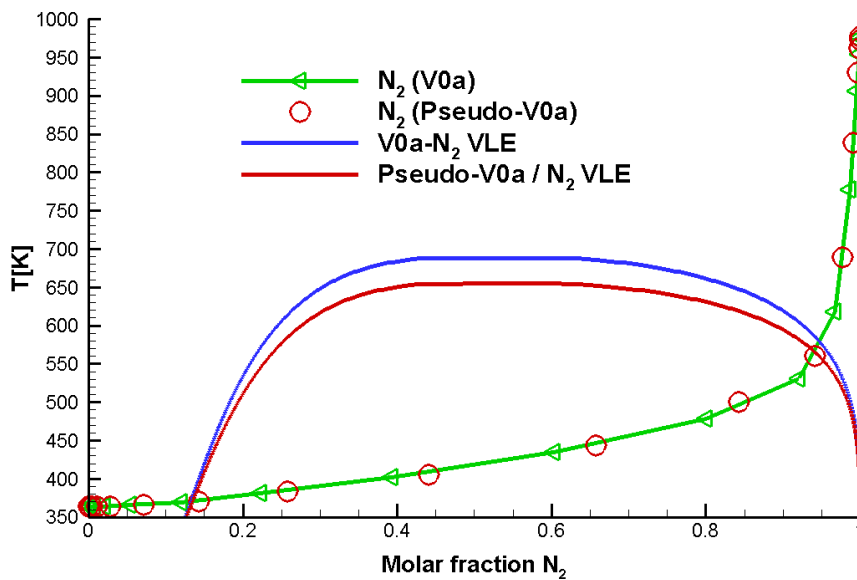


Figure 4.14: Advection Test Case 2 (N₂- V0a/ pseudo-Diesel V0a). Results of VLE interface at 10⁻⁶s and phase boundaries from VLE at 11MPa.

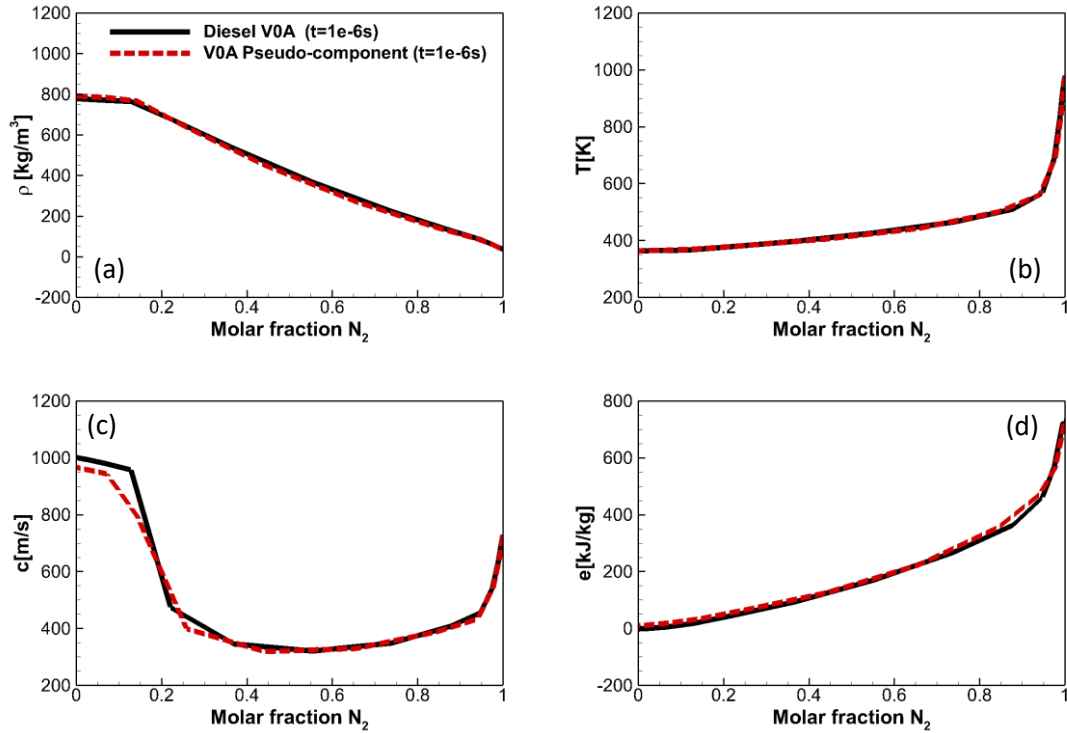


Figure 4.15: Advection Test Case 2 (N₂- V0a/ pseudo-Diesel V0a), CFL = 0.5, u = 10 m/s, 100 cells. Results of (a) density, (b) temperature, (c) speed of sound and (d) internal energy results at 10⁻⁶ s.

is employed at the left boundary; a flat velocity profile is imposed at the inlet; the velocity of the jet is 600 m/s; the diameter of the exit nozzle is 0.1mm; the case is initialized using a pressure in the chamber of 11 MPa; the temperature of the nitrogen is 973 K; and the temperature of the injected fuel is 363K. The binary interaction parameter applied is $k_{ij} = 0.1446$. The loops where the hyperbolic fluxes, parabolic fluxes, update of conservative variables and thermodynamic solver are solved were paralleled employing OpenMP (24 physical cores where employed). Some instabilities were observed in the initialization as [21] reported. To solve this problem, a ramp is used to accelerate the fuel to 600m/s. The jet is quickly heated-up from a compressed liquid state to gas and finally, to a supercritical state describing an isobaric-adiabatic mixing line, see Figure 4.16. Figure 4.17 shows how the Kelvin Helmholtz instability and ligament-shaped structures are developed in the shear layer.

Diesel jet

The initial conditions and set-up of the simulation is the same as the n-dodecane jet. The binary interaction parameter applied is $k_{ij} = 0.1446$. Figure 4.18 shows the density, temperature, pressure and overall vapor fraction on a molar basis at 3.04×10^{-5} s. The computational time required to solve at 3.3×10^{-5} s was 91.7 hours. A lot of time is invested on solving the

multidimensional Newton method of the cells that are in a VLE state. At these conditions, the derivatives of the Jacobian matrix are calculated numerically; the developed methodology is fast enough to perform simulations at affordable time scales. It should also be considered that the results are equivalent to a multicomponent injection of a Diesel surrogate of 4 components that vaporize when mixed with hot nitrogen. If the multicomponent surrogate was modelled as a pseudo-component with a higher number of compounds (e.g., V0b, V1 and V2 Diesel surrogates), the simulation time would be practically the same. This methodology makes the simulation time independent of the number of compounds present in the fuel and thus, allowing the real composition of a specific fuel to be utilised in CFD simulations.

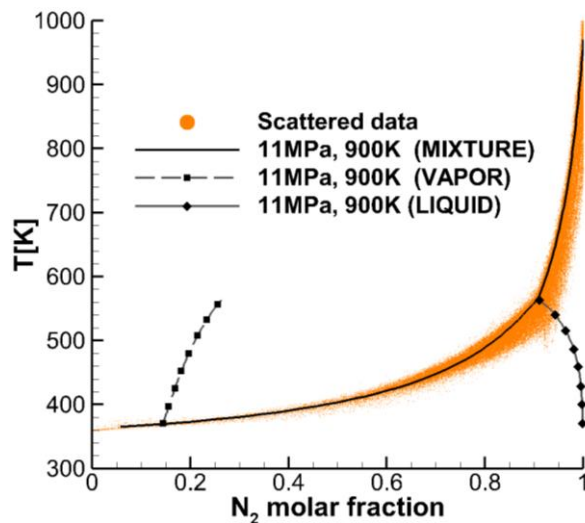


Figure 4.16. Scattered data of composition and temperature of the planar n-dodecane jet, dodecane-nitrogen phase boundary from VLE at 11MPa and isobaric-adiabatic mixing line.

4.2 Conclusions

This chapter presents a numerical framework that combines PC-SAFT and VLE calculations in a density-based, fully conservative solver of the Navier-Stokes and energy conservation equations to simulate fuel-air mixing at high-pressure conditions. By coupling VLE calculations with the PC-SAFT model, subcritical simulations can be carried out. A purely predictive method that employs the PC-SAFT EoS for developing pseudo-components, which are defined to replicate the properties of complex hydrocarbon mixtures (e.g., Diesel fuels), has been completed and validated to be used in CFD simulations. Then, complex hydrocarbon mixtures can be modelled as a single pseudo-component knowing their number averaged molecular weight and hydrogen-to-carbon ratio. The results obtained employing the multicomponent Diesel V0a and its pseudo-component in a fuel-N₂ advection test case show minimum

differences in density (1.6%), sonic fluid velocity (3.7%) and internal energy (5.5%). However, using a multicomponent surrogate significantly increase the computational requirements. The time required to solve the multicomponent V0a Diesel advection test case was 432% the time consumed by the same case employing its pseudo-component as fuel. Greater differences are expected in multidimensional cases (more cells would be in a VLE state as the contact surface of the jet and the nitrogen increases) or simulations where the hydrocarbon mixture presents more components (e.g., V0b, V1 and V2 Diesel surrogates). Additionally, several advection test cases and sock tube problems were performed to validate the numerical framework using analytical and exact solutions. Two-dimensional simulations of n-dodecane and Diesel injections into nitrogen are included to demonstrate the multidimensional, multispecies and multiphase capability of the numerical framework.

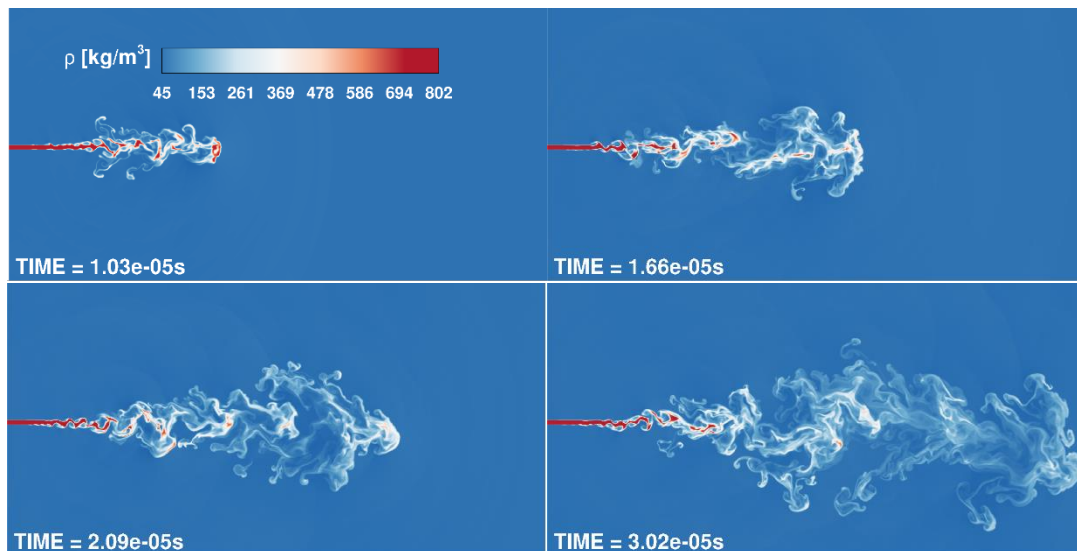


Figure 4.17: Density results of n-dodecane planar jet.

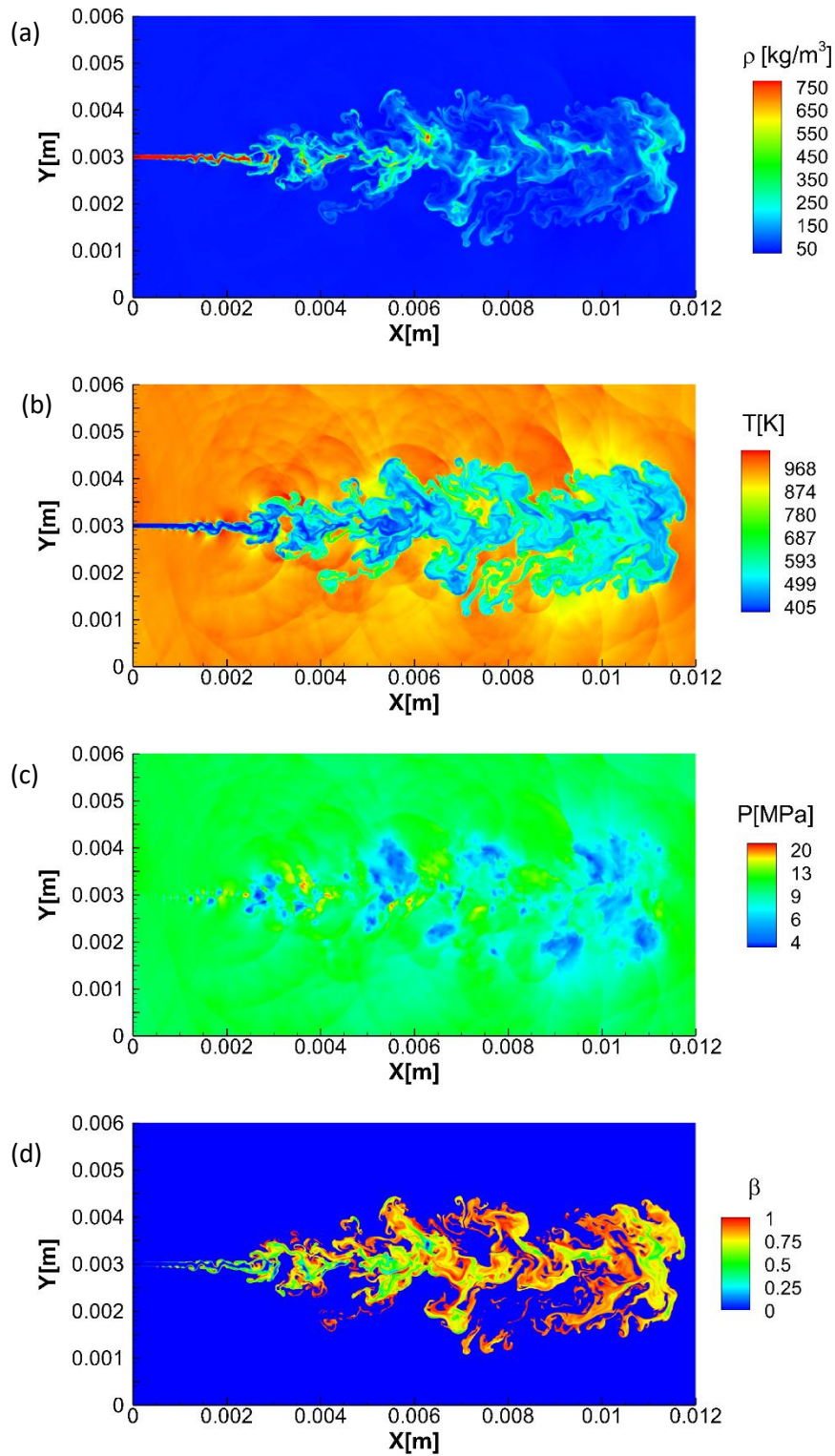


Figure 4.18: CFL = 0.5, 1,216,800 cells. Results of the simulation of the VOA Diesel pseudo-component jet at $t = 3.04 \times 10^{-5}$ s.: (a) density, (b) temperature, (c) pressure, and (d) overall vapor fraction on a molar basis.

5. Conclusions and future work

5.1 Conclusions

The conclusions of this thesis are the following:

- A new numerical framework has been developed to simulate supercritical, transcritical and subcritical injections at Diesel engine relevant conditions using a compressible density-based solver of the Navier-Stokes equations along with the conservative formulation of the energy equation. For the first time, the PC-SAFT has been used to close this system and compute properties of the working fluids.
- Both conservative and a quasi-conservative formulation (double flux model of [33], [35], [53] is applied) were tested.
 - It was observed that the conservative formulation generates spurious pressure oscillations, as reported with other diffuse interface density-based codes employing a real-fluid EoS. In 2D simulations, since the interfaces are not sharp one-point jumps but smooth as they are resolved, the wiggles generated do not compromise the stability of the simulation.
 - The quasi-conservative scheme can model supercritical and transcritical single- and multicomponent cases without spurious pressure oscillations. However, errors in the energy conservation that appear employing this formulation may produce an unphysical quick heat-up of the jet in multicomponent cases making these schemes inadequate for Diesel injection simulations where the temperature plays a significant role in determining the ignition time. The energy conservation error was higher using the PC-SAFT model than PR EoS in the analysed cases.
- A fully conservative formulation which employs a new spatial reconstruction technique was developed: first, the pressure and sonic fluid velocity are computed at the cell centres once the conservative variables have been updated in each Runge-Kutta sub-time step of the hyperbolic operator; then, these variables are reconstructed at the cell faces to solve the Riemann problem. This technique allows one to perform practical CFD simulations using complex EoS at affordable CPU times (the number of times the PC-SAFT model is solved in the hyperbolic operator per time step is lower than 20% the times it is employed using a classic FC implementation in the 2D simulations performed). Additionally, it smooths-out the previously observed spurious pressure oscillations.

- The results obtained by the PC-SAFT EoS to model Diesel shows the highest degree of agreement with experimental values in comparison with the results obtained when applying the method developed at NIST (AAD% for density (kg/m³) at 293.15K and 0.1MPa lower than 1.03% in the analysed Diesel surrogates).
- A purely predictive method that employs the PC-SAFT EoS for developing pseudo-components, which are defined to replicate the properties of complex hydrocarbon mixtures (e.g., Diesel fuels), was validated and completed to be used in CFD simulations. This methodology makes the simulation time independent of the number of compounds present in the fuel and thus, allowing the real composition of a specific fuel to be utilised in practical CFD simulations (the time required to solve a four-component Diesel advection test case was 432% the time consumed by the same case employing a pseudo-component). The pseudo-component developed correctly captures the evaporation process of the multicomponent Diesel surrogates in the VLE interface.
- The properties of Diesel fuel were modelled as: multicomponent surrogates of four, five, eight and nine components divided into accuracy types, depending on how closely they match the composition of real Diesel; or as a pseudo-component that replicates the properties of a specific multicomponent surrogate. To the best of the author's knowledge, this is the first time that real Diesel composition is considered in CFD simulations using a molecular based model. All the multi-component Diesel surrogates tested show different properties to n-dodecane, a working fluid commonly used in CFD simulations to model Diesel fuel.
- PC-SAFT is an alternative to cubic EoS, which show low accuracy when computing the thermodynamic properties of hydrocarbons at temperatures that are typical for today's high-pressure fuel injection systems.
- VLE calculations were included to simulate injections where the fuel enters the combustion chamber at low temperatures (subcritical injections). Due to the computational requirements of computing the VLE state of multiple components, it is necessary to model the Diesel surrogates as single pseudo-components to perform simulations at affordable CPU times.
- One-dimensional simulations (shock tube problems and advection test cases) were performed to validate the numerical framework against analytical and exact solutions.
- Planar two-dimensional simulations of supercritical, transcritical and subcritical injections were performed to demonstrate the multidimensional, multispecies and multiphase

capability of the developed code. Nitrogen, n-dodecane and Diesel were used as working fluids.

- Published molecular dynamic simulations have been employed to demonstrate that the numerical framework properly captures the multicomponent VLE interface of subcritical injections at high-pressure conditions.
- The framework was developed as a first complete step of a modelling approach, hence the physics of transcritical, supercritical and subcritical injection were not part of the objectives. It has been performed the validation of the thermodynamic algorithm employing experimental results; validation of the CFD code with exact and analytical solutions; and a validation of the pseudo-component method. Moreover, it is proven that no pressure oscillations are present in the solution, the jet is heated-up correctly; the algorithm is stable; and practical simulations can be performed. The next step is the implementation of this numerical algorithm in OpenFOAM and simulate Diesel jets for which we have experimental results.

5.2 Future work

The coupling of a SAFT variant (the PC-SAFT), Navier-Stokes equations, energy conservation equation and VLE calculations in a same numerical framework, allows one to exploit the great capabilities of these molecular based models in CFD simulations. Taking this into account, my recommendations for future work are:

Spray systems

- To solve the in-nozzle flow and Diesel spray in a single domain. Cavitation can be captured in a numerical framework where the PC-SAFT EoS is used along with VLE calculations. [89] carried out an experimental and numerical study to analyse the influence of in-nozzle flow, cavitation and fuel properties on the Diesel spray. The authors showed how cavitation can spread throughout the nozzle hole, reach the exit and influence the evolution of the spray. They observed the collapse of cavitation structures in the spray jet and its asymmetric shape provoked by cavitation inception in the nozzle hole and collapse of cavitation structures. It would be interesting to capture in a single simulation all these phenomena and analyse how the different vaporization rates of the Diesel compounds affect the injection process.
- To simulate a complete gasoline cycle, as proposed by [21]. Different multicomponent surrogates and pseudo-components could be developed to model the properties of gasoline.
- To perform supercritical cryogenic jet simulations. In liquid rocket engines, cryogenic propellants are injected into combustion chambers at supercritical pressure conditions, then mixing and combustions takes place. The developed numerical framework can be used to capture the mixing process and easily model the properties of the different propellants.

Natural gas

- To model the different processes involved in the storage or transport of natural gas. Natural gas is a relatively clean source of energy (compared to other fossil fuels), whose use has increased significantly in recent years. In order to deliver it to the consumers it is subjected to several processes such as compression, liquefaction or pressure drop [5].

PC-SAFT can accurately predict the thermodynamics properties of natural gas and similar mixtures in a wide range of temperature and pressure [5].

Biological and chemical engineering

- To couple the electrolyte Perturbed-Chain Statistical Association Theory (ePC-SAFT) variant developed by [90] with the Navier-Stokes equations and energy equation to model electrolyte solutions. These systems can be found in different applications like waste and drinking water treatment, fertilizer production, electrolysis, enhanced oil recovery or osmosis and reverse osmosis of aqueous solutions [91]. High accuracy thermodynamic can be very relevant in the CFD simulations employed to simulate these processes.

Appendix

Figure A1 shows a schematic representation of the CFD code. By interpolating the conservative variables, speed of sound and pressure at the cell faces in the hyperbolic operator, the thermodynamic solver can be directly applied to the updated conservative variables. Thus, it is not employed twice per cell face in each Runge-Kutta subtime-step [32]. In the parabolic operator, the conservative variables, temperature, and enthalpy are interpolated at the cell faces. Again, the thermodynamic solver is applied to the updated conservative variables.

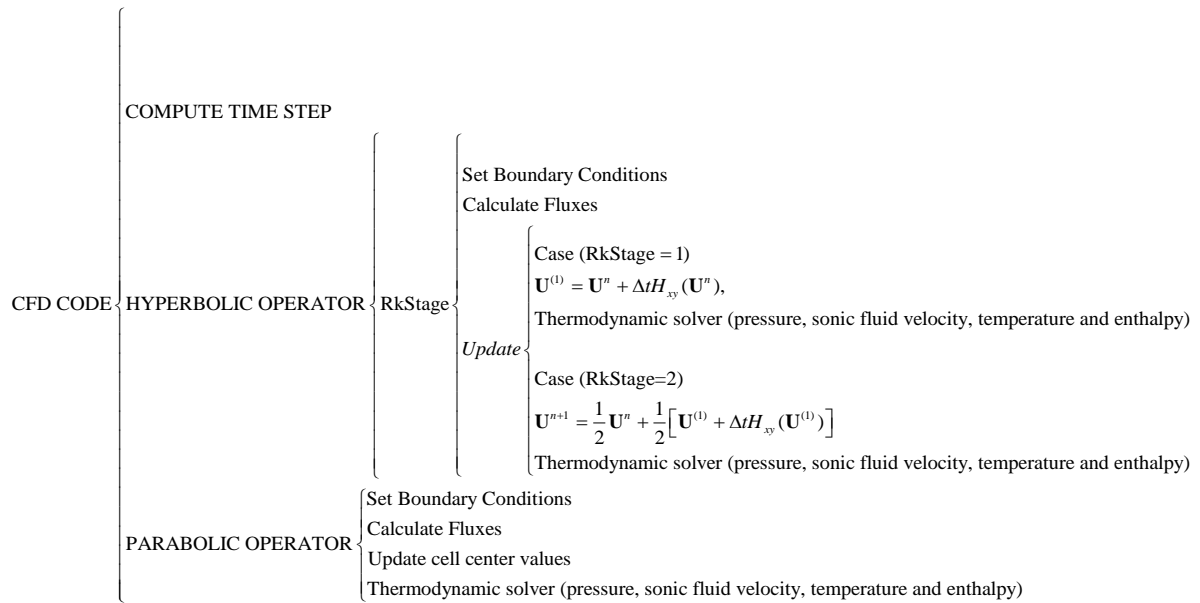


Figure A1: Schematic representation of the CFD code

Thermodynamic solver

The first step is to determine if only one phase exists checking the molar fractions of the components. This filter is employed to decrease the computational time reducing VLE calculations as the Algorithm 1 is quicker than the Algorithm 2. The limits A and B are case dependent.

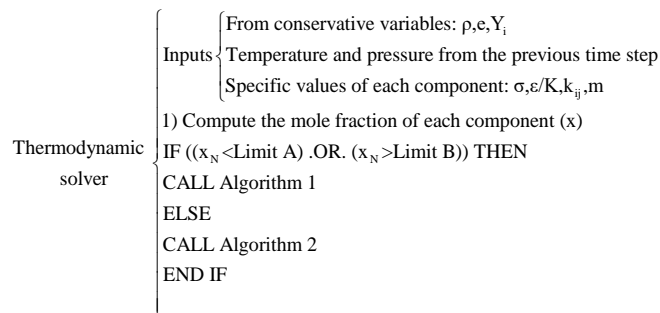


Figure A2: Schematic representation of the thermodynamic solver

Algorithm 1

The molecular density is computed using the density of the mixture. Once the molecular density is known a Newton method is employed to compute the temperature that is needed to calculate the value of all other thermodynamic variables. The temperature dependent function used in the iterative method is the internal energy. Initially a temperature value is assumed (for example the value of the temperature from the previous time RK sub-step or the previous time step) to initialize the iteration process. In most cells, this value is close to the solution.

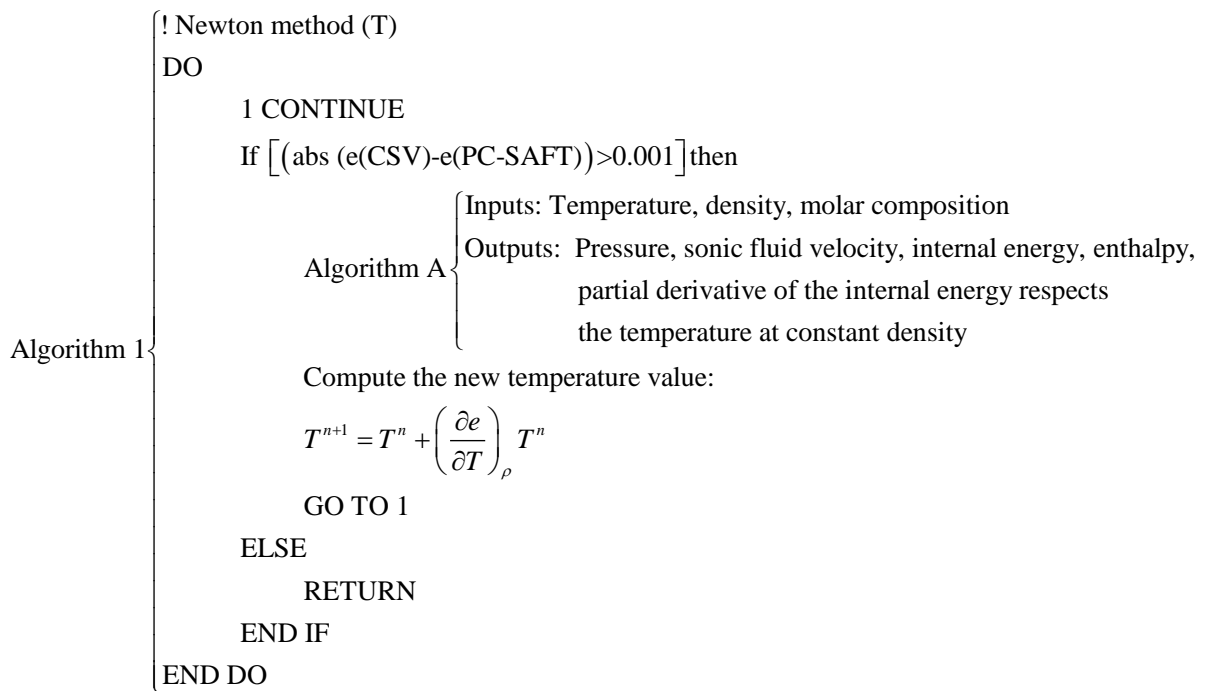


Figure A3: Schematic representation of the Algorithm 1

Algorithm 2

The pressure and the temperature are iterated employing a multidimensional Newton method until the density and the internal energy obtained in the PC-SAFT are the ones obtained from the conservative variables. The initial values of the pressure and the temperature are the ones already stored in the cell that is being solved.

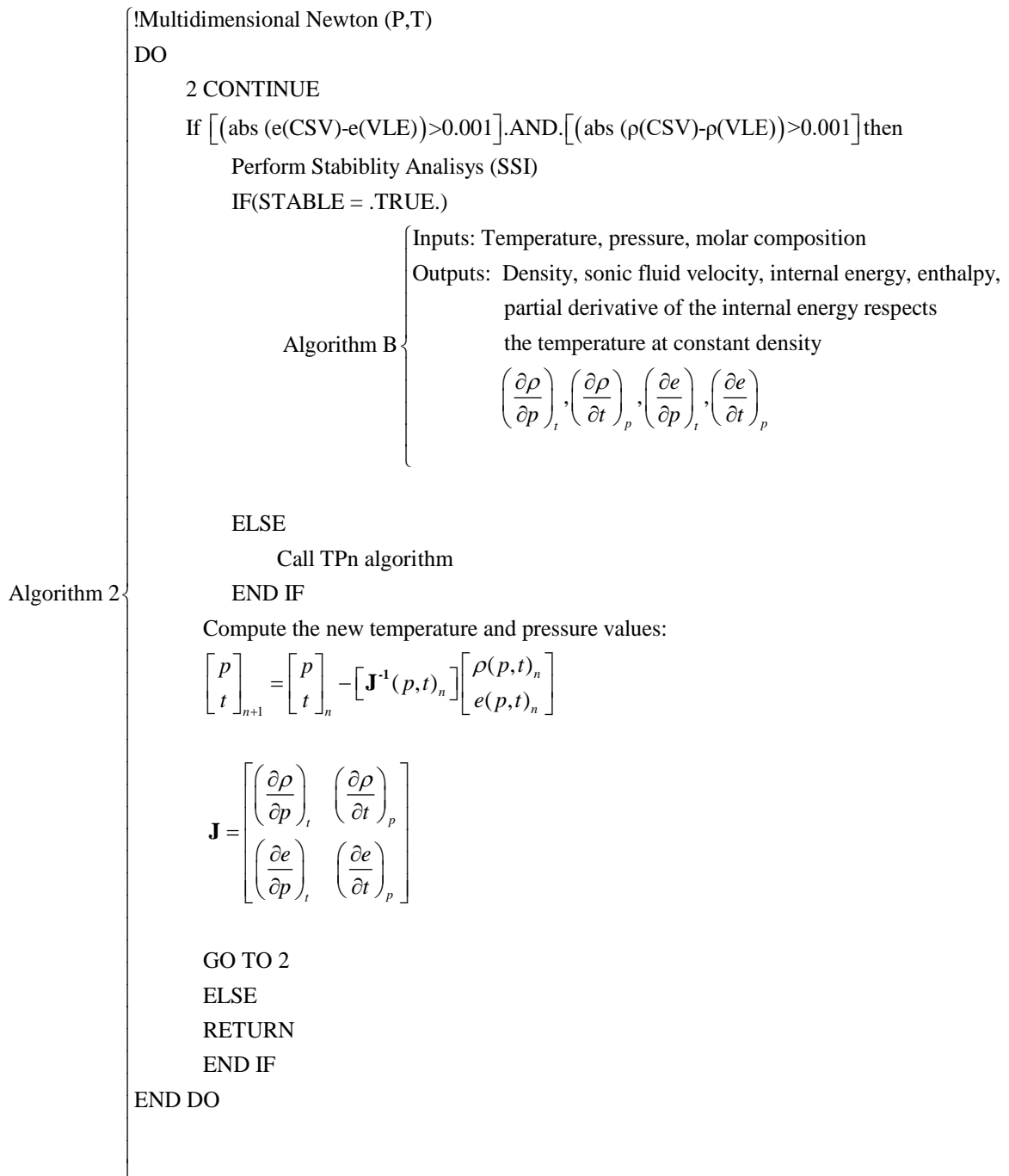


Figure A4: Schematic representation of the Algorithm 2

Algorithm A

Inputs: Temperature, density, molar composition.

Output: Pressure, sonic fluid velocity, internal energy, enthalpy, partial derivative of the internal energy respects the temperature at constant density.

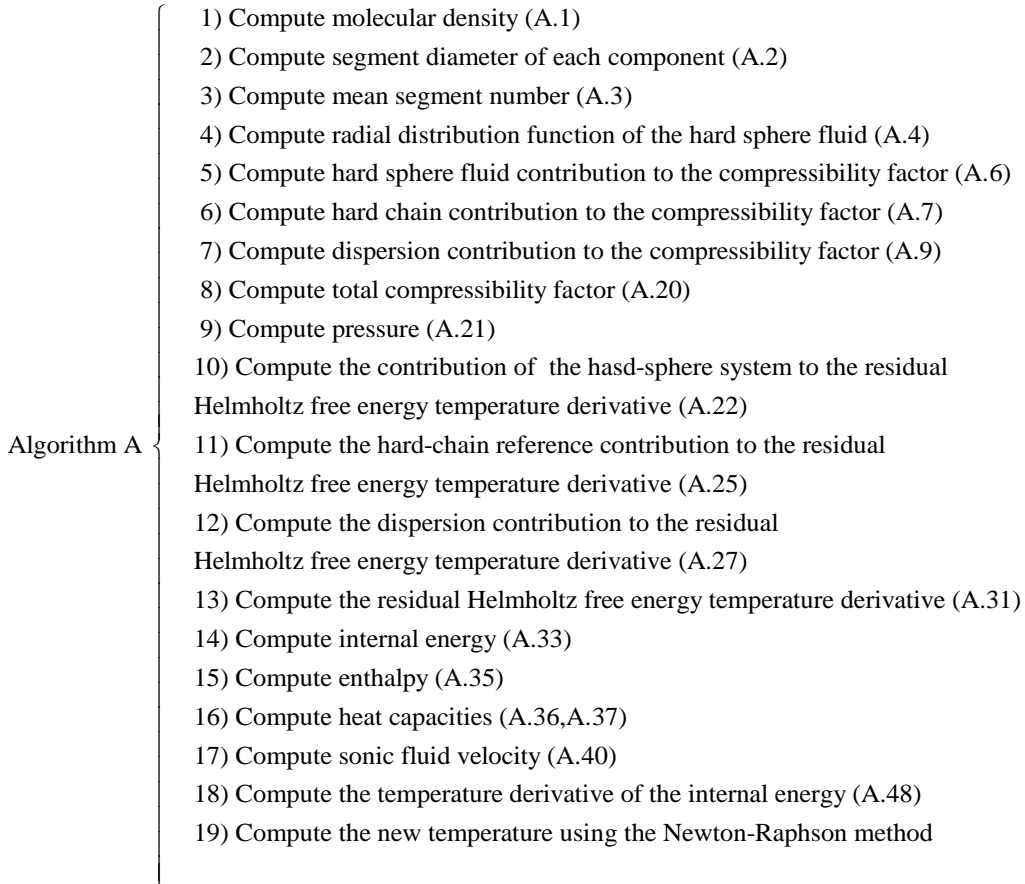


Figure A5: Schematic representation of the Algorithm A

Steps

1) Compute molecular density

$$\rho_m = \rho(kg/m^3) * 10^{-30} * N_A / M_M * 1000 \quad (A.1)$$

where N_A is the Avogadro number and M_M is the molecular weight of the mixture.

2) Compute temperature-dependent segment diameter d of component i [55]

$$d_i = \sigma_{di} \left[1 - 0.12 \exp \left(-3 \frac{\varepsilon_i}{kT} \right) \right] \quad (A.2)$$

where k is the Boltzmann constant, T is the temperature, ε_i is the depth of pair potential of the component and σ_{di} is the segment diameter.

3) Compute mean segment number [55]

$$\bar{m} = \sum_i^{nc} x_i m_i \quad (\text{A.3})$$

where m_i is the number of segments per chain of the component i and x_i is the mole fraction of component i .

4) Compute radial distribution function of the hard-sphere fluid [55]

$$g_{ij}^{hs} = \frac{1}{(1-\zeta_3)} + \left(\frac{d_i d_j}{d_i + d_j} \right) \frac{3\zeta_2}{(1-\zeta_3)^2} + \left(\frac{d_i d_j}{d_i + d_j} \right)^2 \frac{3\zeta_2^2}{(1-\zeta_3)^3} \quad (\text{A.4})$$

where

$$\zeta_n = \frac{\pi}{6} \rho_m \sum_i x_i m_i d_i^n \quad n \in \{0,1,2,3\} \quad (\text{A.5})$$

5) Compute contribution of the hard sphere to the compressibility factor [55]

$$Z^{hs} = \frac{\zeta_3}{(1-\zeta_3)} + \frac{3\zeta_1\zeta_2}{\zeta_0(1-\zeta_3)^2} + \frac{3\zeta_2^3 - \zeta_3\zeta_2^3}{\zeta_0(1-\zeta_3)^3} \quad (\text{A.6})$$

6) Compute hard-chain contribution to the compressibility factor [55]

$$Z^{hc} = \bar{m}Z^{hs} - \sum_i x_i (m_i - 1)(g_{ii}^{hs})^{-1} \rho_m \frac{\partial g_{ii}^{hs}}{\partial \rho_m} \quad (\text{A.7})$$

$$\rho_m \frac{\partial g_{ij}^{hs}}{\partial \rho_m} = \frac{\zeta_3}{(1-\zeta_3)^2} + \left(\frac{d_i d_j}{d_i + d_j} \right) \left(\frac{3\zeta_2}{(1-\zeta_3)^2} + \frac{6\zeta_2\zeta_3}{(1-\zeta_3)^3} \right) + \left(\frac{d_i d_j}{d_i + d_j} \right)^2 \left(\frac{4\zeta_2^2}{(1-\zeta_3)^3} + \frac{6\zeta_2^2\zeta_3}{(1-\zeta_3)^4} \right) \quad (\text{A.8})$$

7) Compute dispersion contribution to the compressibility factor [55]

$$Z^{disp} = -2\pi\rho_m \frac{\partial(\eta I_1)}{\partial \eta} \overline{m^2 \varepsilon \sigma_d^3} - \pi\rho_m \bar{m} \left[C_1 \frac{\partial(\eta I_2)}{\partial \eta} + C_2 \eta I_2 \right] \overline{m^2 \varepsilon^2 \sigma_d^3} \quad (\text{A.9})$$

C_1 and C_2 are defined as:

$$C_1 = \left(1 + Z^{hc} + \rho_m \frac{\partial Z^{hc}}{\partial \rho_m} \right)^{-1} = \left(1 + \bar{m} \frac{8\eta - 8\eta^2}{(1-\eta)^4} + (1 - \bar{m}) \frac{20\eta - 27\eta^2 + 12\eta^3 - 2\eta^4}{[(1-\eta)(2-\eta)]^2} \right)^{-1} \quad (\text{A.10})$$

$$C_2 = \frac{\partial C_1}{\partial \eta} = -C_1^2 \left(\bar{m} \frac{-4\eta^2 + 20\eta + 8}{(1-\eta)^5} + (1 - \bar{m}) \frac{2\eta^3 + 12\eta^2 - 48\eta + 40}{[(1-\eta)(2-\eta)]^3} \right) \quad (\text{A.11})$$

The terms $\overline{m^2 \varepsilon \sigma_d^3}$ and $\overline{m^2 \varepsilon^2 \sigma_d^3}$ are defined as:

$$\overline{m^2 \varepsilon \sigma_d^3} = \sum_i^{nc} \sum_j^{nc} x_i x_j m_i m_j \left(\frac{\varepsilon_{ij}}{kT} \right) \sigma_{d,ij}^3 \quad (\text{A.12})$$

$$\overline{m^2 \varepsilon^2 \sigma_d^3} = \sum_i^{nc} \sum_j^{nc} x_i x_j m_i m_j \left(\frac{\varepsilon_{ij}}{kT} \right)^2 \sigma_{d,ij}^3 \quad (\text{A.13})$$

The mixture parameters σ_{ij} and ε_{ij} , which are defined for every pair of unlike segments, are modelled using a Berthelot-Lorentz combining rule.

$$\sigma_{ij} = \frac{1}{2}(\sigma_i + \sigma_j) \quad (\text{A.14})$$

$$\varepsilon_{ij} = \sqrt{\varepsilon_i \varepsilon_j} (1 - k_{ij}) \quad (\text{A.15})$$

$\frac{\partial(\eta L_1)}{\partial \eta}$ and $\frac{\partial(\eta L_2)}{\partial \eta}$ are expressed as:

$$\frac{\partial(\eta L_1)}{\partial \eta} = \sum_{j=0}^6 a_j (\bar{m})(j+1)\eta^j \quad (\text{A.16})$$

$$\frac{\partial(\eta L_2)}{\partial \eta} = \sum_{j=0}^6 b_j (\bar{m})(j+1)\eta^j \quad (\text{A.17})$$

The coefficients a and b depend on the chain length:

$$a_i(\bar{m}) = a_{0i} + \frac{\bar{m}-1}{\bar{m}} a_{1i} + \frac{\bar{m}-1}{\bar{m}} \frac{\bar{m}-2}{\bar{m}} a_{2i} \quad (\text{A.18})$$

$$b_i(\bar{m}) = b_{0i} + \frac{\bar{m}-1}{\bar{m}} b_{1i} + \frac{\bar{m}-1}{\bar{m}} \frac{\bar{m}-2}{\bar{m}} b_{2i} \quad (\text{A.19})$$

$a_{0i}, a_{1i}, a_{2i}, b_{0i}, b_{1i}, b_{2i}$ are constants [55].

8) Compute compressibility factor [55]

$$Z = 1 + Z^{hc} + Z^{disp} \quad (\text{A.20})$$

9) Compute pressure [55]

$$P = Z k_B T \rho_m (10^{10})^3 \quad (\text{A.21})$$

10) Compute temperature derivative of the Helmholtz free energy residual contribution of the hard-sphere system [55]

$$\left(\frac{\partial \hat{a}^{hs}}{\partial T} \right)_{\rho, x_i} = \frac{1}{\zeta_0} \left[\frac{3(\zeta_{1,T} \zeta_2 + \zeta_1 \zeta_{2,T})}{(1-\zeta_3)} + \frac{3\zeta_1 \zeta_2 \zeta_{3,T}}{(1-\zeta_3)^2} + \frac{3\zeta_2^2 \zeta_{2,T}}{\zeta_3 (1-\zeta_3)^2} + \frac{\zeta_2^3 \zeta_{3,T} (3\zeta_3 - 1)}{\zeta_3^2 (1-\zeta_3)^3} + \left(\frac{3\zeta_2^2 \zeta_{2,T} \zeta_3 - 2\zeta_2^3 \zeta_{3,T}}{\zeta_3^3} \right) \ln(1-\zeta_3) + \left(\zeta_0 - \frac{\zeta_2^3}{\zeta_3^2} \right) \frac{\zeta_{3,T}}{(1-\zeta_3)} \right] \quad (\text{A.22})$$

with abbreviations for two temperature derivatives:

$$\zeta_{n,T} = \frac{\partial \zeta_n}{\partial T} = \frac{\pi}{6} \rho_m \sum_i x_i m_i n d_{i,T} (d_i)^{n-1} \quad n \in \{0,1,2,3\} \quad (\text{A.23})$$

$$d_{i,T} = \frac{\partial d_i}{\partial T} = \sigma_i \left(3 \frac{\varepsilon_i}{kT^2} \right) \left[-0.12 \exp \left(-3 \frac{\varepsilon_i}{kT} \right) \right] \quad (\text{A.24})$$

11) Compute temperature derivative of the Helmholtz free energy hard-chain reference contribution [55]

$$\left(\frac{\partial \tilde{a}^{hc}}{\partial T} \right)_{\rho, x_i} = \bar{m} \left(\frac{\partial \tilde{a}^{hs}}{\partial T} \right)_{\rho, x_i} - \sum_i x_i (m_i - 1) (g_{ii}^{hs})^{-1} \left(\frac{\partial g_{ii}^{hs}}{\partial T} \right)_{\rho, x_i} \quad (\text{A.25})$$

The temperature derivative of the radial pair distribution function is:

$$\begin{aligned} \frac{\partial g_{ii}^{hs}}{\partial T} = & \frac{\zeta_{3,T}}{(1-\zeta_3)^2} + \left(\frac{1}{2} d_{i,T} \right) \frac{\zeta_2}{(1-\zeta_3)^2} + \left(\frac{1}{2} d_i \right) \left(\frac{3\zeta_{2,T}}{(1-\zeta_3)^2} + \frac{6\zeta_2\zeta_{3,T}}{(1-\zeta_3)^3} \right) + \\ & \left(\frac{1}{2} d_i d_{i,T} \right) \frac{2\zeta_2^2}{(1-\zeta_3)^3} + \left(\frac{1}{2} d_i \right)^2 \left(\frac{4\zeta_2\zeta_{2,T}}{(1-\zeta_3)^3} + \frac{6\zeta_2^2\zeta_{3,T}}{(1-\zeta_3)^4} \right) \end{aligned} \quad (\text{A.26})$$

12) Compute temperature derivative of the Helmholtz free energy dispersive attraction [55]

$$\begin{aligned} \left(\frac{\partial \tilde{a}^{disp}}{\partial T} \right)_{\rho, x_i} = & -2\pi\rho_m \left(\frac{\partial I_1}{\partial T} - \frac{I_1}{T} \right) \overline{m^2 \varepsilon \sigma_d^3} - \pi\rho_m \bar{m} \\ & \left[\frac{\partial C_1}{\partial T} I_2 + C_1 \frac{\partial I_2}{\partial T} - 2C_1 \frac{I_2}{T} \right] \overline{m^2 \varepsilon^2 \sigma_d^3} \end{aligned} \quad (\text{A.27})$$

with

$$\frac{\partial I_1}{\partial T} = \sum_{i=0}^6 a_i(\bar{m}) i \zeta_{3,T} \eta^{i-1} \quad (\text{A.28})$$

$$\frac{\partial I_2}{\partial T} = \sum_{i=0}^6 b_i(\bar{m}) i \zeta_{3,T} \eta^{i-1} \quad (\text{A.29})$$

$$\frac{\partial C_1}{\partial T} = \zeta_{3,T} C_2 \quad (\text{A.30})$$

13) Compute temperature derivative of the Helmholtz free energy [55]

$$\left(\frac{\partial \tilde{a}^{res}}{\partial T} \right)_{\rho, x_i} = \left(\frac{\partial \tilde{a}^{hc}}{\partial T} \right)_{\rho, x_i} + \left(\frac{\partial \tilde{a}^{disp}}{\partial T} \right)_{\rho, x_i} \quad (\text{A.31})$$

14) Compute the internal energy [92]

The internal energy is estimated as the sum of the ideal internal energy and the residual internal energy [92].

$$\frac{e^{res}}{RT} = -T \left(\frac{\partial \tilde{a}^{res}}{\partial T} \right)_{\rho, x_i} \quad (\text{A.32})$$

$$e = e^{res} + e^{id} \quad (\text{A.33})$$

15) Compute enthalpy [55]:

It is computed as the sum of the ideal contribution (obtained by integrating the ideal heat capacity at constant pressure with respect to the temperature) and the residual enthalpy [55].

$$\frac{h^{res}}{RT} = -T \left(\frac{\partial \tilde{a}^{res}}{\partial T} \right)_{\rho, x_i} + (Z - 1) \quad (\text{A.34})$$

$$h = h^{res} + h^{id} \quad (\text{A.35})$$

16) Heat capacities [93]

Heat capacities are computed as the sum of the ideal contribution [94] and the correction terms calculated with the PC-SAFT EoS [92]. where C_p and C_v are the heat capacities at constant pressure and volume respectively.

$$C_v = C_{v,id} + C_{v,res} \quad (\text{A.36})$$

$$C_p = C_{p,id} + C_{p,res} \quad (\text{A.37})$$

$$C_v^{res} = -RT \left[2 \left(\frac{\partial \tilde{a}^{res}}{\partial T} \right)_{\rho, x_i} + T \left(\frac{\partial^2 \tilde{a}^{res}}{\partial T^2} \right)_{\rho, x_i} \right] \quad (\text{A.38})$$

$$C_p^{res} = C_v^{res} + R \frac{\left[\rho_m T \left(\frac{\partial^2 \tilde{a}^{res}}{\partial \rho_m \partial T} \right)_{x_i} + \rho_m \left(\frac{\partial \tilde{a}^{res}}{\partial \rho_m} \right)_{T, x_i} + 1 \right]^2}{\left[\rho_m^2 \left(\frac{\partial^2 \tilde{a}^{res}}{\partial \rho_m^2} \right)_{T, x_i} + 2 \rho_m \left(\frac{\partial \tilde{a}^{res}}{\partial \rho_m} \right)_{T, x_i} + 1 \right]} \quad (\text{A.39})$$

17) Speed of sound [93]

The speed of sound is computed as:

$$c = \sqrt{\frac{C_p}{C_v} \left(\frac{\partial P}{\partial \rho_m} \right)_T} \quad (\text{A.40})$$

The derivatives needed to compute the speed of sound are:

$$\left(\frac{\partial P}{\partial \rho_m}\right)_{T,x_i} = \left(\frac{\partial P}{\partial \eta}\right)_{T,x_i} \left(\frac{\partial \eta}{\partial \rho_m}\right)_{T,x_i} \quad (\text{A.41})$$

$$\left(\frac{\partial \eta}{\partial \rho_m}\right)_{T,x_i} = \frac{\pi}{6} (\sum_i x_i m_i d_i^3) \quad (\text{A.42})$$

$$\left(\frac{\partial P}{\partial \eta}\right)_{T,x_i} = k_B T (10^{10})^3 \left[\rho_m \left(\frac{\partial Z}{\partial \eta}\right)_{T,x_i} + Z \left(\frac{\partial \rho_m}{\partial \eta}\right)_{T,x_i} \right] \quad (\text{A.43})$$

$$\left(\frac{\partial \rho_m}{\partial \eta}\right)_{T,x_i} = \frac{6}{\pi} (\sum_i x_i m_i d_i^3)^{-1} \quad (\text{A.44})$$

$$\left(\frac{\partial Z}{\partial \eta}\right)_{T,x_i} \text{ can be found in [95].} \quad (\text{A.45})$$

18) Compute derivative internal energy with respect to temperature at constant density

[93]

$$\left(\frac{\partial e^{res}}{\partial T}\right)_{\rho,x_i} = -RT \left[2 \left(\frac{\partial \tilde{\alpha}^{res}}{\partial T}\right)_{\rho,x_i} + \left(\frac{\partial^2 \tilde{\alpha}^{res}}{\partial T^2}\right)_{\rho,x_i} * T \right] \quad (\text{A.46})$$

$$\frac{de^{id}}{dT} = C_v^{id} \quad (\text{A.47})$$

$$\left(\frac{\partial e}{\partial T}\right)_{\rho,x_i} = \left(\frac{\partial e^{res}}{\partial T}\right)_{\rho,x_i} + \frac{de^{id}}{dT} \quad (\text{A.48})$$

19) Compute the new temperature using the Newton method

Algorithm A(p)

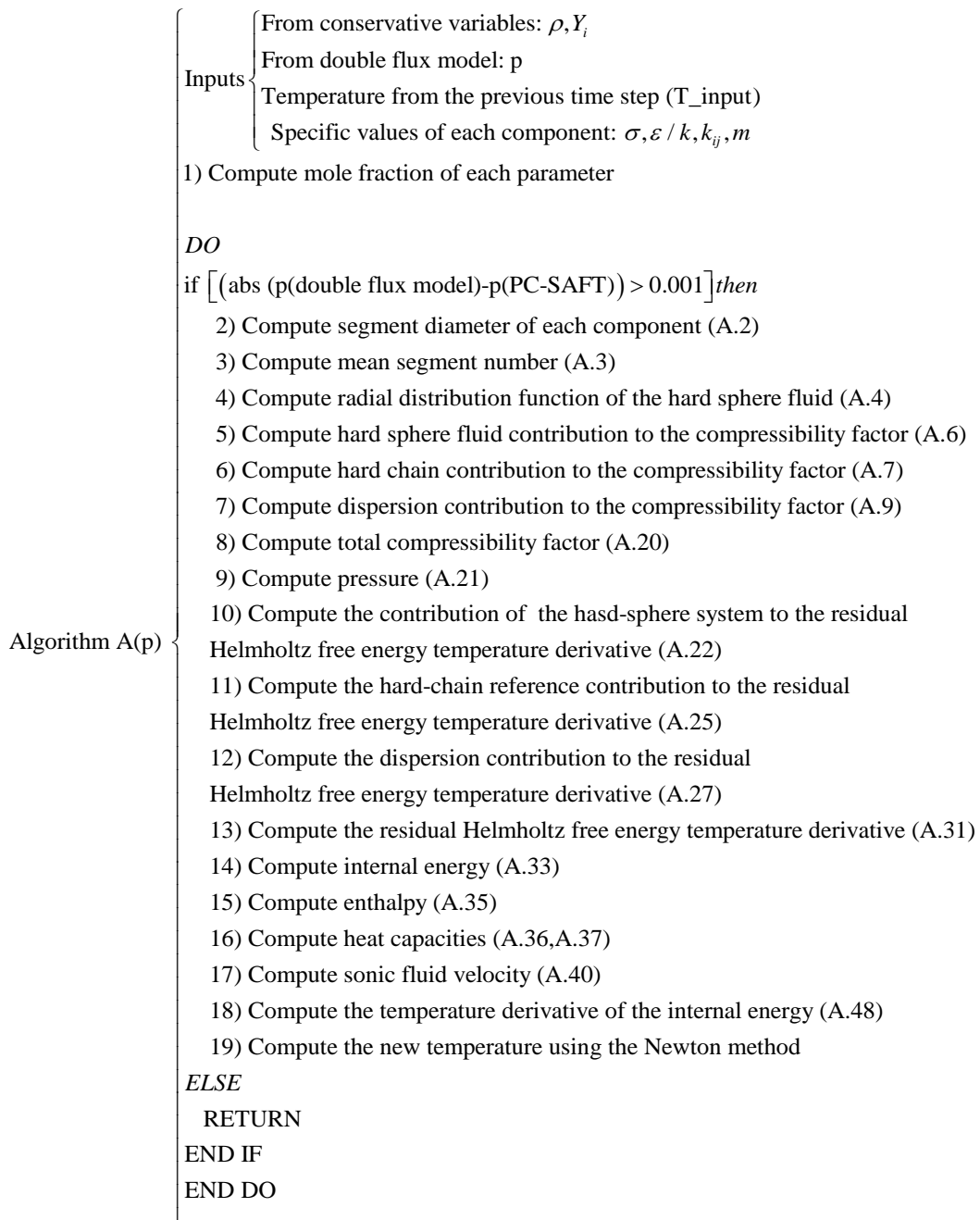


Figure A6: Schematic representation of the Algorithm A(p)

Algorithm B

Inputs: Temperature, pressure, molar composition.

Output: Density, speed of sound, internal energy, enthalpy, fugacities, partial derivative of the internal energy respect the temperature at constant pressure, partial derivative of the internal energy respect the pressure at constant temperature, partial derivative of the density respects the temperature at constant pressure and partial derivative of the density respect the temperature at constant pressure.

This algorithm is applied when the pressure and the temperature are iterated employing a multidimensional Newton method until the density and the internal energy computed are the ones obtained from the conservative variables.

$$\begin{bmatrix} p \\ t \end{bmatrix}_{n+1} = \begin{bmatrix} p \\ t \end{bmatrix}_n - [J^{-1}(p, t)_n] \begin{bmatrix} \rho(p, t)_n \\ e(p, t)_n \end{bmatrix} \quad (\text{A.49})$$

where

$$J = \begin{bmatrix} \left(\frac{\partial \rho}{\partial p}\right)_t & \left(\frac{\partial \rho}{\partial t}\right)_p \\ \left(\frac{\partial e}{\partial p}\right)_t & \left(\frac{\partial e}{\partial t}\right)_p \end{bmatrix} \quad (\text{A.50})$$

The independent variables of the PC-SAFT are the temperature and the density. Thus, it is necessary to perform the following transformations to obtain the partial derivatives needed for the multidimensional Newton method.

$$\left(\frac{\partial \rho}{\partial p}\right)_T = \left(\frac{\partial p}{\partial \rho}\right)_T^{-1} \quad \text{Reciprocity} \quad (\text{A.51})$$

$$\left(\frac{\partial \rho}{\partial t}\right)_p = - \left(\frac{\partial p}{\partial t}\right)_\rho \left(\frac{\partial p}{\partial \rho}\right)_T^{-1} \quad \text{Chain rule} \quad (\text{A.52})$$

$$\left(\frac{\partial e}{\partial p}\right)_T = \left(\frac{\partial e}{\partial \rho}\right)_T \left(\frac{\partial p}{\partial \rho}\right)_T^{-1} \quad \text{Chain rule} \quad (\text{A.53})$$

$$\left(\frac{\partial e}{\partial t}\right)_p = \left(\frac{\partial e}{\partial t}\right)_\rho - \left(\frac{\partial e}{\partial \rho}\right)_T \left(\frac{\partial \rho}{\partial t}\right)_p \left(\frac{\partial p}{\partial \rho}\right)_T^{-1} \quad \text{Triple product rule} \quad (\text{A.54})$$

The partial derivatives needed then are:

$$\left(\frac{\partial p}{\partial t}\right)_\rho, \left(\frac{\partial p}{\partial \rho}\right)_T, \left(\frac{\partial e}{\partial \rho}\right)_T, \left(\frac{\partial e}{\partial t}\right)_\rho$$

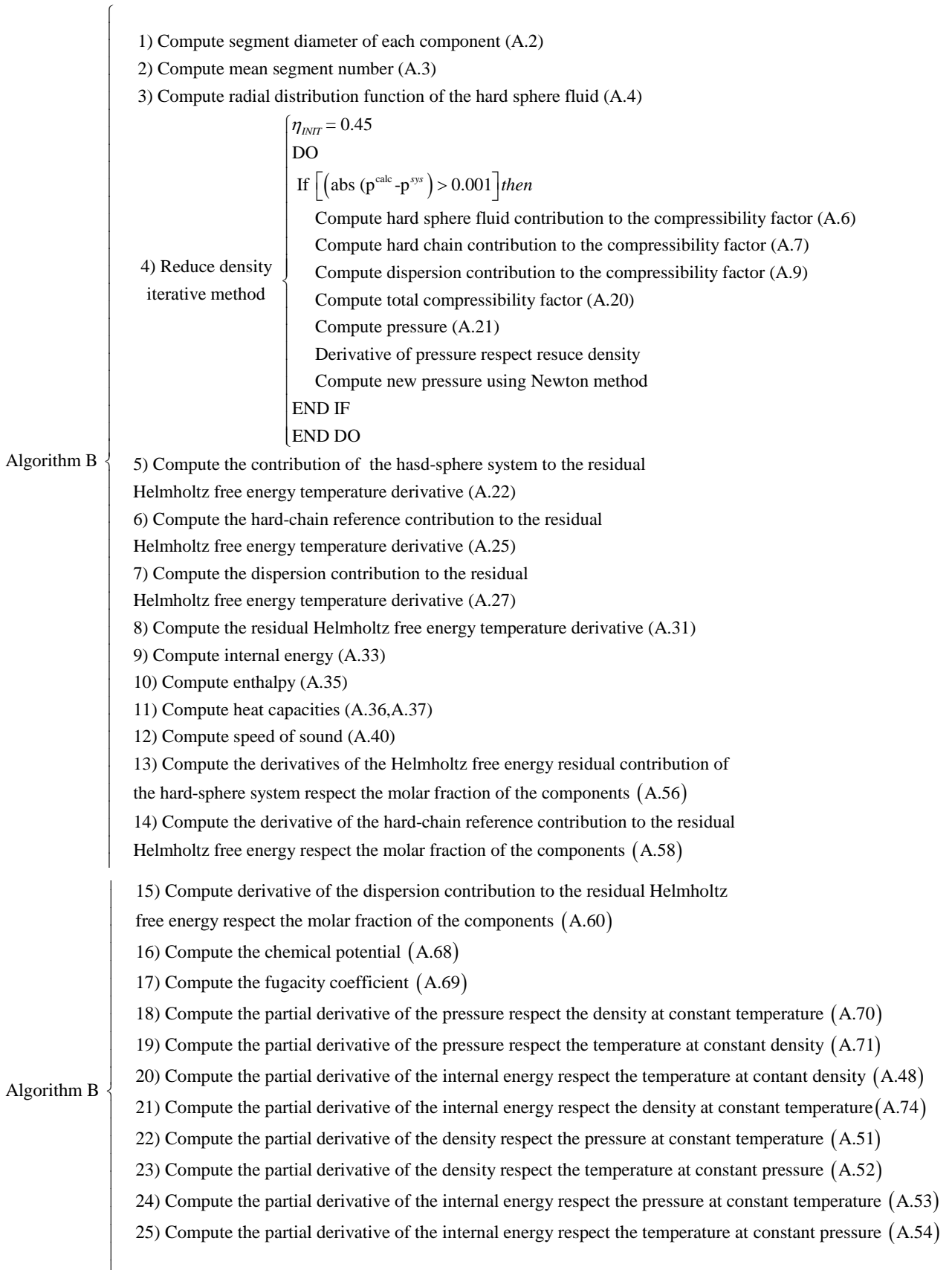


Figure A7: Schematic representation of the Algorithm B

Steps

- 1) Compute temperature-dependent segment diameter d of component i (A.2)
- 2) Compute mean segment number (A.3)
- 3) Compute radial distribution function of the hard-sphere fluid (A.4)
- 4) Reduce density iterative method
 - a. $\eta_{INIT} = 0.45$
 - b. Compute contribution of the hard sphere to the compressibility factor (A.6)
 - c. Compute hard-chain contribution to the compressibility factor (A.7)
 - d. Compute dispersion contribution to the compressibility factor (A.9)
 - e. Compute compressibility factor (A.20)
 - f. Compute pressure (A.21)
 - g. Derivative of pressure respect reduce density

$$\left(\frac{\partial P}{\partial \eta}\right) = \left[\rho_m \left(\frac{\partial Z}{\partial \eta}\right) + Z \left(\frac{\partial \rho_m}{\partial \eta}\right)\right] (10^{10})^3 Z k_B T \quad (\text{A.55})$$
 - h. Compute the new pressure using the Newton method
- 5) Compute temperature derivative of the Helmholtz free energy residual contribution of the hard-sphere system (A.22)
- 6) Compute temperature derivative of the hard-chain reference contribution to the residual Helmholtz free energy (A.25)
- 7) Compute temperature derivative of the dispersion contribution to the residual Helmholtz free energy (A.27)
- 8) Compute temperature derivative of the Helmholtz free energy (A.31)
- 9) Compute the internal energy (A.33)
- 10) Compute enthalpy (A.35)
- 11) Compute heat capacities (A.36,37)
- 12) Compute speed of sound (A.40)
- 13) Compute the derivatives of the Helmholtz free energy residual contribution of the hard-sphere system respect the molar fraction of the components (A.56)

$$\begin{aligned} \left(\frac{\partial \tilde{a}^{hs}}{\partial x_k}\right)_{T,\rho,x_{j \neq k}} &= -\frac{\zeta_{0,xk}}{\zeta_0} \tilde{a}^{hs} + \frac{1}{\zeta_0} \left[\frac{3(\zeta_{1,xk}\zeta_2 + \zeta_1\zeta_{2,xk})}{(1-\zeta_3)} + \frac{3\zeta_1\zeta_2\zeta_{3,xk}}{(1-\zeta_3)^2} + \frac{3\zeta_2^2\zeta_{2,xk}}{\zeta_3(1-\zeta_3)^2} + \right. \\ &\left. \frac{\zeta_2^3\zeta_{3,xk}(3\zeta_3-1)}{\zeta_3^2(1-\zeta_3)^3} + \left(\frac{3\zeta_2^2\zeta_{2,xk}\zeta_3 - 2\zeta_2^3\zeta_{3,xk}}{\zeta_3^3} - \zeta_{0,xk}\right) \ln(1-\zeta_3) + \left(\zeta_0 - \frac{\zeta_2^3}{\zeta_3^2}\right) \frac{\zeta_{3,xk}}{(1-\zeta_3)} \right] \end{aligned} \quad (\text{A.56})$$

where

$$\zeta_{n,xk} = \left(\frac{\partial \zeta_n}{\partial x_k} \right)_{T,\rho,x_{j \neq k}} = \frac{\pi}{6} \rho_m m_k (d_k)^n \quad (\text{A.57})$$

14) Compute the derivative of the hard-chain reference contribution to the residual Helmholtz free energy respect the molar fraction of the components (A.58)

$$\begin{aligned} \left(\frac{\partial \tilde{a}^{hc}}{\partial x_k} \right)_{T,\rho,x_{j \neq k}} &= m_k \tilde{a}^{hs} + \bar{m} \left(\frac{\partial \tilde{a}^{hs}}{\partial x_k} \right)_{T,\rho,x_{j \neq k}} - \sum_i x_i (m_i - 1) (g_{ii}^{hs})^{-1} \left(\frac{\partial g_{ii}^{hs}}{\partial x_k} \right)_{T,\rho,x_{j \neq k}} \\ &\quad - (m_k - 1) \ln(g_{kk}^{hs}) \end{aligned} \quad (\text{A.58})$$

where

$$\begin{aligned} \left(\frac{\partial g_{ij}^{hs}}{\partial x_k} \right)_{T,\rho,x_{j \neq k}} &= \frac{\zeta_{3,xk}}{(1-\zeta_3)^2} + \left(\frac{d_i d_j}{d_i + d_j} \right) \left(\frac{3\zeta_{2,xk}}{(1-\zeta_3)^2} + \frac{6\zeta_2 \zeta_{3,xk}}{(1-\zeta_3)^3} \right) + \\ &\left(\frac{d_i d_j}{d_i + d_j} \right)^2 \left(\frac{4\zeta_2 \zeta_{2,xk}}{(1-\zeta_3)^3} + \frac{6\zeta_2^2 \zeta_{3,xk}}{(1-\zeta_3)^4} \right) \end{aligned} \quad (\text{A.59})$$

15) Compute derivative of the dispersion contribution to the residual Helmholtz free energy respect the molar fraction of the components (A.60)

$$\begin{aligned} \left(\frac{\partial \tilde{a}^{disp}}{\partial x_k} \right)_{T,\rho,x_{j \neq k}} &= -2\pi\rho_m \left[I_{1,xk} \overline{m^2 \varepsilon \sigma^3} + I_1 \overline{(m^2 \varepsilon \sigma^3)}_{xk} \right] - \\ &\pi\rho \left\{ [m_k C_1 I_2 + \bar{m} C_{1,xk} I_2 + \bar{m} C_1 I_{2,xk}] \overline{m^2 \varepsilon \sigma^3} + \right. \\ &\left. \bar{m} C_1 I_2 \overline{(m^2 \varepsilon \sigma^3)}_{xk} \right\} \end{aligned} \quad (\text{A.60})$$

where

$$\overline{(m^2 \varepsilon \sigma^3)}_{xk} = 2m_k \sum_j x_j m_j \left(\frac{\varepsilon_{kj}}{kT} \right) \sigma_{kj}^3 \quad (\text{A.61})$$

$$\overline{(m^2 \varepsilon^2 \sigma^3)}_{xk} = 2m_k \sum_j x_j m_j \left(\frac{\varepsilon_{kj}}{kT} \right)^2 \sigma_{kj}^3 \quad (\text{A.62})$$

$$C_{1,xk} = C_2 \zeta_{3,xk} - C_1^2 \left[m_k \frac{8\eta - 2\eta^2}{(1-\eta)^4} - m_k \frac{20\eta - 27\eta^2 + 12\eta^3 - 2\eta^4}{[(1-\eta)(2-\eta)]^2} \right] \quad (\text{A.63})$$

$$I_{1,xk} = \sum_{i=0}^6 [a_i(\bar{m}) i \zeta_{3,xk} \eta^{i-1} + a_{i,xk} \eta^i] \quad (\text{A.64})$$

$$I_{2,xk} = \sum_{i=0}^6 [b_i(\bar{m}) i \zeta_{3,xk} \eta^{i-1} + b_{i,xk} \eta^i] \quad (\text{A.65})$$

$$a_{i,xk} = \frac{m_k}{\bar{m}^2} a_{1i} + \frac{m_k}{\bar{m}^2} \left(3 - \frac{4}{\bar{m}}\right) a_{2i} \quad (\text{A.66})$$

$$b_{i,xk} = \frac{m_k}{\bar{m}^2} b_{1i} + \frac{m_k}{\bar{m}^2} \left(3 - \frac{4}{\bar{m}}\right) b_{2i} \quad (\text{A.67})$$

16) Compute the chemical potential (A.68):

$$\frac{\mu_k^{res}(T,v)}{kT} = \tilde{a}^{res} + (Z - 1) + \left(\frac{\partial \tilde{a}^{res}}{\partial x_k}\right)_{T,v,x_{i \neq j}} - \sum_{j=1}^N \left[x_j \left(\frac{\partial \tilde{a}^{res}}{\partial x_j}\right)_{T,v,x_{i \neq j}} \right] \quad (\text{A.68})$$

17) Compute the fugacity coefficient (A.69):

$$\ln \varphi_k = \frac{\mu_k^{res}(T,v)}{kT} - \ln Z \quad (\text{A.69})$$

18) Compute the partial derivative of the pressure with respect to the density at constant density.

$$\left(\frac{\partial P}{\partial \rho_m}\right)_T = k_B T (10^{10})^3 \left[\left(\frac{\partial Z}{\partial \rho_m}\right)_t \rho_m + Z \right] \quad (\text{A.70})$$

19) Compute the partial derivative of the pressure respect the temperature at constant density.

$$\left(\frac{\partial P}{\partial T}\right)_\rho = k_B (10^{10})^3 \rho_m \left[\left(\frac{\partial Z}{\partial T}\right)_\rho T + Z \right] \quad (\text{A.71})$$

20) Compute the partial derivative of the internal energy respect the temperature at constant density. (A.48)

21) Compute the partial derivative of the internal energy respect the density at constant temperature.

$$\left(\frac{\partial e^{res}}{\partial \rho_m}\right)_T = -RT^2 \left(\frac{\partial \tilde{a}^{res}}{\partial T \partial \rho_m}\right)_T \quad (\text{A.72})$$

$$\frac{de^{id}}{d\rho_m} = 0.0 \quad (\text{A.73})$$

$$\left(\frac{\partial e}{\partial T}\right)_{\rho, x_i} = \left(\frac{\partial e^{res}}{\partial T}\right)_{\rho, x_i} \quad (\text{A.74})$$

- 22) Compute the partial derivative of the density respect the pressure at constant temperature (A.51)
- 23) Compute the partial derivative of the density respect the temperature at constant pressure (A.52)
- 24) Compute the partial derivative of the internal energy respect the pressure at constant temperature (A.53)
- 25) Compute the partial derivative of the internal energy respect the temperature at constant pressure (A.54)

Stability

The Successive Substitution Iteration (SSI) algorithm ([21], [96]) (without the Newton method) has been employed to determine if the mixture is stable.

```

1) IF (T > Tc FUEL) THEN
    STABLE=1
    RETURN
END IF
2) IF [ (XN2 > C).AND.(XN2 < D) ] THEN
    STABLE=0
    RETURN
END IF
3) Call Algorithm B (obtain fugacity values)
    Inputs: Temperature, pressure, molar composition of the mixture
4) Calculate di(z) (A.75)
5) Wilson's correlation is used to initialize the K-values (A.76)
6) Calculate Y_init (A.77-A.78)
7) DO k=1,ntrial    ! SSI ALGORITHM
    {
        Yi = Y_init(k,i)
        DO j=1,nmax
            {
                IF (||dY|| > εSSI) THEN
                    y_triali = Yi/sum(Y)
                    Call Algorithm B
                    {
                        Inputs: Temperature, pressure, molar composition y_trial
                        Obtain fugacity values (ln φi)
                    }
                    Yn(i) = exp[di(z) - ln φi]
                    dYi = Yni - Yi
                    Yi = Yni
                ELSE
                    TPD*(k) = 1. - sum(Y)
                    GO TO 1
                END IF
            }
        END DO
    }
    END DO
1 CONTINUE
IF (min(TPD*(k)) < -10-8)
    STABLE = FALSE
ELSE
    STABLE = TRUE
END IF
END DO

```

Stability {

Figure A8: Schematic representation of the stability algorithm

Steps

1) The mixture is stable if the temperature is higher than T_c of the fuel (STABLE = 1)

Any mixture with a temperature higher than the critical temperature of the fuel will be in a supercritical state (STABLE = 1). This kind of filters are applied to reduce the computational time.

2) The mixture is unstable if the nitrogen molar fraction is bigger than C and lower than D (STABLE = 0)

For example, by performing an injection of n-dodecane at 363K in a combustion chamber at 973K, the nitrogen mole fraction at which the fuel starts vaporizing depends on the pressure in the combustion chamber. Considering Diesel engine high-load operation conditions and an isobaric scenario it would be safe to consider that any mixture with a nitrogen molar fraction bigger than 0.35 and lower 0.7 will be in a VLE state.

3) Call Algorithm B to obtain fugacity coefficients $\ln\phi_i(z_i)$

Inputs: Temperature, pressure, molar composition of the mixture

4) Calculate $d_i(z)$

$$d_i(z) = \ln\phi_i(z_i) + \ln z_i \quad (\text{A.75})$$

5) The Wilson's correlation is used to initialize the K-values

$$K_i = \frac{p_{ci}}{p} \exp \left[5.37(1.0 + w_i) \left(1.0 - \frac{T_{ci}}{T} \right) \right] \quad (\text{A.76})$$

being

$$K_i = \frac{x_i}{y_i}$$

where p_{ci} is the critical pressure of the component i, T_{ci} is the critical temperature of the component i, w_i is the acentric factor of the component i.

6) Calculate trial phases Y (two trials)

For the trial 1:

$$Y(1, comp) = \begin{cases} \frac{z_i}{K_i} & \text{(Liquid phase)} \\ z_i K_I & \text{(Vapor phase)} \end{cases} \quad (\text{A.77})$$

For the trial 2:

$$Y(2, comp) = \begin{cases} \frac{z_i}{K_i^3} & \text{(Liquid phase)} \\ \frac{z_i K_I}{3} & \text{(Vapor phase)} \end{cases} \quad (\text{A.78})$$

7) SSI-Algorithm (Figure A8)

TPn Algorithm

A successive substitution method is employed to perform equilibrium calculations at specified temperature, pressure and overall composition.

```

1) Wilson's correlation is used to initialize the K-values (A.76)
2) WHILE (eps(TPN)<10-7) THEN
  !Rachford-Rice
  a) If the conditions A.79-A.80 are met:
    βmin = 0, βmax = 1
    If Ki > 1 change βmin and βmax (A.81-A.82)
    Calculate βmi (A.83)
    Change βmin and βmax (A.84)
    WHILE (eps(Rachford-Rice) > 10-7) THEN
      Calculate g(β), g'(β) (A.85-A.86)
      Change limits βmin and βmax (A.87)
      Newton-Raphson (A.88)
      Calculate eps = abs((βnew - β) / β)
      New overall fraction of vapor phase (A.90-A.91)
      Calculate liquid and vapour mole fractions (A.92-A.93)
    b) If the conditions A.79-A.80 are not met:
      Calculate liquid and vapour mole fractions (A.94-A.95)
    c) Call Algorithm B to obtain fugacity coefficients of the liquid and vapor phase
    d) Objective function (A.96)
    e) Calculate eps(TPN)
    f) Update K-factors from fugacity coefficients (A.97)
END
  
```

Figure A9: Schematic representation of the TPn algorithm

1) The Wilson's correlation is used to initialize the K-values (A.76)

2) WHILE (eps(TPN)<10⁻⁷) THEN

Solve Rachford-Rice

a. Check conditions A.79-A.80 to know if there is a solution in the interval

$\beta \in [0, 1]$. If the conditions are met $\beta_{min} = 0, \beta_{max} = 1$. If not, go to step 2.b.

$$\sum_{i=1}^C z_i K_i - 1 > 0 \quad (A.79)$$

$$1 - \sum_{i=1}^C \frac{z_i}{K_i} < 0 \quad (A.80)$$

• If $K_i > 1$ then

$$\beta_{min} = \max_i \left[0, \frac{K_i z_i - 1}{K_i - 1} \right] \quad (A.81)$$

$$\beta_{\max} = \min_i \left[1, \frac{1-z_i}{1-K_i} \right] \quad (\text{A.82})$$

- Calculate $\beta_{ini} = 0.5(\beta_{min} + \beta_{max})$ (A.83)

- **Change limits**

$$g(\beta_{ini}) > 0 \rightarrow \beta_{\min} = \beta_{ini},$$

$$g(\beta_{ini}) < 0 \rightarrow \beta_{\max} = \beta_{ini} \quad (\text{A.84})$$

- **WHILE (eps(Rachford-Rice) > 10⁻⁷) then**

- Calculate $g(\beta)$, $g'(\beta)$

$$g(\beta) = \sum_{i=1}^C (y_i - x_i) = \sum_{i=1}^C \frac{z_i(K_i-1)}{1-\beta+\beta K_i} = 0 \quad (\text{A.85})$$

$$g'(\beta) = -\sum_{i=1}^C \frac{z_i(K_i-1)^2}{(1-\beta+\beta K_i)^2} < 0 \quad (\text{A.86})$$

- **Change limits**

$$g > 0 \rightarrow \beta_{\min} = \beta,$$

$$g < 0 \rightarrow \beta_{\max} = \beta \quad (\text{A.87})$$

- **Newton-Raphson**

$$\Delta\beta = -\frac{g(\beta)}{dg/d\beta}$$

$$\beta_{new} = \beta + \Delta\beta \quad (\text{A.88})$$

- **Calculate eps**

$$eps = abs((\beta_{new} - \beta)/\beta) \quad (\text{A.89})$$

- **New overall fraction of vapor phase:**

$$\beta = \beta_{new} \text{ if } \beta_{new} \text{ is inside the interval } [\beta_{\min}, \beta_{\max}] \quad (\text{A.90})$$

- **If it is not, it is calculated as:**

$$\beta = 0.5(\beta_{\min} + \beta_{\max}), \beta_{\min} < \beta_{\text{new}} < \beta_{\max} \quad (\text{A.91})$$

- Calculate liquid and vapour mole fractions

$$x_i = \frac{z_i}{1 - \beta + \beta K_i} \quad (\text{A.92})$$

$$y_i = \frac{K_i z_i}{1 - \beta + \beta K_i} \quad (\text{A.93})$$

- b. If the conditions A.79-A.80 are not met [97]:

If $\sum z_i / K_i \leq 1$ the liquid and vapour mole fractions are computed as:

$$\beta = 1$$

$$x_i = z_i / K_i$$

$$y_i = z_i \quad (\text{A.94})$$

Normalization of x_i

If $\sum z_i K_i \leq 1$ the liquid and vapour mole fractions are computed as:

$$\beta = 0$$

$$x_i = z_i$$

$$y_i = z_i * K_i \quad (\text{A.95})$$

Normalization of y_i

- c. Call Algorithm B to obtain fugacity coefficients of the liquid and vapor phase

Inputs: Temperature, pressure, molar composition of the liquid or vapor

- d. Objective function

$$F_i = \ln \varphi_v(T, p, y) - \ln \varphi_l(T, p, x) + \ln K_i = 0 \quad (\text{A.96})$$

- e. Calculate eps(TPN)

- f. Update K-factors from fugacity coefficients

$$K_i = \exp(\ln \varphi_l(T, p, x) - \ln \varphi_v(T, p, y)) \quad (\text{A.97})$$

END

VLE properties

The partial derivatives needed to perform the multidimensional Newton iteration in T and p are obtained numerically.

The phase fraction on mass (β_m) basis is computed as:

$$\beta_m = \beta \frac{M_V(\text{mixture molar mass in liquid phase})}{M_T(\text{mixture molar mass})} \quad (\text{A.98})$$

The equilibrium volume (v_{EQ}) is computed as:

$$v_{EQ} = \beta_m v_v + (1 - \beta_m) v_l \quad (\text{A.99})$$

The equilibrium density is computed as:

$$\rho = \frac{1}{v_{EQ}} \quad (\text{A.100})$$

The equilibrium internal energy is computed as:

$$e = \beta_m e_v + (1 - \beta_m) e_l \quad (\text{A.101})$$

The equilibrium enthalpy is computed as:

$$h = \beta_m h_v + (1 - \beta_m) h_l \quad (\text{A.102})$$

The speed of sound in the VLE state was computed using Wallis formula:

$$\frac{1}{\rho c_{\text{Wallis}}^2} = \frac{\theta}{\rho_v c_v^2} + \frac{1-\theta}{\rho_l c_l^2} \quad (\text{A.103})$$

where the vapour volume fraction (θ) is computed as:

$$\theta = \frac{\rho - \rho_v}{\rho_v - \rho_l} \quad (\text{A.104})$$

Publications

Journal publications (newest fist)

Rodriguez, C., Rokni, H. B., Koukouvinis, P., Gupta, A., & Gavaises, M. (2019). Complex multicomponent real-fluid thermodynamic model for high-pressure Diesel fuel injection. Fuel. Accepted manuscript.

Rodriguez, C., Koukouvinis, P., & Gavaises, M. (2019). Simulation of supercritical diesel jets using the PC-SAFT EoS. The Journal of Supercritical Fluids, 145, 48–65. <https://doi.org/10.1016/j.supflu.2018.11.003>

Rodriguez, C., Vidal, A., Koukouvinis, P., Gavaises, M., & McHugh, M. A. (2018). Simulation of transcritical fluid jets using the PC-SAFT EoS. Journal of Computational Physics, 374, 444–468. <https://doi.org/10.1016/j.jcp.2018.07.030>

Vidal, A., **Rodriguez, C.,** Koukouvinis, P., Gavaises, M., & Mchugh, M. A. (n.d.). Modelling of Diesel fuel properties through its surrogates using Perturbed-Chain, Statistical Associating Fluid Theory. <https://doi.org/10.1177/1468087418801712>

Conference publications (newest fist)

C. Rodriguez, Houman B. Rokni, P. Koukouvinis, Ashutosh Gupta, M. Gavaises, “CFD simulation of pseudo-diesel injections at high-load conditions employing the PC-SAFT EoS and VLE calculations”, to be presented in ILASS-Europe, Sept 2019

C. Rodriguez, P. Koukouvinis, M. Gavaises, “Supercritical, transcritical and subcritical real-fluid mixing using the PC-SAFT EOS”, ENCOM 2019, Germany, April 2019

C. Rodriguez, A. Vidal, P. Koukouvinis, M. Gavaises, “Simulation of transcritical Diesel jets using the PC-SAFT EoS”, ICLASS, Chicago, IL, USA, July 22-26, 2018

A. Vidal, **C. Rodriguez,** P. Koukouvinis, M. Gavaises, ‘Effect of realistic multicomponent diesel surrogates on predicted in-nozzle flow and cavitation’, ICLASS, Chicago, IL, USA, July 22-26, 2018

C. Rodriguez, A. Vidal, P. Koukouvinis, and M. Gavaises, “Supercritical and transcritical real-fluid mixing using the PC-SAFT EOS”, in Proceedings ILASS–Europe 2017. 28th Conference on Liquid Atomization and Spray Systems, 2017.

References

- [1] E. Dons *et al.*, “Impact of time–activity patterns on personal exposure to black carbon,” *Atmos. Environ.*, vol. 45, no. 21, pp. 3594–3602, Jul. 2011.
- [2] J. E. Hansen, “A brighter future,” *Clim. Change*, vol. 52, no. 4, pp. 435–440, 2002.
- [3] E. Çabukoglu, G. Georges, L. Küng, G. Pareschi, and K. Boulouchos, “Battery electric propulsion: An option for heavy-duty vehicles? Results from a Swiss case-study,” *Transp. Res. Part C Emerg. Technol.*, vol. 88, pp. 107–123, Mar. 2018.
- [4] I. T. F. (International T. Forum), “ITF Transport Outlook 2017.” OECD Publishing Paris, 2017.
- [5] W. O. H. Mayer *et al.*, “Atomization and Breakup of Cryogenic Propellants Under High-Pressure Subcritical and Supercritical Conditions,” *J. Propuls. Power*, vol. 14, no. 5, pp. 835–842, Sep. 1998.
- [6] M. OSCHWALD* *et al.*, “INJECTION OF FLUIDS INTO SUPERCRITICAL ENVIRONMENTS,” *Combust. Sci. Technol.*, vol. 178, no. 1–3, pp. 49–100, Jan. 2006.
- [7] C. Segal and S. A. Polikhov, “Subcritical to supercritical mixing,” *Phys. Fluids*, vol. 20, no. 5, p. 052101, May 2008.
- [8] R. R. Rachedi, L. C. Crook, and P. E. Sojka, “An Experimental Study of Swirling Supercritical Hydrocarbon Fuel Jets,” *J. Eng. Gas Turbines Power*, vol. 132, no. 8, p. 081502, 2010.
- [9] B. Chehroudi, “Recent Experimental Efforts on High-Pressure Supercritical Injection for Liquid Rockets and Their Implications,” *Int. J. Aerosp. Eng.*, vol. 2012, pp. 1–31, 2012.
- [10] R. N. Dahms, J. Manin, L. M. Pickett, and J. C. Oefelein, “Understanding high-pressure gas-liquid interface phenomena in Diesel engines,” *Proc. Combust. Inst.*, vol. 34, no. 1, pp. 1667–1675, Jan. 2013.
- [11] R. N. Dahms and J. C. Oefelein, “On the transition between two-phase and single-phase interface dynamics in multicomponent fluids at supercritical pressures,” *Phys. Fluids*, vol. 25, no. 9, p. 092103, Sep. 2013.
- [12] J. Manin, M. Bardi, L. M. Pickett, R. N. Dahms, and J. C. Oefelein, “Microscopic investigation of the atomization and mixing processes of diesel sprays injected into high pressure and temperature environments,” *Fuel*, vol. 134, pp. 531–543, Oct. 2014.
- [13] L. Pickett and G. Bruneaux, “Engine combustion network. Combustion Research Facility, Sandia National Laboratories, Livermore, CA,” See <http://www.sandia.gov/ECN>, 2011.
- [14] C. Crua, J. Manin, and L. M. Pickett, “On the transcritical mixing of fuels at diesel engine conditions,” *Fuel*, vol. 208, pp. 535–548, 2017.

- [15] G. Mo and L. Qiao, "A molecular dynamics investigation of n-alkanes vaporizing into nitrogen: transition from subcritical to supercritical," *Combust. Flame*, vol. 176, pp. 60–71, 2017.
- [16] M. Jangi, R. Solsjo, B. Johansson, and X. Bai, "International Journal of Heat and Fluid Flow On large eddy simulation of diesel spray for internal combustion engines," *Int. J. HEAT FLUID FLOW*, vol. 53, pp. 68–80, 2015.
- [17] Y. Pei, E. R. Hawkes, S. Kook, G. M. Goldin, and T. Lu, "Modelling n-dodecane spray and combustion with the transported probability density function method," *Combust. Flame*, vol. 162, no. 5, pp. 2006–2019, May 2015.
- [18] Y. Pei *et al.*, "Large eddy simulation of a reacting spray flame with multiple realizations under compression ignition engine conditions," *Combust. Flame*, vol. 162, no. 12, pp. 4442–4455, Dec. 2015.
- [19] A. Wehrfritz, V. Vuorinen, O. Kaario, and M. Larmi, "Large eddy simulation of high-velocity fuel sprays: studying mesh resolution and breakup model effects for spray A," *At. Sprays*, vol. 23, no. 5, 2013.
- [20] Q. Xue, S. Som, P. K. Senecal, and E. Pomraning, "Large eddy simulation of fuel-spray under non-reacting IC engine conditions," *At. Sprays*, vol. 23, no. 10, 2013.
- [21] J. Matheis and S. Hickel, "Multi-component vapor-liquid equilibrium model for LES of high-pressure fuel injection and application to ECN Spray A," *Int. J. Multiph. Flow*, vol. 99, pp. 294–311, Feb. 2018.
- [22] G. Lacaze, A. Misdariis, A. Ruiz, and J. C. Oefelein, "Analysis of high-pressure Diesel fuel injection processes using LES with real-fluid thermodynamics and transport," *Proc. Combust. Inst.*, vol. 35, no. 2, pp. 1603–1611, 2015.
- [23] L. Hakim, G. Lacaze, and J. Oefelein, "Large Eddy Simulation of Autoignition Transients in a Model Diesel Injector Configuration," *SAE Int. J. Fuels Lubr.*, vol. 9, no. 1, pp. 2016-01–0872, Apr. 2016.
- [24] R. N. Dahms and J. C. Oefelein, "Non-equilibrium gas–liquid interface dynamics in high-pressure liquid injection systems," *Proc. Combust. Inst.*, vol. 35, no. 2, pp. 1587–1594, 2015.
- [25] J. M. H. L. Sengers and E. Kiran, *Supercritical Fluids: Fundamentals for Application*. Kluwer Academic Publishers, 1994.
- [26] E. Knudsen, E. M. Doran, V. Mittal, J. Meng, and W. Spurlock, "Compressible Eulerian needle-to-target large eddy simulations of a diesel fuel injector," *Proc. Combust. Inst.*, vol. 36, no. 2, pp. 2459–2466, 2017.

- [27] J. Matheis and S. Hickel, "Multi-component vapor-liquid equilibrium model for LES and application to ECN Spray A," *arXiv Prepr. arXiv1609.08533*, 2016.
- [28] L. L. Tavlarides and G. Antiescu, "SUPERCRITICAL DIESEL FUEL COMPOSITION, COMBUSTION PROCESS AND FUEL SYSTEM," US 7,488,357 B2, 2009.
- [29] G. Anitescu, *Supercritical fluid technology applied to the production and combustion of diesel and biodiesel fuels*. Syracuse University, 2008.
- [30] R. Lin, *Issues on clean diesel combustion technology using supercritical fluids: thermophysical properties and thermal stability of diesel fuel*. Syracuse University, 2011.
- [31] D. T. Banuti, P. C. Ma, and M. Ihme, "Phase separation analysis in supercritical injection using large-eddy-simulation and vapor-liquid-equilibrium," in *53rd AIAA/SAE/ASEE Joint Propulsion Conference*, 2017, no. July.
- [32] C. Rodriguez, P. Koukouvinis, and M. Gavaises, "Simulation of supercritical diesel jets using the PC-SAFT EoS," *J. Supercrit. Fluids*, vol. 145, pp. 48–65, Mar. 2019.
- [33] P. C. Ma, Y. Lv, and M. Ihme, "An entropy-stable hybrid scheme for simulations of transcritical real-fluid flows," *J. Comput. Phys.*, vol. 340, no. March, pp. 330–357, Jul. 2017.
- [34] H. Terashima and M. Koshi, "Approach for simulating gas–liquid-like flows under supercritical pressures using a high-order central differencing scheme," *J. Comput. Phys.*, vol. 231, no. 20, pp. 6907–6923, Aug. 2012.
- [35] P. C. Ma, L. Bravo, and M. Ihme, "Supercritical and transcritical real-fluid mixing in diesel engine applications," 2015.
- [36] J. C. Oefelein and V. Yang, "Modeling High-Pressure Mixing and Combustion Processes in Liquid Rocket Engines," *J. Propuls. Power*, vol. 14, no. 5, pp. 843–857, Sep. 1998.
- [37] N. Zong, H. Meng, S.-Y. Hsieh, and V. Yang, "A numerical study of cryogenic fluid injection and mixing under supercritical conditions," *Phys. Fluids*, vol. 16, no. 12, pp. 4248–4261, Dec. 2004.
- [38] L. Selle and T. Schmitt, "Large-Eddy Simulation of Single-Species Flows Under Supercritical Thermodynamic Conditions," *Combust. Sci. Technol.*, vol. 182, no. 4–6, pp. 392–404, Jun. 2010.
- [39] J. P. Hickey and M. Ihme, "Supercritical mixing and combustion in rocket propulsion," *Annu. Res. Briefs, Cent. Turbul. Res. Stanford Univ. Stanford, CA*, 2013.
- [40] D.-Y. Peng and D. B. Robinson, "A New Two-Constant Equation of State," *Ind. Eng. Chem. Fundam.*, vol. 15, no. 1, pp. 59–64, Feb. 1976.
- [41] G. Soave, "Equilibrium constants from a modified Redlich-Kwong equation of state,"

- Chem. Eng. Sci.*, vol. 27, no. 6, pp. 1197–1203, Jun. 1972.
- [42] H. Terashima, S. Kawai, and N. Yamanishi, “High-Resolution Numerical Method for Supercritical Flows with Large Density Variations,” *AIAA J.*, vol. 49, no. 12, pp. 2658–2672, Dec. 2011.
- [43] H. Terashima and M. Koshi, “Characterization of cryogenic nitrogen jet mixings under supercritical pressures,” in *51st AIAA Aerospace Sciences Meeting including the New Horizons Forum and Aerospace Exposition*, 2013, no. January, pp. 2–11.
- [44] H. Terashima and M. Koshi, “Strategy for simulating supercritical cryogenic jets using high-order schemes,” *Comput. Fluids*, vol. 85, pp. 39–46, Oct. 2013.
- [45] J.-P. Hickey, P. C. Ma, M. Ihme, and S. S. Thakur, “Large Eddy Simulation of Shear Coaxial Rocket Injector: Real Fluid Effects,” *49th AIAA/ASME/SAE/ASEE Jt. Propuls. Conf.*, pp. 1–15, 2013.
- [46] C. Rodriguez, A. Vidal, P. Koukouvinis, M. Gavaises, and M. A. McHugh, “Simulation of transcritical fluid jets using the PC-SAFT EoS,” *J. Comput. Phys.*, vol. 374, pp. 444–468, Dec. 2018.
- [47] S.-K. Kim, H.-S. Choi, and Y. Kim, “Thermodynamic modeling based on a generalized cubic equation of state for kerosene/LOx rocket combustion,” *Combust. Flame*, vol. 159, no. 3, pp. 1351–1365, 2012.
- [48] C. Rodriguez, A. Vidal, P. Koukouvinis, and M. Gavaises, “Supercritical and transcritical real-fluid mixing using the PC-SAFT EOS,” in *Proceedings ILASS–Europe 2017. 28th Conference on Liquid Atomization and Spray Systems*, 2017.
- [49] T. García-Córdova, D. N. Justo-García, B. E. García-Flores, and F. García-Sánchez, “Vapor–Liquid Equilibrium Data for the Nitrogen + Dodecane System at Temperatures from (344 to 593) K and at Pressures up to 60 MPa,” *J. Chem. Eng. Data*, vol. 56, no. 4, pp. 1555–1564, Apr. 2011.
- [50] T. Schmitt, L. Selle, A. Ruiz, and B. Cuenot, “Large-Eddy Simulation of Supercritical-Pressure Round Jets,” *AIAA J.*, vol. 48, no. 9, pp. 2133–2144, Sep. 2010.
- [51] R. Abgrall and S. Karni, “Computations of Compressible Multifluids,” *J. Comput. Phys.*, vol. 169, no. 2, pp. 594–623, May 2001.
- [52] G. Billet and R. Abgrall, “An adaptive shock-capturing algorithm for solving unsteady reactive flows,” *Comput. Fluids*, vol. 32, no. 10, pp. 1473–1495, Dec. 2003.
- [53] P. C. Ma, Y. Lv, and M. Ihme, “Numerical methods to prevent pressure oscillations in transcritical flows,” no. 1999, pp. 1–12, Apr. 2017.
- [54] X. Lu and Y. Hu, *Molecular thermodynamics of complex systems*, vol. 131. Springer, 2008.

- [55] J. Gross and G. Sadowski, "Perturbed-Chain SAFT: An Equation of State Based on a Perturbation Theory for Chain Molecules," *Ind. Eng. Chem. Res.*, vol. 40, no. 4, pp. 1244–1260, Feb. 2001.
- [56] J. Gross and G. Sadowski, "Modeling Polymer Systems Using the Perturbed-Chain Statistical Associating Fluid Theory Equation of State," *Ind. Eng. Chem. Res.*, vol. 41, no. 5, pp. 1084–1093, Mar. 2002.
- [57] W. G. Chapman, G. Jackson, and K. E. Gubbins, "Phase equilibria of associating fluids," *Mol. Phys.*, vol. 65, no. 5, pp. 1057–1079, Dec. 1988.
- [58] M. S. Wertheim, "Fluids with highly directional attractive forces. I. Statistical thermodynamics," *J. Stat. Phys.*, vol. 35, no. 1–2, pp. 19–34, Apr. 1984.
- [59] M. S. Wertheim, "Fluids with highly directional attractive forces. II. Thermodynamic perturbation theory and integral equations," *J. Stat. Phys.*, vol. 35, no. 1–2, pp. 35–47, Apr. 1984.
- [60] M. S. Wertheim, "Fluids of dimerizing hard spheres, and fluid mixtures of hard spheres and dispheres," *J. Chem. Phys.*, vol. 85, no. 5, pp. 2929–2936, Sep. 1986.
- [61] J. A. Barker and D. Henderson, "Perturbation theory and equation of state for fluids: the square-well potential," *J. Chem. Phys.*, vol. 47, no. 8, pp. 2856–2861, 1967.
- [62] J. A. Barker and D. Henderson, "Perturbation theory and equation of state for fluids. II. A successful theory of liquids," *J. Chem. Phys.*, vol. 47, no. 11, pp. 4714–4721, 1967.
- [63] W. G. Chapman, K. E. Gubbins, G. Jackson, and M. Radosz, "SAFT: Equation-of-state solution model for associating fluids," *Fluid Phase Equilib.*, vol. 52, no. C, pp. 31–38, Dec. 1989.
- [64] N. P. Khare, "Predictive modeling of metal-catalyzed polyolefin processes," Virginia Tech, 2003.
- [65] S. Leekumjorn and K. Krejbjerg, "Phase behavior of reservoir fluids: Comparisons of PC-SAFT and cubic EOS simulations," *Fluid Phase Equilib.*, vol. 359, pp. 17–23, Dec. 2013.
- [66] A. J. de Villiers, C. E. Schwarz, A. J. Burger, and G. M. Kontogeorgis, "Evaluation of the PC-SAFT, SAFT and CPA equations of state in predicting derivative properties of selected non-polar and hydrogen-bonding compounds," *Fluid Phase Equilib.*, vol. 338, pp. 1–15, Jan. 2013.
- [67] M. Salimi and A. Bahramian, "The Prediction of the Speed of Sound in Hydrocarbon Liquids and Gases: The Peng-Robinson Equation of State Versus SAFT-BACK," *Pet. Sci. Technol.*, vol. 32, no. 4, pp. 409–417, Feb. 2014.
- [68] K. Schou Pedersen and C. Hasdbjerg, "PC-SAFT Equation of State Applied to Petroleum

- Reservoir Fluids,” in *SPE Annual Technical Conference and Exhibition*, 2007, vol. 1, no. 4, pp. 1–10.
- [69] S. Kawai, H. Terashima, and H. Negishi, “A robust and accurate numerical method for transcritical turbulent flows at supercritical pressure with an arbitrary equation of state,” *J. Comput. Phys.*, vol. 300, pp. 116–135, Nov. 2015.
- [70] C. J. Mueller *et al.*, “Diesel Surrogate Fuels for Engine Testing and Chemical-Kinetic Modeling: Compositions and Properties,” *Energy & Fuels*, vol. 30, no. 2, pp. 1445–1461, Feb. 2016.
- [71] A. Vidal, C. Rodriguez, P. Koukouvinis, M. Gavaises, and M. A. McHugh, “Modelling of Diesel fuel properties through its surrogates using Perturbed-Chain, Statistical Associating Fluid Theory,” *Int. J. Engine Res.*, p. 146808741880171, Sep. 2018.
- [72] H. B. Rokni, A. Gupta, J. D. Moore, M. A. McHugh, B. A. Bamgbade, and M. Gavaises, “Purely predictive method for density, compressibility, and expansivity for hydrocarbon mixtures and diesel and jet fuels up to high temperatures and pressures,” *Fuel*, vol. 236, no. August 2018, pp. 1377–1390, Jan. 2019.
- [73] R. W. Houim and K. K. Kuo, “A low-dissipation and time-accurate method for compressible multi-component flow with variable specific heat ratios,” *J. Comput. Phys.*, vol. 230, no. 23, pp. 8527–8553, Sep. 2011.
- [74] E. F. Toro, *Riemann solvers and numerical methods for fluid dynamics: a practical introduction*. Springer Science & Business Media, 2013.
- [75] G.-S. Jiang and C.-W. Shu, “Efficient Implementation of Weighted ENO Schemes,” *J. Comput. Phys.*, vol. 126, no. 1, pp. 202–228, Jun. 1996.
- [76] K. H. Kim and C. Kim, “Accurate, efficient and monotonic numerical methods for multi-dimensional compressible flows,” *J. Comput. Phys.*, vol. 208, no. 2, pp. 527–569, Sep. 2005.
- [77] R. J. Spiteri and S. J. Ruuth, “A New Class of Optimal High-Order Strong-Stability-Preserving Time Discretization Methods,” *SIAM J. Numer. Anal.*, vol. 40, no. 2, pp. 469–491, Jan. 2002.
- [78] T. H. Chung, M. Ajlan, L. L. Lee, and K. E. Starling, “Generalized multiparameter correlation for nonpolar and polar fluid transport properties,” *Ind. Eng. Chem. Res.*, vol. 27, no. 4, pp. 671–679, Apr. 1988.
- [79] M. R. Riazi and C. H. Whitson, “Estimating diffusion coefficients of dense fluids,” *Ind. Eng. Chem. Res.*, vol. 32, no. 12, pp. 3081–3088, Dec. 1993.
- [80] E. W. Lemmon, M. L. Huber, and M. O. McLinden, “NIST reference fluid thermodynamic

and transport properties–REFPROP.” version, 2002.

- [81] N. Kyriazis, P. Koukouvinis, and M. Gavaises, “Numerical investigation of bubble dynamics using tabulated data,” *Int. J. Multiph. Flow*, vol. 93, pp. 158–177, Jul. 2017.
- [82] S. Kawai and H. Terashima, “A high-resolution scheme for compressible multicomponent flows with shock waves,” *Int. J. Numer. Methods Fluids*, vol. 66, no. 10, pp. 1207–1225, Aug. 2011.
- [83] P. C. Ma, H. Wu, D. T. Banuti, and M. Ihme, “Numerical analysis on mixing processes for transcritical real-fluid simulations,” in *2018 AIAA Aerospace Sciences Meeting*, 2018, no. January.
- [84] M. L. Michelsen, “The isothermal flash problem. Part I. Stability,” *Fluid Phase Equilib.*, vol. 9, no. 1, pp. 1–19, Dec. 1982.
- [85] D. N. Justo-García, F. García-Sánchez, A. Romero-Martínez, E. Díaz-Herrera, and E. Juaristi, “Isothermal Multiphase Flash Calculations with the PC-SAFT Equation of State,” in *AIP Conference Proceedings*, 2008, vol. 979, pp. 195–214.
- [86] A. Tihic, G. M. Kontogeorgis, N. von Solms, M. L. Michelsen, and L. Constantinou, “A Predictive Group-Contribution Simplified PC-SAFT Equation of State: Application to Polymer Systems,” *Ind. Eng. Chem. Res.*, vol. 47, no. 15, pp. 5092–5101, Aug. 2008.
- [87] C. Rodriguez, H. B. Rokni, P. Koukouvinis, A. Gupta, and M. Gavaises, “Complex multicomponent real-fluid thermodynamic model for high-pressure Diesel fuel injection,” *Fuel*, p. Accepted Manuscript, 2019.
- [88] R. K. Sinnott, *Coulson & Richardson’s Chemical Engineering: Volume 6/Chemical Engineering Design*. Elsevier Butterworth Heinemann, 1999.
- [89] L. Lešnik, B. Kegl, G. Bombek, M. Hočevár, and I. Biluš, “The influence of in-nozzle cavitation on flow characteristics and spray break-up,” *Fuel*, vol. 222, pp. 550–560, Jun. 2018.
- [90] L. F. Cameretti, G. Sadowski, and J. M. Mollerup, “Modeling of Aqueous Electrolyte Solutions with Perturbed-Chain Statistical Associated Fluid Theory,” *Ind. Eng. Chem. Res.*, vol. 44, no. 9, pp. 3355–3362, Apr. 2005.
- [91] C. Held, L. F. Cameretti, and G. Sadowski, “Modeling aqueous electrolyte solutions,” *Fluid Phase Equilib.*, vol. 270, no. 1–2, pp. 87–96, Aug. 2008.
- [92] M. F. Gord, M. Roozbahani, H. R. Rahbari, and S. J. H. Hosseini, “Modeling thermodynamic properties of natural gas mixtures using perturbed-chain statistical associating fluid theory,” *Russ. J. Appl. Chem.*, vol. 86, no. 6, pp. 867–878, Jun. 2013.
- [93] N. Diamantonis and I. Economou, “Evaluation of SAFT and PC-SAFT EoS for the calculation

of thermodynamic derivative properties of fluids related to carbon capture and sequestration,” no. June 2011, pp. 1–32, 2011.

- [94] B. E. Poling, J. M. Prausnitz, and J. P. O’connell, *The properties of gases and liquids*. McGraw-hill New York, 2001.
- [95] R. Privat, R. Gani, and J.-N. Jaubert, “Are safe results obtained when the PC-SAFT equation of state is applied to ordinary pure chemicals?,” *Fluid Phase Equilib.*, vol. 295, no. 1, pp. 76–92, Aug. 2010.
- [96] H. Hoteit and A. Firoozabadi, “Simple phase stability-testing algorithm in the reduction method,” *AIChE J.*, vol. 52, no. 8, pp. 2909–2920, Aug. 2006.
- [97] E. Scientific, P. Company, and L. Michelsen, “The isothermal flash problem. part ii. phase-split calculation,” vol. 9, 1982.